ABSTRACT

ON OPTIMAL DESIGN AND APPLICATIONS OF LINEAR TRANSFORMS

by
Mehmet V. Tazebay

Linear transforms are encountered in many fields of applied science and engineering. In the past, conventional block transforms provided acceptable answers to different practical problems. But now, under increasing competitive pressures, with the growing reservoir of theory and a corresponding development of computing facilities, a real demand has been created for methods that systematically improve performance. As a result the past two decades have seen the explosive growth of a class of linear transform theory known as multiresolution signal decomposition. The goal of this work is to design and apply these advanced signal processing techniques to several different problems.

The optimal design of subband filter banks is considered first. Several design examples are presented for M-band filter banks. Conventional design approaches are found to present problems when the number of constraints increases. A novel optimization method is proposed using a step-by-step design of a hierarchical subband tree. This method is shown to possess performance improvements in applications such as subband image coding. The subband tree structuring is then discussed and generalized algorithms are presented. Next, the attention is focused on the interference excision problem in direct sequence spread spectrum (DSSS) communications. The analytical and experimental performance of the DSSS receiver employing excision are presented. Different excision techniques are evaluated and ranked along with the proposed adaptive subband transform-based exciser. The robustness of the considered methods is investigated for either time-localized or

frequency-localized interferers. A domain switchable excision algorithm is also presented. Finally, some of the ideas associated with the interference excision problem are utilized in the spectral shaping of a particular biological signal, namely heart rate variability. The improvements for the spectral shaping process are shown for time-frequency analysis. In general, this dissertation demonstrates the proliferation of new tools for digital signal processing.

ON OPTIMAL DESIGN AND APPLICATIONS OF LINEAR TRANSFORMS

by
Mehmet V. Tazebay

A Dissertation
Submitted to the Faculty of
New Jersey Institute of Technology
in Partial Fulfillment of the Requirements for the Degree of
Doctor of Philosophy

Department of Electrical and Computer Engineering

January 1996

APPROVAL PAGE

ON OPTIMAL DESIGN AND APPLICATIONS OF LINEAR TRANSFORMS

Mehmet V. Tazebay

Dr. Ali N. Akansu, Dissertation Advisor — Date
Associate Professor of Electrical and Computer Engineering, NJIT

Dr. Yeheskel Bar-Ness, Committee Member — Date
Distinguished Professor of Electrical and Computer Engineering, NJIT

Dr. Richard A. Haddad, Committee Member — Date
Professor of Electrical and Computer Engineering, NJIT

Dr. Dennis Karvelas, Committee Member — Date
Assistant Professor of Computer and Information Science, NJIT

Dr. Stanley Reisman, Committee Member — Date
Professor of Electrical and Computer Engineering, NJIT

Dr. Zoran Siveski, Committee Member — Date
Assistant Professor of Electrical and Computer Engineering, NJIT

BIOGRAPHICAL SKETCH

Author: Mehmet V. Tazebay

Degree: Doctor of Philosophy

Date: January 1996

Undergraduate and Graduate Education:

- Doctor of Philosophy,
  New Jersey Institute of Technology,
  Newark, NJ, 1996
- Master of Science in Biomedical Engineering,
  Boğaziçi University, Istanbul, Turkey, 1992.
- Bachelor of Science in Electronics and Communications Engineering,
  Istanbul Technical University, Istanbul, Turkey, 1989

Major: Electrical Engineering

Presentations and Publications:

[1] Mehmet V. Tazebay, and Ali N. Akansu, "Progressive Optimization in Subband Trees," in the Proceedings of SPIE's Visual Communications and Image Processing-94, Vol. 3, pp. 1100-1111, September 25-29, 1994, Chicago, IL.

[2] Mehmet V. Tazebay, and Ali N. Akansu, "Progressive Optimality in Hierarchical Filter Banks," in the Proceedings of IEEE International Conference on Image Processing, Vol. 1, pp. 825-829, November 13-16, 1994, Austin, TX.

[3] Mehmet V. Tazebay, Ali N. Akansu and Matthew Sherman, "A Novel Adaptive Time-Frequency Excision Technique for Direct Sequence Spread Spectrum Communications," in the Proceedings of IEEE International Symposium on Time-Frequency and Time-Scale Analysis, Vol. 1, pp. 492-495, October 25-28, 1994, Philadelphia, PA.

[4] Mehmet V. Tazebay, and Ali N. Akansu, "Progressive Optimization of Time-Frequency Localization in Subband Trees," in the Proceedings of IEEE International Symposium on Time-Frequency and Time-Scale Analysis, Vol. 1, pp. 128-131, October 25-28, 1994, Philadelphia, PA.

[5] Mehmet V. Tazebay, and Ali N. Akansu, "A Smart Time-Frequency Exciser for DSSS Communications," in the Proceedings of IEEE International Conference on Acoustics, Speech and Signal Processing, Vol. 2, pp. 1209-1212, May 8-12, 1995, Detroit, Michigan.

[6] Michael Meyer, Mehmet V. Tazebay, and Ali N. Akansu, "A Sliding and Variable Window-Based Multitone Excision for Digital Audio Broadcasting," in the Proceedings of IEEE International Symposium on Circuits and Systems, Vol 2, pp. 1464-1467, April 29 - May 3, 1995.

[7] Mehmet V. Tazebay, Rindala Saliba and Stanley Reisman, "Adaptive Time-Frequency Analysis of Autonomic Nervous System," in the Proceedings of IEEE International Conference in Engineering in Medicine and Biology Society , September 19-23, 1995, Montreal, Canada.

[8] Mehmet V. Tazebay, and Ali N. Akansu, "A Comparative Performance Study of Excisers in Spread Spectrum Communications," in the Proceedings of IEEE Global Telecommunications Conference, November 13-17, 1995, Singapore.

[9] Mehmet V. Tazebay and Ali N. Akansu, "*Adaptive subband transforms in time-frequency excisers for DSSS communications systems*," in IEEE Transactions on Signal Processing, Vol. 43, No. 11, pp. 2776-2782, November 1995.

[10] Ali N. Akansu and Mehmet V. Tazebay "Orthogonal Transmultiplexer: A Multiuser Communications Platform from FDMA to CDMA," an invited paper to be presented at the Europian Signal Processing Conference (EUSIPCO), Trieste, Italy, 1996.

This work is dedicated to
Tazebay family

ACKNOWLEDGMENT

First of all, I would like to express my sincere gratitude to my advisor, Professor Ali N. Akansu for his continuous support and enthusiasm. He patiently guided me through the problems we encountered, always insisting on the clear presentation of ideas. It is a privilege to work with him.

Many thanks are also due to Professor Stanley Reisman for his support during my Ph.D. program. Chapter 6 is a result of our continuing collaboration. I would like to thank to Professor Richard A. Haddad for participating in my committee despite his extremely busy schedule, accepting the invitation while still with Polytechnic University. (Recently, he joined the NJIT community). I would also like to thank to Professor Zoran Siveski for his fruitful conversations and readily available help. I wish to express my appreciation to Professor Yeheskel Bar-Ness and Professor Dennis Karvelas for serving on my committee.

I have cherished the company of Zeynep Toros, who has encouraged and supported me on many occasions. Thanks are due to Dr. Adil Benyassine who is still a very good friend although he graduated last year. I appreciate my warm friendship with Murat Berin. We had nice chats all along. It was a great pleasure to work with Michael Meyer during his stay in the USA. I would also like to acknowledge the members of the Center for Communications and Signal Processing Research: Luay Al-Nadi, Ambalavanar Arulambalam, Muzaffer Kanaan, Xueming Lin, Chris Peckham, Shahid Rana, Nadir Sezgin, Amit Shah, Zhiqiang Xu, Jin Zhou and many others. Thanks to all of you.

I am greatly indebted to Lisa Fitton, not only for reading the manuscript but also for being an understanding and caring friend. I would like to thank Brenda Walker from the ECE department and Brian White from Computing Services for their continuous help through bureaucratic and technical matters.

On the personal side, I would like to thank Guner and Sermet Tazebay, my mother and father, for making this all possible through their immeasurable love, encouragement and support for years. Finally, I am especially thankful to my wife, Aysu Selin, for her love and patience. Her support and encouragement have made many difficult things easier and joyful.

TABLE OF CONTENTS

TABLE OF CONTENTS
(continued)

TABLE OF CONTENTS
(continued)

Chapter **Page**

LIST OF TABLES

LIST OF FIGURES

LIST OF FIGURES
(continued)

LIST OF FIGURES
(continued)

LIST OF FIGURES
(continued)

LIST OF FIGURES
(continued)

LIST OF FIGURES
(continued)

Figure **Page**

LIST OF FIGURES
(continued)

Figure **Page**

CHAPTER 1

INTRODUCTION

The construction of bases for the linear expansion of signals has been extensively studied in the signal processing field. The linear expansion of signals aims to obtain better representations. Unitary transforms are often used for this purpose, as evidenced by the widespread applications of the discrete Fourier transform and the discrete cosine transform, among others. Unitary transforms have a number of desirable properties such as energy conservation, underlying orthogonality, stability and a well developed theory based on linear algebra. Computationally efficient implementations of these transforms have been reported in the literature. The evolution of multirate digital signal processing has the tools for a better understanding of discrete signals processed at different resolutions. The multirate filter banks still continue to evolve in its new extensions, design procedures, and applications. Multirate filter banks are the primary consideration of this study.

Multirate filter banks aim to decompose signals into their subband components. Here, linear, time-invariant, usually finite-impulse response filters are employed. The first perfect reconstruction filter banks were derived for two-band systems by Smith and Barnwell [43][44]. The M-band solutions immediately followed this initial design [53][52][57][56]. Daubechies established the link between discrete-time perfect reconstruction filter banks and wavelets [11]. She basically has shown that these two theories merge in the limit. The linkages and distinctions of discrete-time multirate filter banks and continuous-time wavelets are well understood in the engineering community [4][2].

The intent of this dissertation is to demonstrate the potential benefits of multirate filter banks. A new method is presented on optimal design of perfect reconstruction filter banks. Adaptive filter banks are investigated and applied to

the spread spectrum communication scenarios. The performance improvements and their theoretical justification are highlighted. The hierarchical subband decomposition of a predefined signal for its feature extraction is questioned. We also extend this philosophy to the problem of how to extract relevant features of a particular biological signal. The improvements can be drastic if the problem at hand can be simplified, unified, and better understood. In fact, understanding the multiresolution signal decomposition is the primary objective of this dissertation aiming to explore and apply the existing theories and develop new insights.

Outline and Contribution of Dissertation

Chapter 2 develops the background material required for the rest of the thesis. Discrete-time and multirate signal processing are briefly reviewed. We also cover the key structures for perfect reconstruction analysis/synthesis systems. Chapter 3 explores the optimal design of two-band and M-band filter banks. Several optimality criteria are presented along with design examples. The key results of M-band filter bank design theory are extended to a new design methodology. We present a new method for the optimal design of M-band hierarchical filters and show the resulting performance improvements in subband image coding. In chapter 4, we discuss the adaptive subband transforms. The idea of an optimal subband tree structuring concept is revisited and algorithms for this purpose are improved. In chapter 5 we look at the interference excision problem in direct sequence spread spectrum communication systems. In this chapter we propose the application of adaptive subband transforms to the interference rejection problem, along with other conventional techniques. The important features of jamming signals, such as time or frequency localization properties, are assessed by pre-processing of the received signal either in the time domain or in the frequency domain. The practical solutions to the transform domain interference excision are also discussed. We derive analytical

performance measures for an exciser-based DSSS receiver and compare the analytical performance results with the computer simulation results. The robustness of different competing excision techniques is also examined in this chapter. Chapter 6 moves to a totally different application area of time-frequency analysis. The major motivation here is to improve time-frequency representations of non-stationary biological signals by utilizing the decomposition tools developed earlier in the dissertation. It is shown that the fundamental concepts proposed are also still valid for this case. A signal-adaptive analysis method is presented. We show in this dissertation that it is possible to improve the performance of time-frequency representation techniques with the proper treatment of the signal at hand in most of the cases considered.

CHAPTER 2

MATHEMATICAL PRELIMINARIES

In order to establish a common ground, we shall review the basic material of multiresolution signal processing [4][55][17].

The mathematical notation and terminology for later chapters are also explained in this chapter. The details of fundamentals will not be repeated since they are extensively provided in the above references.

2.1 Review of Discrete-Time Signal Processing

A discrete-time signal is often described as $x(n)$ where $n \in Z$ (time index). The signal $x(n)$ is an ordered sequence of numbers that frequently results from sampling a continuous-time signal $x(t)$. We will particularly consider linear, causal and time-invariant systems throughout this work [37]. The output of such a system corresponding to an input $x(n)$ is defined by the convolution sum as

$$y(n) = \sum_k x(k)h(n-k) = x(n) * h(n), \tag{2.1}$$

where $h(n)$ is the impulse response of the discrete-time system. The two-sided Z-transform of $x(n)$ is defined by [37]

$$X(z) = \sum_{n=-\infty}^{\infty} x(n)z^{-n}. \tag{2.2}$$

The set of values for which the sum converges is known as the region of convergence. The one-sided Z-transform is of primary interest for the causal systems considered in this work. The discrete-time Fourier transform (DTFT) of $x(n)$ is defined as

$$X(e^{j\omega}) = \sum_{n=-\infty}^{\infty} x(n)e^{-j\omega n}, \tag{2.3}$$

and the inverse transform is given by

$$x(n) = \frac{1}{2\pi}\int_{-\pi}^{\pi} X(e^{j\omega})e^{j\omega n}. \tag{2.4}$$

The DTFT is invertible whenever it is convergent. The discrete Fourier transform is obtained from DTFT by sampling the latter at N equally spaced points on the unit circle of the Z-domain as:

$$X(k) = X(e^{j\omega})\mid_{\omega=\frac{2\pi k}{N}}. \tag{2.5}$$

For finite-length signals the DFT is defined as [37]

$$X(k) = \sum_{n=0}^{N-1} x(n)e^{-j\frac{2\pi kn}{N}}. \tag{2.6}$$

Based on these definitions, Eq.(2.1) can be rewritten in the Z-domain as

$$Y(z) = H(z)X(z), \tag{2.7}$$

and in the frequency domain as

$$Y(e^{j\omega}) = H(e^{j\omega})X(e^{j\omega}). \tag{2.8}$$

According to Parseval's theorem,

$$\sum_{n=-\infty}^{\infty} h(n)g^{*}(n) = \frac{1}{2\pi}\int_{0}^{2\pi} H(e^{j\omega})G^{*}(e^{j\omega})d\omega. \tag{2.9}$$

2.2 Linear Expansion of Discrete-time Signals

The linear expansion of discrete-time signals is the core of research problems dealt with in this dissertation. The choice of basis functions emphasized in this work are required to have two main properties, namely: (i) completeness and (ii) orthonormality. This section and the following sections will revisit different linear expansion techniques given in the literature.

In conventional block-transform processing, the signal is divided into independent

blocks of N-samples. In a vector-matrix representation, let any arbitrary N-length signal block be denoted as

$$\underline{x}^T = [x_0 \ , \ x_1 \ , \ldots \ , \ x_{N-1}], \tag{2.10}$$

and the corresponding spectral (transform) vector be

$$\underline{y}^T = [y_0 \ , \ y_1 \ , \ldots \ , \ y_{N-1}]. \tag{2.11}$$

The rows of a real unitary transform matrix $\mathbf{A}$ are called the basis functions and are denoted as $\underline{a}_m \quad (0 \leq m \leq N-1)$. The forward and inverse transforms are expressed as

$$\underline{y} = \mathbf{A}\underline{x} = \begin{bmatrix} a_{00} & a_{01} & \cdots & a_{0(N-1)} \\ a_{10} & a_{11} & \cdots & a_{1(N-1)} \\ \vdots & \vdots & \ddots & \vdots \\ a_{(N-1)0} & a_{(N-1)1} & \cdots & a_{(N-1)(N-1)} \end{bmatrix} \begin{bmatrix} x_0 \\ x_1 \\ \vdots \\ x_{N-1} \end{bmatrix} \tag{2.12}$$

and

$$\underline{x} = \mathbf{A}^{-1}\underline{y} = \mathbf{A}^T\underline{y} \ , \tag{2.13}$$

where $\mathbf{A}^{-1} = \mathbf{A}^T$. Any unitary NxN transform matrix will satisfy the above equations. This naturally highlights a considerable freedom in the choice of basis functions. It should be recognized that the applications might impose additional constraints on basis selection.

The conventional block transforms provide a fixed tiling of the time-frequency plane. Each basis function in the transform matrix is represented by a time-frequency tile. The size of the transform is the limiting factor on the resolution and number of discrete tiles. Hence, a discrete-time orthogonal transform projects a finite length signal onto its time-frequency tiles. The tile shapes and sizes may be uniform or arbitrary. If the tiling is done input dependant then the proper analysis tool is obtained over the fixed transforms. The construction of such schemes will be discussed in Chapter 4.

In signal compression application of transforms, the input signal is transformed into spectral coefficients which are then quantized, encoded and transmitted. The receiver performs the inverse operations for signal reconstruction. If the input signal is highly correlated, a valuable orthogonal transformation is expected to provide perfectly decorrelated or less correlated transform coefficients. Then, the quantization becomes quite efficient [26].

The discrete cosine transform (DCT) and DFT have been extensively studied and used in many 1-D and 2-D signal processing applications. Computationally, efficient implementations of these transforms exist. The Karhunen-Loéve transform (KLT) is an optimal method for perfectly decorrelating the coefficients of a stationary random process. Hence, it is a signal-dependent transform. The KLT is not used in practice, since the calculation of the transform matrix can be extremely complicated. The decorrelating properties of unitary block transforms have been utilized in speech, video compression, and many other signal processing and communications problems.

2.3 Multirate Filter Banks

The multirate filter bank is another popular method for projecting an input signal onto its basis functions. It decomposes the input signal into its individual subband spectra using a bank of analysis filters ($H_0(z)$, $H_1(z)$, ... , $H_{M-1}(z)$). Figure 2.1 displays a maximally decimated (critically sampled) M-band multirate filter bank. Each subband filter occupies π/M of full bandwidth. In other words, the full band signal is band-limited to a slower sampling rate. Naturally, this redundancy can be eliminated by down-sampling the sequence by the same rate (M) [4][55]. One in every M samples is retained by the downsampler of rate M. For the time-being we do not discuss subband coding but instead we will focus on the decimated outputs. These decimated outputs can be considered as the subband transform coefficients. Reconstruction of the signal is achieved by the up-sampling of the decimated subband

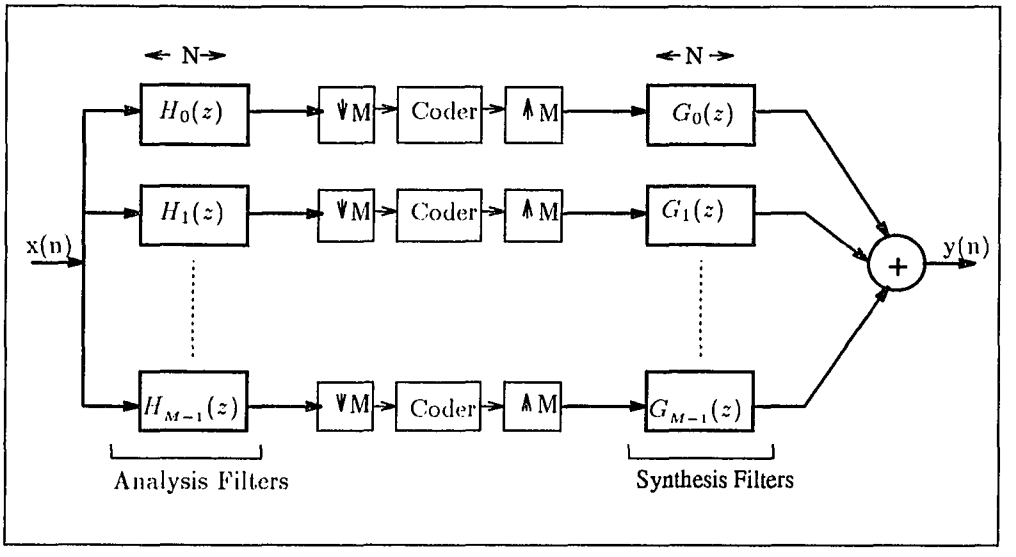

Figure 2.1 Uniform M-band analysis/synthesis filter bank.

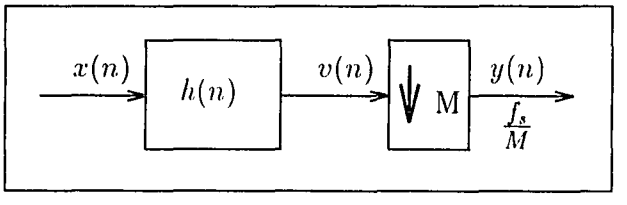

Figure 2.2 The decimation operation: an anti-aliasing filter and the down-sampler.

signals and filtering by the synthesis filters ($G_0(z)$, $G_1(z)$, ... , $G_{M-1}(z)$). Then, these interpolated outputs are summed together as the reconstructed signal.

2.3.1 Decimation Stage

A decimator generally consists of an anti-aliasing filter $\{h(n)\}$ followed by a down-sampler of rate M, as shown in Figure 2.2. Assuming the use of an FIR filter, the signal at the output of the filter is given by

$$v(n) = h(n) * x(n) = \sum_k h(k)x(n-k), \tag{2.14}$$

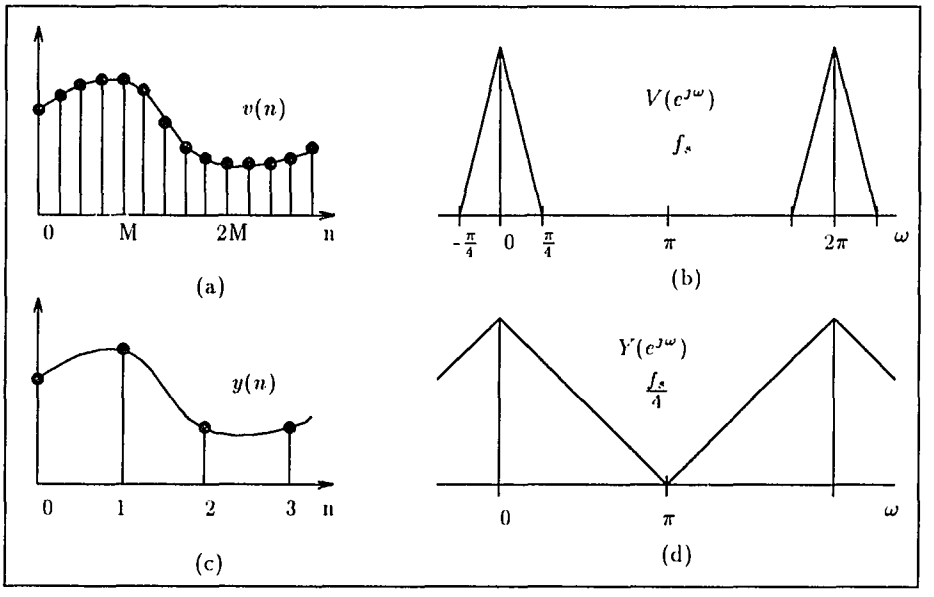

Figure 2.3 (a) Filtered signal at fast clock rate, (b) signal spectrum occupying $\frac{1}{4}$ of full band at fast clock rate, f_s, (c) down-sampled signal at slow clock rate, (d) spectrum of signal down-sampled by 4.

and the down-sampled signal is

$$y(n) = v(Mn). \tag{2.15}$$

Figures 2.3(a)-(d) illustrate the time and frequency domain effects of a down-sampling operation at the Nyquist rate. Decimation can thus be described as

$$y(n) = \sum_k h(k)x(nM - k). \tag{2.16}$$

It is also easily shown that [4][55]

$$Y(z) = \frac{1}{M}\sum_{k=0}^{M-1} V(z^{1/M}W^k), \quad W = e^{-j2\pi/M} \tag{2.17}$$

$$\text{or} \qquad Y(e^{j\omega}) = \frac{1}{M}\sum_{k=0}^{M-1} V(e^{j(\frac{\omega-2\pi k}{M})}). \tag{2.18}$$

2.3.2 Interpolation Stage

An interpolator consists of an up-sampler with the rate of M followed by a proper

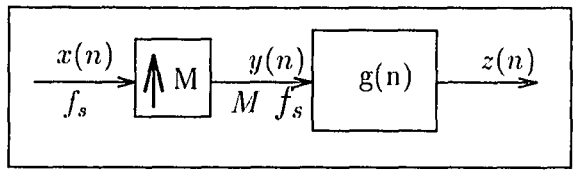

Figure 2.4 The interpolation operation: the up-sampler and anti-imaging filter.

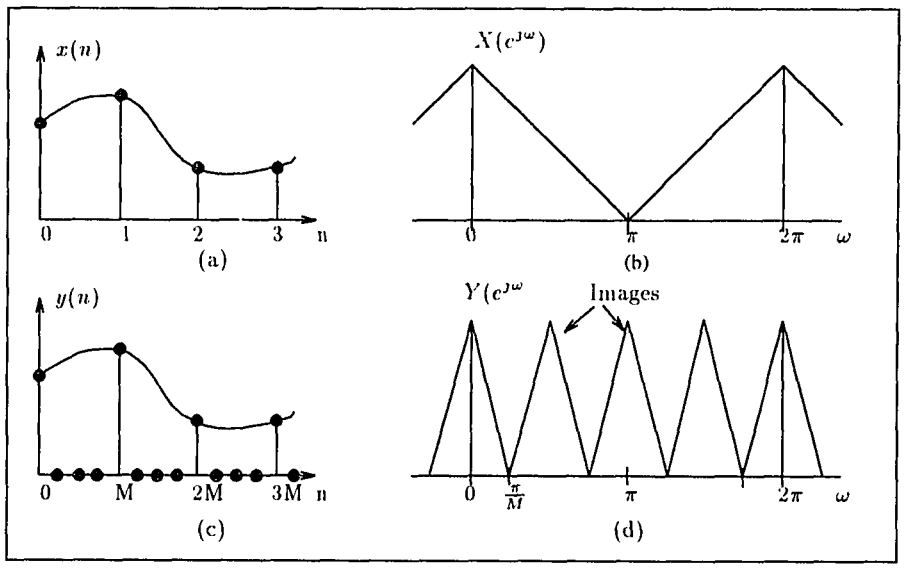

Figure 2.5 (a) Input $x(n)$ in the time domain, (b) input $X(e^{j\omega})$ in the frequency domain, (c) up-sampled signal $y(n)$ in the time domain for $M = 4$, (d) up-sampled signal $Y(e^{j\omega})$ in the frequency domain for $M = 4$.

anti-imaging filter $g(n)$, as shown in Figure 2.4. The up-sampler inserts $(M-1)$ zeros between the sample values and re-indexes the time scale. The operator is defined by

$$y(n) = \begin{cases} x(n/M), & n = 0, \pm M, \pm 2M, ... \\ 0, & \text{otherwise.} \end{cases} \tag{2.19}$$

The up-sampling operation stretches the signal in the time domain while compressing it in the frequency domain. Figures 2.5(a)-(d) illustrate the time and frequency domain effects of the up-sampling operation. Then, the output signal $z(n)$

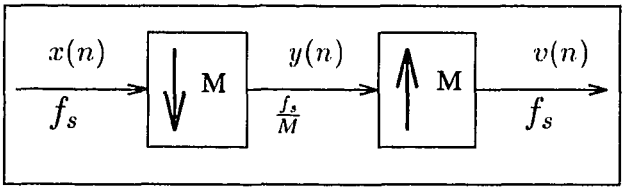

Figure 2.6 Down-sampler and up-sampler cascaded

is obtained by convolving $y(n)$ with the interpolation (anti-imaging) filter $g(n)$ as

$$z(n) = \sum_k g(k)y(n - Mk), \tag{2.20}$$

and essentially with

$$Y(z) = X(z^M) \quad , \quad Y(e^{j\omega}) = X(e^{j\omega M}). \tag{2.21}$$

2.3.3 Multirate Identities

(a) Down-sampler/Up-sampler Cascaded: If we position the down-sampler and the up-sampler back-to-back as shown in Figure 2.6, the following relationship is obtained as

$$v(n) = \begin{cases} x(n) & n = 0, \pm M, \pm 2M, ... \\ 0 & \text{otherwise.} \end{cases} \tag{2.22}$$

In this structure, down-sampling retains every M^{th} sample while up-sampling compresses $y(n)$ in frequency and inserts $(M-1)$ zeros between its sample values in the time domain. In the transform domain,

$$V(z) = \frac{1}{M} \sum_{k=0}^{M-1} X(zW^k) \tag{2.23}$$

or

$$V(e^{j\omega}) = \frac{1}{M} \sum_{k=0}^{M-1} X(e^{j(\omega - \frac{2\pi k}{M})}). \tag{2.24}$$

where $W = e^{-j\frac{2\pi}{M}}$. It is observed that $V(e^{j\omega})$ is simply the sum of M replicas of $X(e^{j\omega})$ spaced by $\frac{2\pi}{M}$ apart. Figure 2.7 displays the effects of a down-sampler/up-sampler cascade in the frequency domain. In particular, Figure 2.7(d) illustrates

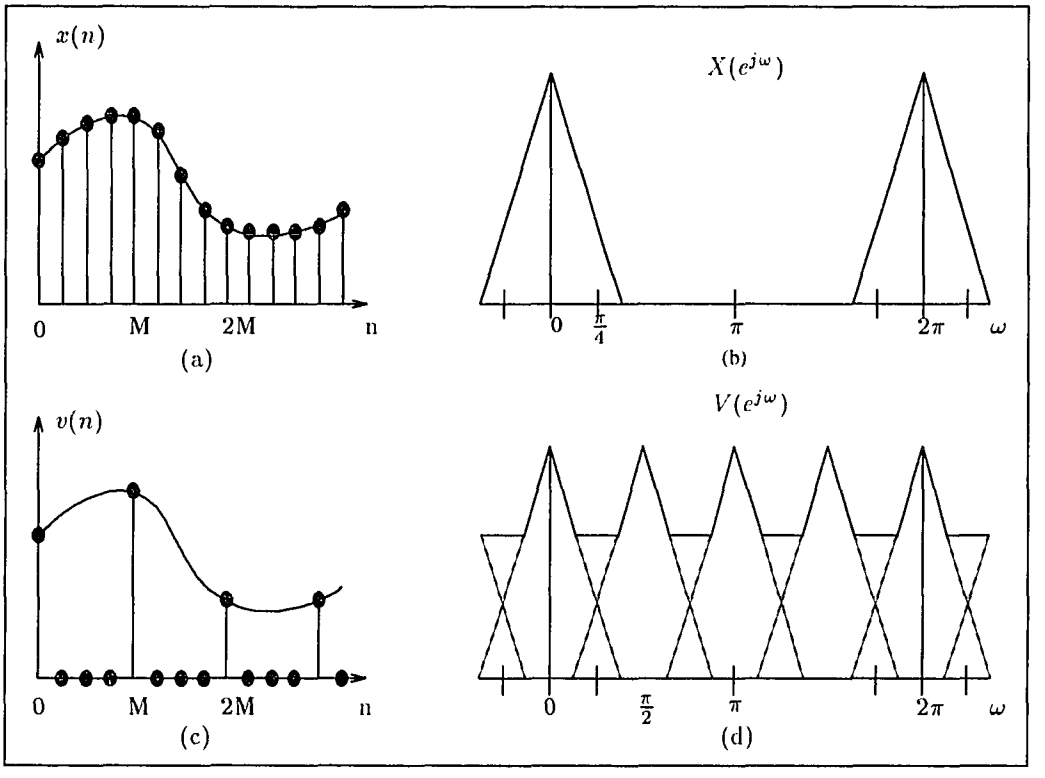

Figure 2.7 Down-sampler and up-sampler cascade operation: (a) input $x(n)$ in the time domain, (b) input $X(e^{j\omega})$ in the frequency domain, (c) output $v(n)$ in the time domain, (d) output $V(e^{j\omega})$ in the frequency domain.

both aliasing and imaging effects.

(b) Equivalent Structures: The equivalences of two multirate operator combinations given in Figure 2.8 are straightforward. Transfer functions can be moved across samplers and they become very useful for polyphase representation of multirate systems [4].

2.3.4 Perfect Reconstruction Systems and Paraunitary Filter Banks

In this section we will briefly discuss perfect reconstruction systems where the signal at the output of the system is a perfect replica of the input. Most of the material presented concerns the perfect reconstruction property. Its illustration is particularly simple for the case of a two-band filter bank (Figure 2.9). The input signal $x(n)$ is

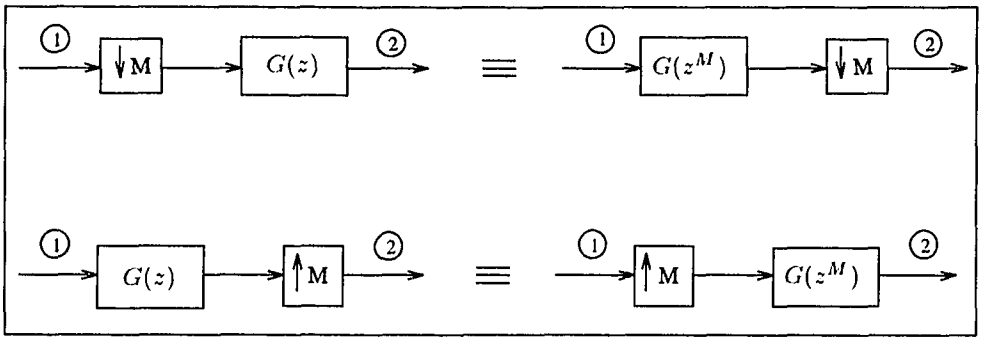

Figure 2.8 Equivalent structures.

first filtered by two filters $H_0(z)$ and $H_1(z)$, typically lowpass and high-pass filters, respectively. Each subband signal $[x_m(n)]$ is therefore limited to a bandwidth of approximately $\pi/2$. Therefore, they can be down-sampled by a factor of 2. At this point we exclude any processing after the analysis. The subband signals $y_0(n)$ and $y_1(n)$ are independently passed through a 2-fold up-sampler. The up-sampler output signals $v_0(n)$ and $v_1(n)$ are then passed through the synthesis filters $[G_0(z)$, $G_1(z)]$ and summed together to yield the output signal $\hat{x}(n)$. If the system is perfect reconstruction (PR), then it satisfies the property $\hat{x}(n) = cx(n - n_0)$, where c is a constant and n_0 is a proper integer delay. From Figure 2.9,

$$\begin{aligned} X_0(z) &= H_0(z)X(z) \\ X_1(z) &= H_1(z)X(z). \end{aligned} \tag{2.25}$$

The outputs of the down-samplers (from Eq.(2.17), M=2) are

$$\begin{aligned} Y_0(z) &= \frac{1}{2}[X_0(z^{1/2}) + X_0(-z^{1/2})] \\ Y_1(z) &= \frac{1}{2}[X_1(z^{1/2}) + X_1(-z^{1/2})]. \end{aligned} \tag{2.26}$$

Note that the second terms in Eq.(2.26) represent aliasing. These equations can be written in a matrix form as:

$$\begin{bmatrix} Y_0(z) \\ Y_1(z) \end{bmatrix} = \frac{1}{2} \begin{bmatrix} H_0(z^{1/2}) & H_0(-z^{1/2}) \\ H_1(z^{1/2}) & H_1(-z^{1/2}) \end{bmatrix} \begin{bmatrix} X(z^{1/2}) \\ X(-z^{1/2}) \end{bmatrix}. \tag{2.27}$$

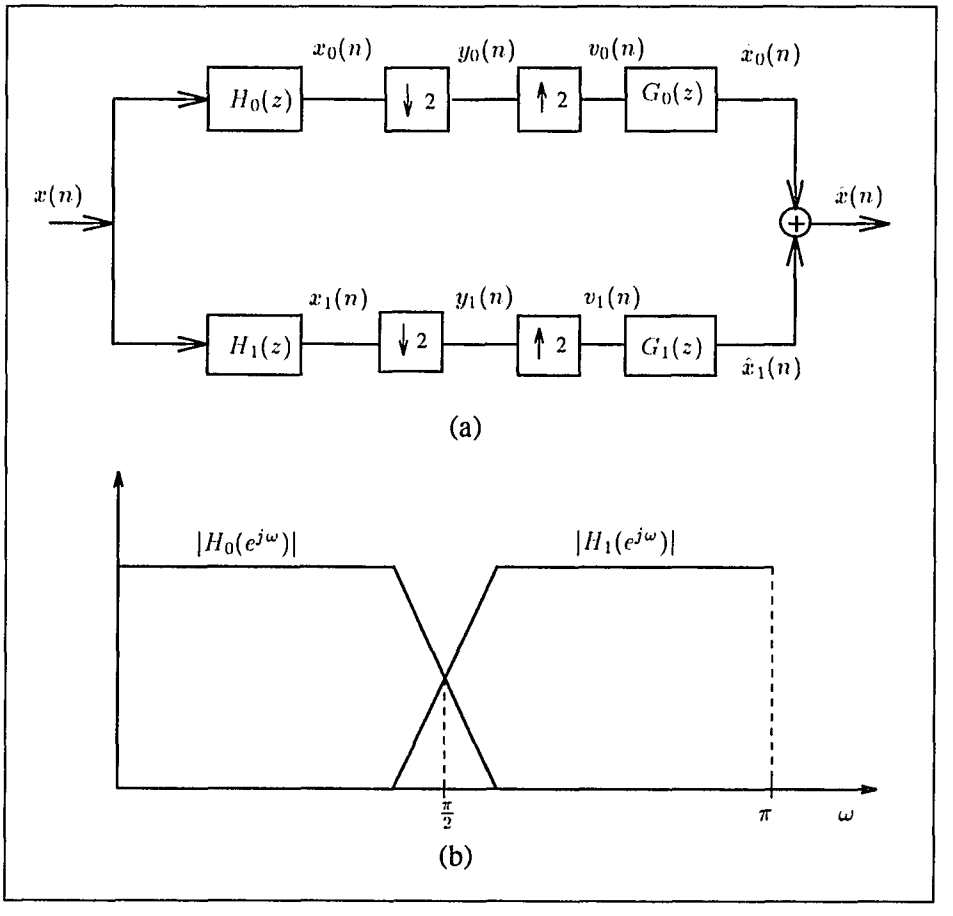

Figure 2.9 (a) 2-band filter bank (b) overlapping magnitude functions for analysis filters.

After the up-sampling the subband signals are expressed as

$$\begin{aligned} V_0(z) &= Y_0(z^2) = \frac{1}{2}[X_0(z) + X_0(-z)] \\ V_1(z) &= Y_1(z^2) = \frac{1}{2}[X_1(z) + X_1(-z)], \end{aligned} \tag{2.28}$$

and the reconstructed signal is obtained as

$$\hat{X}(z) = G_0(z)V_0(z) + G_1(z)V_1(z). \tag{2.29}$$

Rearranging Eq.(2.29), we have

$$\begin{aligned} \hat{X}(z) &= \frac{1}{2}[H_0(z)G_0(z) + H_1(z)G_1(z)]X(z) \\ &\quad + \frac{1}{2}[H_0(-z)G_0(z) + H_1(-z)G_1(z)]X(-z). \end{aligned} \tag{2.30}$$

This relationship can be rewritten in a matrix form as

$$\hat{X}(z) = \frac{1}{2}\begin{bmatrix} G_0(z) & G_1(z) \end{bmatrix} \underbrace{\begin{bmatrix} H_0(z) & H_0(-z) \\ H_1(z) & H_1(-z) \end{bmatrix}}_{\mathbf{H}_{AC}(z)} \begin{bmatrix} X(z) \\ X(-z) \end{bmatrix}, \tag{2.31}$$

where $\mathbf{H}_{AC}(z)$ is called the *alias component* (AC) matrix [4][55].

In many signal processing applications, FIR filters are desirable in the filter bank structure. In practice, the choice of FIR filters causes a degree of aliasing. Even though aliasing can be eliminated by the proper design (or choice) of $G_0(z)$ and $G_1(z)$ severe amplitude and phase distortion might still prevent perfect reconstruction [10]. It was first shown by Smith and Barnwell that all the three distortions, namely aliasing, amplitude and phase can be eliminated and a two-band perfect reconstruction (PR) quadrature mirror filter (QMF) can be obtained [43]. We can rewrite Eq.(2.30) as

$$\hat{X}(z) = T(z)X(z) + S(z)X(-z) \tag{2.32}$$

where $T(z)$ is the transfer or distortion function and $S(z)$ is the aliasing function. Therefore, in order to have a perfect reconstruction system we must (a) eliminate

aliasing, and (b) avoid magnitude and phase distortion. Next, we shall elaborate this statement further.

(a) Alias Cancellation

We can obtain an alias-free two-band filter bank if and only if

$$S(z) = H_0(-z)G_0(z) + H_1(-z)G_1(z) = 0. \tag{2.33}$$

The analysis and synthesis filters are chosen such that Eq.(2.33) is forced to zero. Given $H_0(z)$ and $H_1(z)$, we can choose

$$G_0(z) = H_1(-z), \qquad G_1(z) = -H_0(-z) \tag{2.34}$$

Even though the analysis filters create aliasing components, the synthesis filters are chosen in such a way that the alias components are cancelled. Obviously, this choice still does not guarantee a perfect reconstruction system.

(b) Magnitude and Phase Distortions

Being constrained by Eq.(2.33), the two-band filter bank is alias-free. Then, from Eq.(2.32),

$$\hat{X}(z) = T(z)X(z), \tag{2.35}$$

where $T(z)$ is called the transfer (or distortion) function. On the unit circle,

$$\hat{X}(e^{j\omega}) = T(e^{j\omega})X(e^{j\omega}), \tag{2.36}$$

and the system suffers from magnitude and a phase distortion if $T(z) \neq cz^{-n_0}$, (n_0 is an integer). In other words, if $T(z)$ is not all-pass, amplitude distortion occurs and similarly if $T(z)$ is not linear phase then phase distortion occurs.

A filter bank system satisfies perfect reconstruction if and only if all these distortions are cancelled, and then

$$\hat{X}(e^{j\omega}) = cz^{-n_0}X(z), \tag{2.37}$$

for all X(z). Therefore, from Eq.(2.31), we have the unique PR choice for synthesis filters as

$$\begin{bmatrix} G_0(z) \\ G_1(z) \end{bmatrix} = \frac{2z^{-n_0}}{det[\mathbf{H}_{AC}(z)]} \begin{bmatrix} H_1(-z) \\ -H_0(-z) \end{bmatrix}, \tag{2.38}$$

where $det[\mathbf{H}_{AC}(z)] = H_0(z)H_1(-z) - H_0(-z)H_1(z)$. For this case, the only possibility for PR is to find analysis filters which have

$$det[\mathbf{H}_{AC}(z)] = cz^{-n_0} \quad , \quad c \in R. \tag{2.39}$$

In special cases, PR filter banks possess lossless or a paraunitary condition. A causal transfer matrix with the property of

$$\tilde{\mathbf{H}}\mathbf{H} = M\mathbf{I} \qquad (M \in Z) \tag{2.40}$$

is called *paraunitary* if all of its entries are stable. The paraunitary property is a sufficient condition for an orthonormal (PR) filter bank but it is obviously not a necessary condition. Paraunitary filter banks have been extensively studied in [54]. This property is a natural extension of PR-QMF banks. This property is a natural extension of PR-QMF banks. A consequence of a paraunitary transfer matrix is that the system is power complementary, meaning that

$$\sum_{k=0}^{M-1} H_k(z)H_k(z^{-1}) = M, \tag{2.41}$$

or equivalently,

$$\sum_{k=0}^{M-1} |H_k(e^{j\omega})|^2 = M \quad , \quad \forall\omega. \tag{2.42}$$

CHAPTER 3

DESIGN OF FILTER BANKS AND PROGRESSIVE OPTIMALITY

In this chapter we address the optimal design of finite impulse response (FIR) filter banks. The optimal choice of filter coefficients in the filter bank design is the ultimate question with underlying applications. Our aim is to obtain the best filter coefficients so that a certain objective criterion is met. Next, we shall discuss the optimal filter bank design criteria. In the following sections, we will present two-band and M-band design concepts that have been well matured in the literature [4][55] and give our design example. Finally, we shall introduce the concept of *progressive optimization*, where M-band design becomes particularly less complicated than direct M-band design.

3.1 Optimal Filter Bank Design

Filter banks are widely used in image compression, high-fidelity audio compression, adaptive filtering, frequency-time multiplexing, and communications. The choice of filter coefficients is dictated by the objectives of the specific application. The desired objectives of a design are normally minimized or maximized as appropriate, while certain constraints have to be simultaneously satisfied. The nature of the optimization in this design problem is non-linear and, as we shall see, there are an infinite number of solutions in the solution space. In the optimization step the number of degrees of freedom (D) is the key factor and defined for an M-band PR-QMF filter bank as:

$$D = \sum_{k=1}^{M} N_k - C_{PR} - L, \tag{3.1}$$

where

N_k = number of parameters for k^{th} dimension,

M = dimensionality of the system (number of different filters),

C_{PR} = number of PR constraints,

L = number of degrees of freedom lost by additional specifications imposed on system system design.

In a general case, we can visualize each filter solution existing on one surface of an M-dimensional hyper-cube. Each filter is assumed to have N-tap FIR coefficients. The problem is to find an optimal set of filters such that an objective design criterion is met. Usually, there are certain symmetry and mirror image properties imposed on the filter bank structure. Therefore, the dimensionality of the system and N_k is structure-dependent and is reduced from maximum M-dimension and $\sum_k N_k$ parameters. We shall better clarify this statement during the design examples in the following sections. Underdetermined PR systems, with $D > 0$, are necessary for optimization; otherwise, a range of solutions do not exist. Most of the PR-QMF banks possess the property of being an underdetermined system. Figures 3.1,

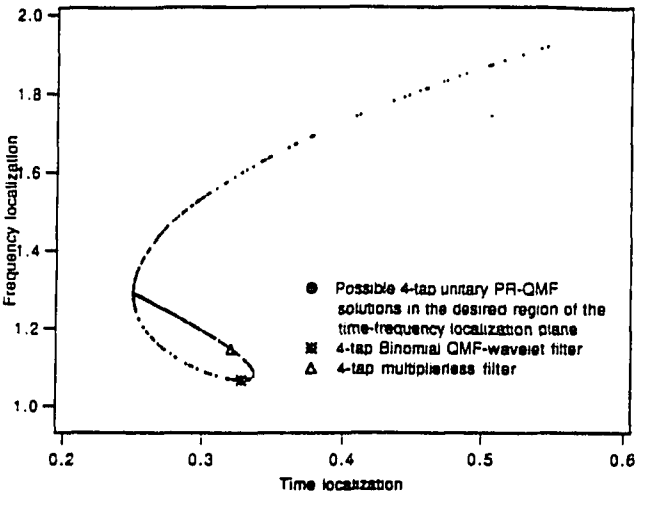

Figure 3.1 The time-frequency localizations of possible regular unitary two-band QMFs for the 4-tap case along with some of the PR-QMFs known in the literature.

3.2, and 3.3 display some of the possible 4-, 6- and 8-tap filter bank with desirable

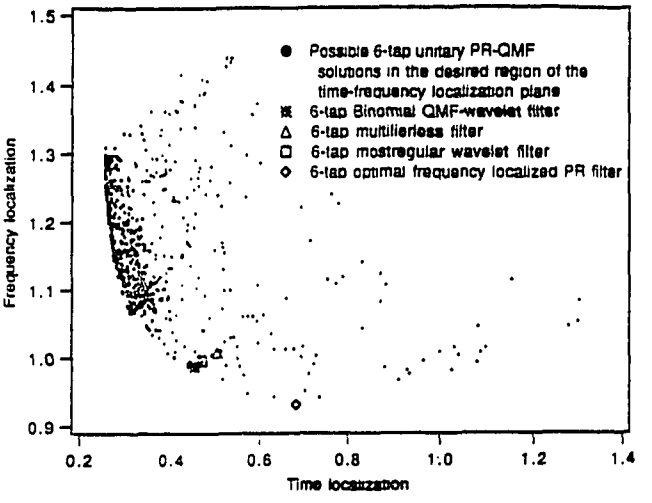

Figure 3.2 The time-frequency localizations of possible regular unitary two-band QMFs for the 6-tap case, along with some of the PR-QMFs known in the literature.

time-frequency properties for compression applications. Each point in these figures represents a PR-QMF solution and its associated time and frequency localizations.

This section emphasizes certain subsets of the solution space which meet the requirements of the selected design criteria. We will discuss a few measures of practical significance in the optimal design of PR-QMF banks. The optimality criterion might be based on a single design measure or a set of measures [8]. We will briefly review several known optimality measures in the next section [4][1]. A two-band PR-QMF will serve as the common ground for defining and emphasizing the significance of these design measures.

3.1.1 Measures of Optimality

Stopband Minimization (Passband Maximization)

PR-QMF banks are expected to have non-overlapping pass-bands. In practice, in

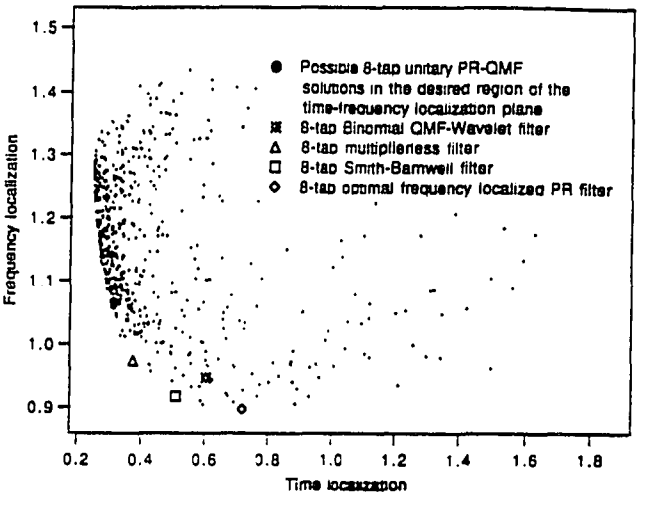

Figure 3.3 The time-frequency localizations of possible regular unitary two-band QMFs for the 8-tap case, along with some of the PR-QMFs known in the literature.

the pass-band region of analysis filter $H_l(z)$, all other analysis filters have their stop-bands leakages. An objective function for stopband minimization for a two-band PR-QMF bank is naturally defined as

$$\phi_s = \int_{\frac{\pi}{2}+\epsilon}^{\pi} |H_0(e^{j\omega})|^2 + \int_0^{\frac{\pi}{2}-\epsilon} |H_1(e^{j\omega})|^2, \tag{3.2}$$

where ϵ is some non-ideal transition bandwidth factor. Similarly, for the general case of an M-band PR-QMF bank,

$$\bar{\phi}_s = \sum_{l=0}^{M-1} \int_{l^{th}\ stop-band} |H_l(e^{j\omega})|^2. \tag{3.3}$$

An objective function for pass-band maximization for a two-band PR-QMF is similarly defined as

$$\phi_p = \int_0^{\frac{\pi}{2}+\epsilon} |H_0(e^{j\omega})|^2 + \int_{\frac{\pi}{2}-\epsilon}^{\pi} |H_1(e^{j\omega})|^2. \tag{3.4}$$

For the general case of an M-band PR-QMF bank,

$$\bar{\phi}_P = \sum_{l=0}^{M-1} \int_{l^{th}_{pass-band}} |H_l(e^{j\omega})|^2. \tag{3.5}$$

In PR-QMF bank structures, minimization of ϕ_s is thus a complementary condition to the maximization of ϕ_p. Since paraunitary systems require the analysis filters to be power complementary, sufficiently small stop-band responses force having pass-band responses $|H_l(e^{j\omega})|$ very close to unity. If one objective function is optimized then the goodness of the other is simultaneously assumed.

Energy Compaction

The energy compaction measure or gain of transform coding over PCM is a desired performance criterion for signal compression techniques. This measure is derived from the rate-distortion theory and its complete derivation can be found in Ref. [26]. Basically, it compares the mean square reconstruction error σ_c^2 for different signal coding schemes with that of pulse code modulation (PCM). It is assumed that each signal is used in conjunction with pdf-optimized quantizers, and optimal bit allocation is performed [26]. The energy compaction measure for an M-band unitary transform is written by

$$G_{TC} = \frac{\sigma_c^2(PCM)}{\sigma_c^2(TC)} = \frac{\frac{1}{N}\sum_{j=0}^{N-1} \sigma_j^2}{[\prod_{j=1}^{N-1} \sigma_j^2]^{1/N}}. \tag{3.6}$$

This is immediately recognized as the ratio of the arithmetic mean of the energies, $\{\sigma_j^2\}$, in each subband to their geometric mean. The output energy of a prototype low-pass filter $\underline{h}_L^T = [h_0\ ,\ h_1\ ,\ \ldots\ ,\ h_{N-1}]$ can be expressed in a matrix form as

$$\sigma_L^2 = \underline{h}_L^T \mathbf{R}_{xx} \underline{h}_L, \tag{3.7}$$

where R_{xx} is the covariance matrix of a zero-mean input. For the two-band case, let σ_L^2, σ_H^2 be the variances of low-pass and high-pass outputs, respectively. For a

paraunitary transformation, it is easily shown that

$$\sigma_x^2 = \frac{1}{2}(\sigma_L^2 + \sigma_H^2). \tag{3.8}$$

The energy compaction measure of a two-band PR-QMF bank is thus expressed as

$$G_{TC} = \frac{\frac{1}{2}(\sigma_L^2 + \sigma_H^2)}{[\sigma_L^2\sigma_H^2]^{1/2}} = \frac{\sigma_x^2}{[\sigma_L^2\sigma_H^2]^{1/2}}. \tag{3.9}$$

The energy compaction measure shapes the frequency responses of the filter responses for the given input spectrum. It is widely used in evaluating the performance of block and subband transforms [4].

Aliasing Energy

The paraunitary or lossless signal decomposition techniques completely cancel the aliasing from analysis through synthesis stages. In practice, however, the quantization or discarding of some of the subbands prevents perfect alias cancellation, and non-cancelled aliasing signal components might exist in the reconstructed signal. The impact of non-cancelled aliasing has been observed in some applications [50][31].

The aliasing energy components at the reconstructed low-pass filter output, in Figure 2.9, is expressed as [4][3]:

$$\sigma_{LA}^2 = \frac{1}{2}\int_{-\pi}^{\pi} |H_0(e^{-j\omega})|^2 S_{xx}(e^{j(\omega+\pi)})|H_0(e^{j(\omega+\pi)})|^2 d\omega, \tag{3.10}$$

where $S_{xx}(e^{j\omega})$ is the power spectral density (PSD) function of the input signal. The time domain version of Eq.(3.10) is given by [4]

$$\sigma_{LA}^2 = \sum_k [\rho(n) * (-1)^n \rho(n)] R_{xx}(k), \tag{3.11}$$

where R_{xx} is the auto-correlation sequence of the input and $\rho(n)$ is the autocorrelation sequence of the filter $h(n)$, defined as

$$\rho(n) = h(n) * h(-n). \tag{3.12}$$

The optimal solution based on this measure minimizes the aliasing energy component of the low-pass branch. This measure hence complements the energy compaction measure. In the latter approach, the filter spectrum has considerable flatness but the spill-over of the subband energies is not directly controlled. Therefore, the aliasing energy measure carefully monitors the aliasing component of the output energy. The non-aliasing energy ratio (NER) was also proposed in Ref. [3] as a result of this measure.

Zero-Mean Band-Pass and High-Pass Filters

Many signal sources have a significant spectral component at zero frequency. Therefore, an efficient transform technique must be able to represent the DC component within only one basis function. The zero-mean constraint for the band-pass and high-pass analysis filters $([\underline{h}_1\ ,\ \underline{h}_2\ ,\ \ldots\ ,\ \underline{h}_{M-1}])$ of an M-band PR-QMF bank is expressed as

$$\sum_n h_i(n) = 0 \quad , \quad i = 1, \ldots\ M-1, \tag{3.13}$$

Therefore, the high-pass filter of a two-band PR-QMF satisfy the requirement:

$$\sum_n h_1(n) = 0.$$

This requirement implies that there must be at least one zero of the low-pass prototype quadrature filter $H_0(e^{j\omega})$ at $\omega = \pi$.

Uncorrelated Subband Coefficients

The cross-correlation of subband signals is used as an optimization measure of filter prototypes. Optimal decorrelation is important if the subband signals are processed as independent signals. The Karhunen-Loéve transform is an optimal block transform with perfectly uncorrelated transform coefficients for the given input statistics. The KLT achieves a diagonal auto-correlation matrix (assuming a zero-mean). The cross-correlation of the two-subband signals $x_0(n)$, $x_1(n)$ in Figure

2.9 is defined as

$$E[x_0(n)x_1(n)] = R_{LH}(0) = \sum_n [\sum_l h(l)(-1)^l h(n-l)] R_{xx}(n), \qquad \forall n. \tag{3.14}$$

In Eq.(3.14), subband signals are considered at the same time index. In the general case, the cross-correlations $R_{LH}(k)$ of the subband signals in different time lags, $(k = 0, 1, \ldots, N)$, are constrained to be zero. Usually, there is more than one filter solution that satisfies the perfect decorrelation condition, $R_{LH}(0) = 0$ [8]. The one that optimizes the objective function under this constraint is the desired solution.

Time and Frequency Localizations

The time-frequency localization property of signal decomposition techniques is another important consideration. While bandwidth compression of the signals requires kernels with good localization in frequency, signal domain features demand a high degree of freedom in the time domain. The trade-off between time and frequency localization is bounded by the uncertainty principle [20]. Let $h(n) \leftrightarrow H(e^{j\omega})$ be a discrete-time Fourier transform pair:

$$H(e^{j\omega}) = \sum_{n=-\infty}^{\infty} h(n)e^{-jn\omega} \leftrightarrow f(n) = \frac{1}{2\pi}\int_{-\pi}^{\pi} H(e^{j\omega})e^{jn\omega}d\omega. \tag{3.15}$$

By Parseval's theorem, the energy is

$$E = \sum_{n=-\infty}^{\infty} |h(n)|^2 = \frac{1}{2\pi}\int_{-\pi}^{\pi} |H(e^{j\omega})|^2 d\omega.$$

The time and frequency centers (means) are defined as [20]

$$\bar{n} = \frac{1}{E}\sum_{-\infty}^{\infty} n|h(n)|^2, \tag{3.16}$$

$$\bar{\omega} = \frac{1}{2\pi E}\int_{-\pi}^{\pi} \omega|H(e^{j\omega})|^2 d\omega. \tag{3.17}$$

Then, the spreads of the function in time and frequency are written as [20]

$$\sigma_n^2 = \frac{1}{E}\sum_{-\infty}^{\infty}(n-\bar{n})^2|h(n)|^2, \tag{3.18}$$

$$\sigma_\omega^2 = \frac{1}{2\pi E}\int_{-\pi}^{\pi}(\omega-\bar{\omega})^2|H(e^{j\omega})|^2 d\omega, \tag{3.19}$$

For band-pass functions with frequency peaks centered at $\pm\hat{\omega}$, the frequency measure in Eq.(3.17) is not suitable. In this case, we are concerned about the spread around $\hat{\omega}$. Therefore, we define frequency spread on $[0,\pi]$ rather than $[-\pi,\pi]$. In this case, we take [20]

$$\hat{\omega} = \frac{\frac{1}{\pi}\int_0^\pi \omega|H(e^{j\omega})|^2 d\omega}{\frac{1}{\pi}\int_0^\pi |H(e^{j\omega})|^2 d\omega}, \tag{3.20}$$

$$\hat{\sigma}_\omega^2 = \frac{\frac{1}{\pi}\int_0^\pi (\omega-\hat{\omega})^2|H(e^{j\omega})|^2 d\omega}{\frac{1}{\pi}\int_0^\pi |H(e^{j\omega})|^2 d\omega}, \tag{3.21}$$

where $\bar{n}$ and σ_n^2 remain unchanged. The time and frequency centers and spreads defined above can be used as the design criteria. The joint time-frequency localization of a discrete-time function is expressed as

$$J_L = \sigma_\omega^2\sigma_n^2, \tag{3.22}$$

and it is usually minimized in most of the applications [46].

3.2 Optimal Design of Two-band Filter Bank

We have laid out the foundations of optimal PR filter bank design. We will proceed with a detailed treatment of a generic two-band PR-QMF filter bank, which was briefly discussed in section 2.3.5. The output of the two-band filter bank in Figure 2.9 was obtained as

$$\hat{X}(z) = T(z)X(z) + S(z)X(-z),$$

where $T(z)$ and $S(z)$ are transfer (distortion) and aliasing functions, respectively. We recall from Eq.(2.31),

$$\begin{aligned} S(z) &= H_0(-z)G_0(z) + H_1(-z)G_1(z), \\ T(z) &= H_0(z)G_0(z) + H_1(z)G_1(z). \end{aligned}$$

Again, note that in order to achieve perfect reconstruction, the following conditions are required to be satisfied as

$$S(z) = 0\ ,\ \forall z \tag{3.23}$$

$$T(z) = cz^{-n_0}\ ,\ \forall z\ , \tag{3.24}$$

where c ($c \in R$) and n_0 ($n_0 \in Z$) are constants. Eq.(3.24) eliminates the aliasing and Eq.(3.24) guarantees a distortionless transfer function. We choose

$$G_0(z) = H_1(-z), \quad G_1(z) = -H_0(-z), \tag{3.25}$$

which will perfectly cancel aliasing. Additionally, if we let analysis filters be related as [43][4]

$$H_1(z) = z^{-(N-1)}H_0(-z^{-1}), \tag{3.26}$$

where N is the length of the FIR filter. Then, $T(z)$ becomes

$$T(z) = \frac{1}{2}z^{-(N-1)}[H_0(z)H_0(z^{-1}) + H_0(-z)H_0(-z^{-1})]. \tag{3.27}$$

For this arrangement of the filters, we get perfect reconstruction if and only if

$$Q_i(z) = H_i(z)H_i(z^{-1}) + H_i(-z)H_i(-z^{-1}) = \text{constant}\ ,\quad (i = 0, 1) \tag{3.28}$$

$$= \quad R_i(z) + R_i(-z) \;=\; \text{constant} \tag{3.29}$$

where $R_i(z)$ is the spectral density function of analysis filter $H_i(z)$, $(i = 0, 1)$ and can be written as

$$\begin{aligned} R_i(z) + R_i(-z) &= \sum_{n=-(N-1)}^{(N-1)} [\rho_i(n) z^{-n} + \rho_i(n)(-z)^{-n}] \\ &= \sum_{n=-(N-1)}^{(N-1)} \rho_i(n)[1 + (-1)^n] z^{-n} \\ &= 2 \sum_{n=-(N-1)}^{(N-1)} \rho_i(2n) z^{-(2n+1)} , \end{aligned} \tag{3.30}$$

where

$$\rho_i(2n) = \sum_k h_i(k) h_i(k + 2n) \quad , \quad (i = 0, 1). \tag{3.31}$$

Eq.(3.31) implies that autocorrelation of $h_i(n)$ has all but one of its even-indexed terms equal to zero. Hence, these are the *PR constraints* as

$$\sum_k h_i(k) h_i(k + 2n) = \delta(n) , \tag{3.32}$$

with the normalization

$$\sum_{k=0}^{(N-1)} |h_i(k)|^2 \;=\; 1. \tag{3.33}$$

Essentially, N has to be a multiple of 2 for PR. The cross-correlation of $h_0(n)$ and $h_1(n)$ has all even-indexed terms equal to zero:

$$\sum_k h_0(k) h_1(k + 2n) = 0. \tag{3.34}$$

It is also possible to write Eq.(3.32) and (3.34) in the matrix form. First, we define the low-pass filter vector as

$$\underline{h}_0^T = [\, h_0(0) \quad h_0(1) \quad \ldots \quad \ldots \quad h_0(N-1) \quad \ldots \quad].$$

The vector $\underline{h}_0$ and its translations by multiples of two form the following analysis transformation matrix:

$$\mathbf{H}_0 = \begin{bmatrix} h_0(0) & h_0(1) & h_0(2) & \ldots & h_0(N-1) & 0 & 0 & 0 & \ldots \\ 0 & 0 & h_0(0) & \ldots & h_0(N-3) & h_0(N-2) & h_0(N-1) & 0 & \ldots \\ \vdots & \vdots & \ddots & & \vdots & \vdots & \vdots & \vdots & \vdots \end{bmatrix}. \tag{3.35}$$

For a paraunitary two-band PR-QMF filter bank we note the following:

$$\mathbf{H}_0\mathbf{H}_0^T = \frac{1}{2}\mathbf{I} \qquad \text{and} \qquad \mathbf{H}\underline{h}_0 = \begin{bmatrix} 1 \\ 0 \\ \vdots \\ 0 \end{bmatrix}. \tag{3.36}$$

where $\mathbf{I}$ is the identity matrix. Similarly, we can write $\mathbf{H_1}$ as the matrix with impulse responses $h_1(n+2k)$. Next, observe that

$$\mathbf{H}_0\mathbf{H}_1^T = \mathbf{0} \tag{3.37}$$

$$\mathbf{H}_0\mathbf{H}_0^T + \mathbf{H}_1\mathbf{H}_1^T = \mathbf{I}. \tag{3.38}$$

The following is a summary of the above vector-matrix equations:

(i) The projection of h_0 onto $\mathbf{H}_0$ has a single non-zero element as a requirement of shift orthogonality.

(ii) Eq.(3.38) points out the projection of cross terms between h_0 and h_1, which necessarily are zero.

(iii) Eq.(3.38) implies that with choices of Eq.(3.25) and (3.26), we obtain not only perfect reconstruction but also a paraunitary system.

Such solutions were first shown by Smith and Barnwell [43]. A prototype $H_0(z)$

that satisfies Eq.(3.32) with above properties results in a two-band PR-QMF bank structure with the corresponding four impulse responses:

$$\begin{aligned} h_0(n) &\longleftrightarrow H_0(z) \\ h_1(n) = (-1)^{(N-1-n)} h_0(N-1-n) &\longleftrightarrow H_1(z) = z^{-(N-1)} H_0(-z^{-1}) \\ g_0(n) = h_0(N-1-n) &\longleftrightarrow G_0(z) = H_1(-z) \\ g_1(n) = (-1)^n h_0(n) &\longleftrightarrow G_1(z) = H_0(-z). \end{aligned} \tag{3.39}$$

Design Examples

The design of a two-band, N-tap PR-QMF bank is a relatively easy problem compared to an M-band ($M > 2$) PR-QMF bank design. Now, as a generic structure, we will consider the following impulse responses for N-tap analysis filters of a two-band PR-QMF bank:

$$\begin{bmatrix} H_0 \\ H_1 \end{bmatrix} : \begin{bmatrix} h(0) & h(1) & h(2) & \dots & h(N-1) \\ -h(N-1) & h(N-2) & -h(N-3) & \dots & h(0) \end{bmatrix}, \tag{3.40}$$

where N is a multiple of 2. The dimensionality of a two-band PR-QMF bank is one in this case since H_1, G_0, G_1 can all be generated from the low-pass prototype H_0, as pointed out in Eq.(3.39). Therefore, the number of PR constraints (without the unitary condition) for this structure with $N = 2K$ is given by

$$C_{PR} = \frac{N}{2} - 1 = K - 1, \quad (K \in Z), \tag{3.41}$$

and the zero-mean condition for the high-pass filter ($\sum_k (-1)^{k+1} h_0(k) = 0$) implies another constraint as $L = C_{ZM} = 1$. The unitary condition can always be skipped since the filters can always be normalized after the optimization without loosing generality. Hence, we have

$$\left\{ \begin{array}{lcl} N_1 & = & N = 2 * K \\ C_{PR} & = & \frac{N}{2} - 1 = K - 1 \\ L & = & 1 \end{array} \right\}.$$

Table 3.1 Number of degrees of freedom for the given structure along with PR-constraints and number of parameters

Filter Length (N)	N_1	C_{PR}	D
2	2	0	1
4	4	1	2
6	6	2	3
10	10	4	5
100	100	49	50
1000	1000	499	500

We can explicitly define the number of degrees of freedom for this structure as

$$D = N_1 - C_{PR} - L = K. \tag{3.42}$$

Table 3.1 displays the number of degrees of freedom for different length two-band PR-QMFs. Clearly, D is a linear function of filter length. Usually, moderate values of D are desired. If D is a small value, then a good solution may not be feasible for the given objective criterion. On the other hand, if D is very large, then within practical optimization techniques, the local optimum solutions are more likely to be reached instead of a global optimum. Also, note that for $N = 2$ we obtain the trivial solution for a two-band filter bank (e.g. $H_0 = \frac{1+z^{-1}}{\sqrt{2}}$ and $H_1 = \frac{1-z^{-1}}{\sqrt{2}}$). Figures 3.4(a)-(b) display the time and frequency (magnitude response) functions of 8-tap PR-QMF solutions for the optimal energy compaction measure. Similarly, another 8-tap solution is given in Figure 3.5 for a stop-band minimized two-band PR-QMF. In Figure 3.6, the aliasing energy minimization is considered. Figures 3.7 and 3.8 display time- and frequency-localized 8-tap solutions, respectively. Finally, we give the joint time-frequency localized 8-tap solution in Figure 3.9.

3.3 M-Band Filter Bank Design

The M-band filter bank with M equal bandwidth parallel filters tries to achieve

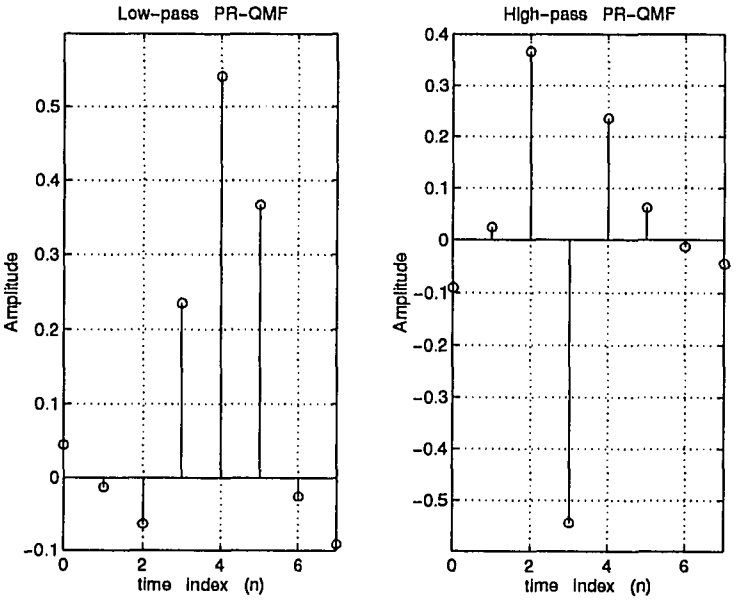

(a)

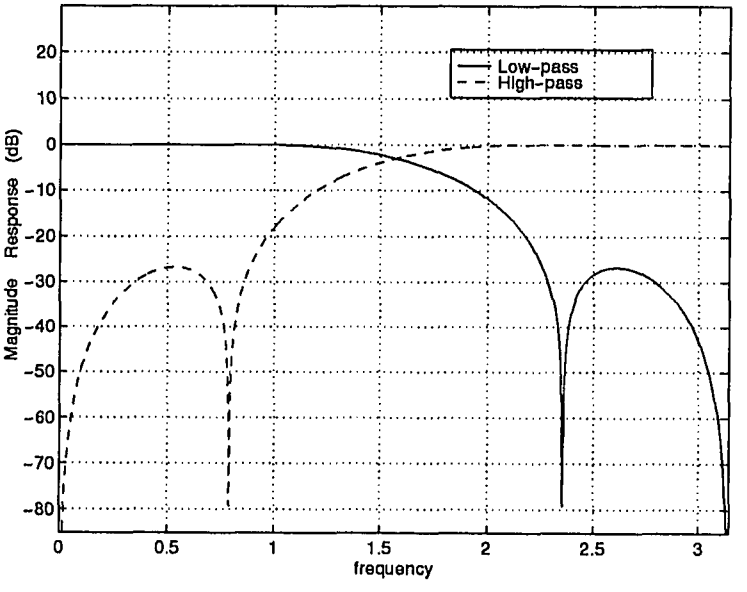

(b)

Figure 3.4 Two-band, 8-tap optimal PR-QMF solutions for the maximum energy compaction criterion: (a) time functions, (b) magnitude responses.

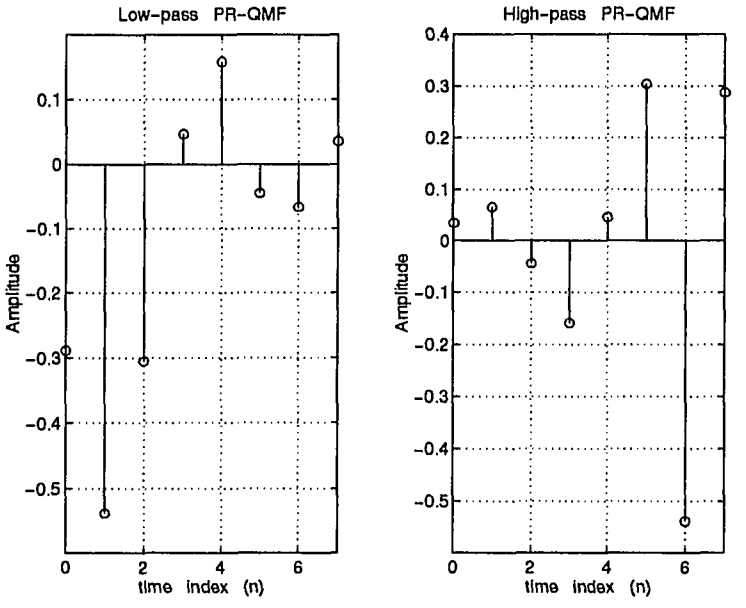

(a)

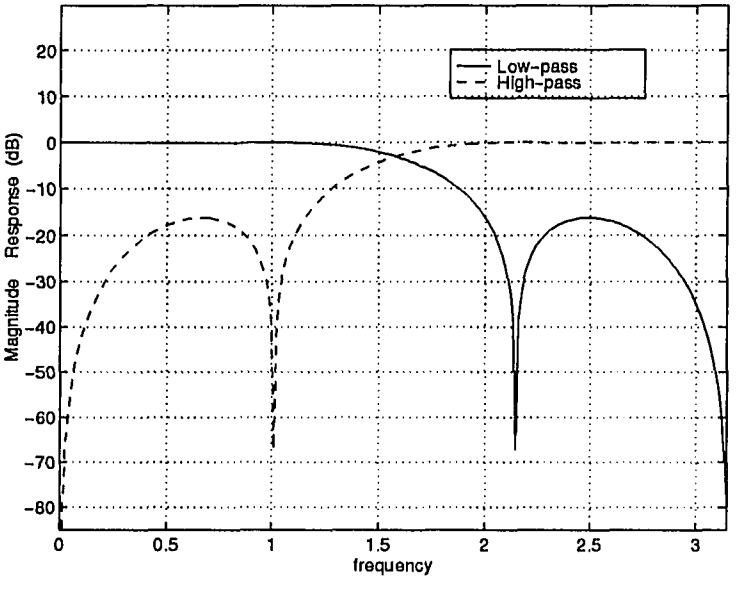

(b)

Figure 3.5 Two-band, 8-tap optimal PR-QMF solutions for the minimum stop-band energy criterion: (a) time functions, (b) magnitude responses.

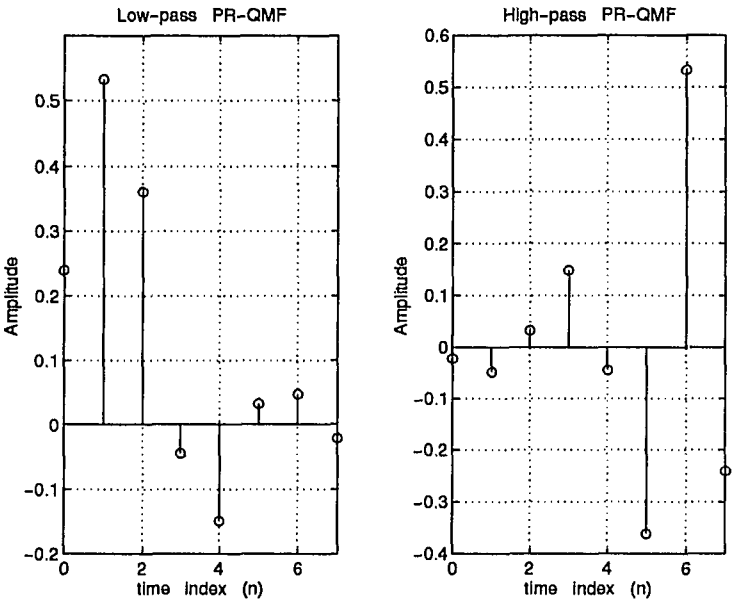

(a)

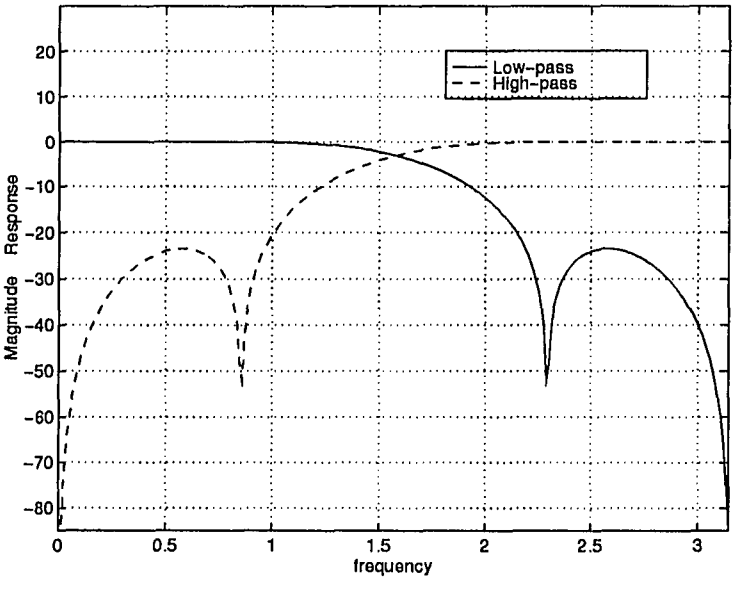

(b)

Figure 3.6 Two-band, 8-tap optimal PR-QMF solutions for the minimum stop-band energy criterion: (a) time functions, (b) magnitude responses.

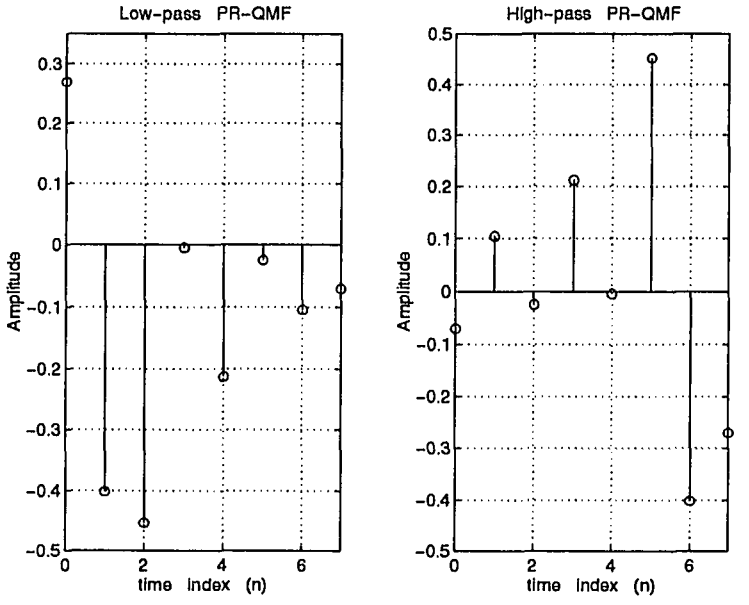

(a)

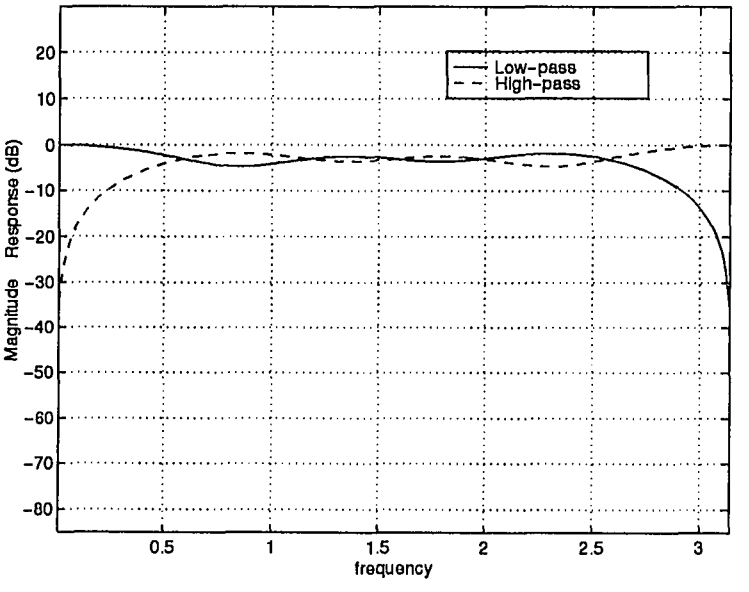

(b)

Figure 3.7 Two-band, 8-tap optimal PR-QMF solutions for the minimum time localization criterion: (a) time functions, (b) magnitude responses.

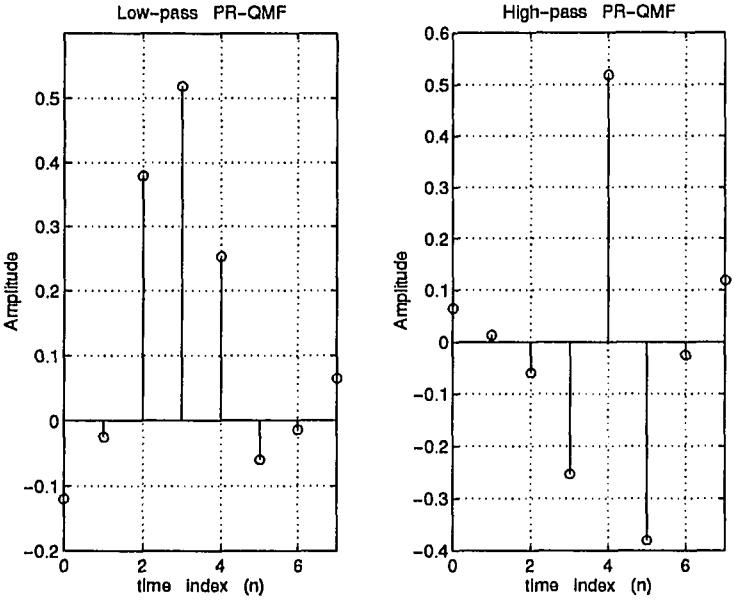

(a)

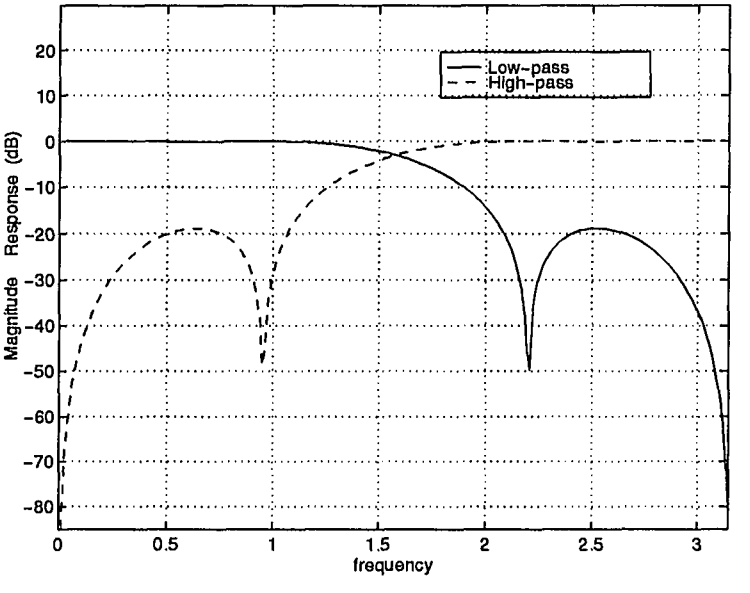

(b)

Figure 3.8 Two-band, 8-tap optimal PR-QMF solutions for the minimum frequency localization criterion: (a) time functions, (b) magnitude responses.

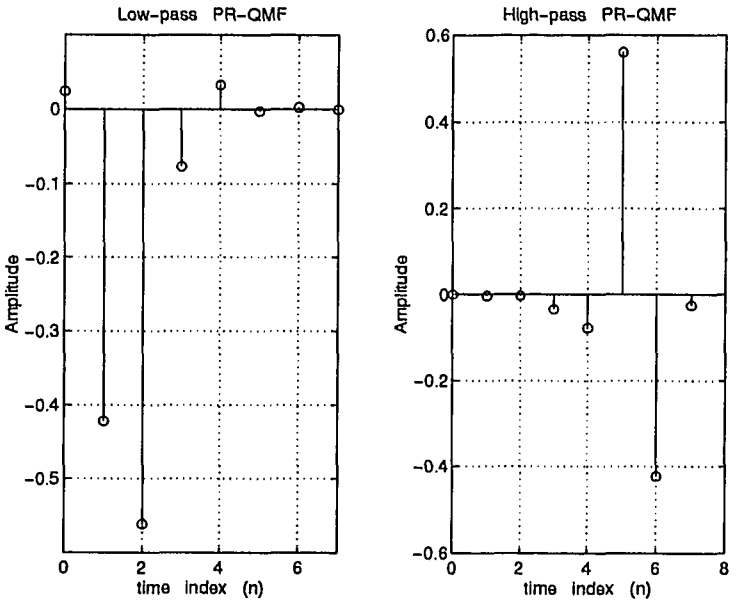

(a)

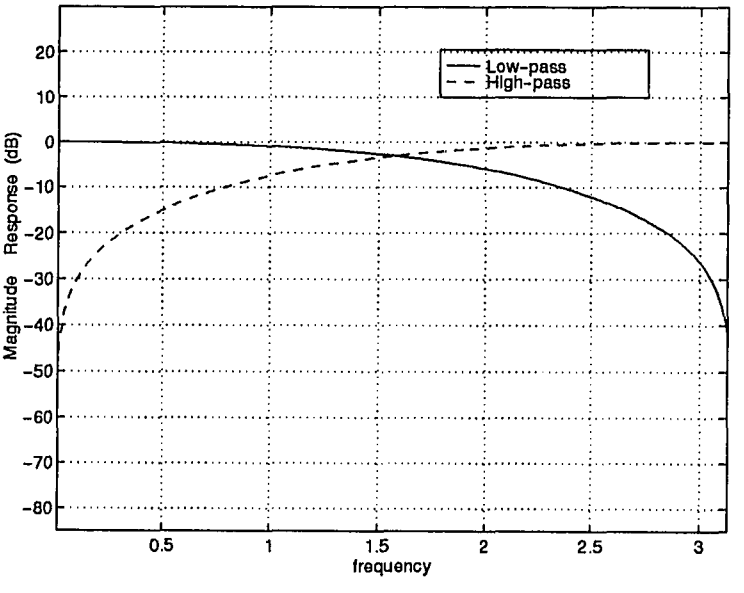

(b)

Figure 3.9 Two-band, 8-tap optimal PR-QMF solutions for the minimum joint time-frequency localization criterion: (a) time functions, (b) magnitude responses.

uniform spectral decomposition. Figure 3.10 shows a maximally decimated M-band filter bank and the generic magnitude responses. The system is a cascade of M-band analysis and synthesis stages. Each of the filters is equally spaced in frequency and has a π/M bandwidth. The two-band PR-QMF bank ($M = 2$) is a special case of the M-band filter bank. The generalization of alias cancellation and perfect reconstruction conditions is an extension of two-band filter bank analysis and hence we shall proceed with the same methodology.

In Figure 3.10(a), the input signal is decomposed into M subband signals ($x_k(n)$, $k = 0, 1, \ldots, M-1$) by the analysis filters. Since the filtered signals have an approximately π/M bandwidth, they are down-sampled by M to obtain $y_k(n)$. After analysis filters, each subband signal is given by

$$X_l(z) = H_l(z)X(z), \tag{3.43}$$

and the decimated signals after down-sampling are

$$V_l(z) = \frac{1}{M}\sum_{k=0}^{M-1} H_l(z^{1/M}W^k)X(z^{1/M}W^k), \tag{3.44}$$

where $l = 0, 1, \ldots, M-1$ and $W = e^{-j\omega/M}$. The decimated signals can be written as

$$\underline{V}^T(z) = [\,V_0(z) \quad V_1(z) \quad \ldots \quad V_{M-1}(z)\,], \tag{3.45}$$

and the aliasing component matrix for the M-band case is

$$\mathbf{H}_{AC}(z) = \begin{bmatrix} H_0(z) & H_1(z) & \ldots & H_{M-1}(z) \\ H_0(zW^1) & H_1(zW^1) & \ldots & H_{M-1}(zW^1) \\ \vdots & \vdots & \ddots & \\ H_0(zW^{M-1}) & H_1(zW^{M-1}) & \ldots & H_{M-1}(zW^{M-1}) \end{bmatrix}. \tag{3.46}$$

The aliasing component vector for the input signal is given by

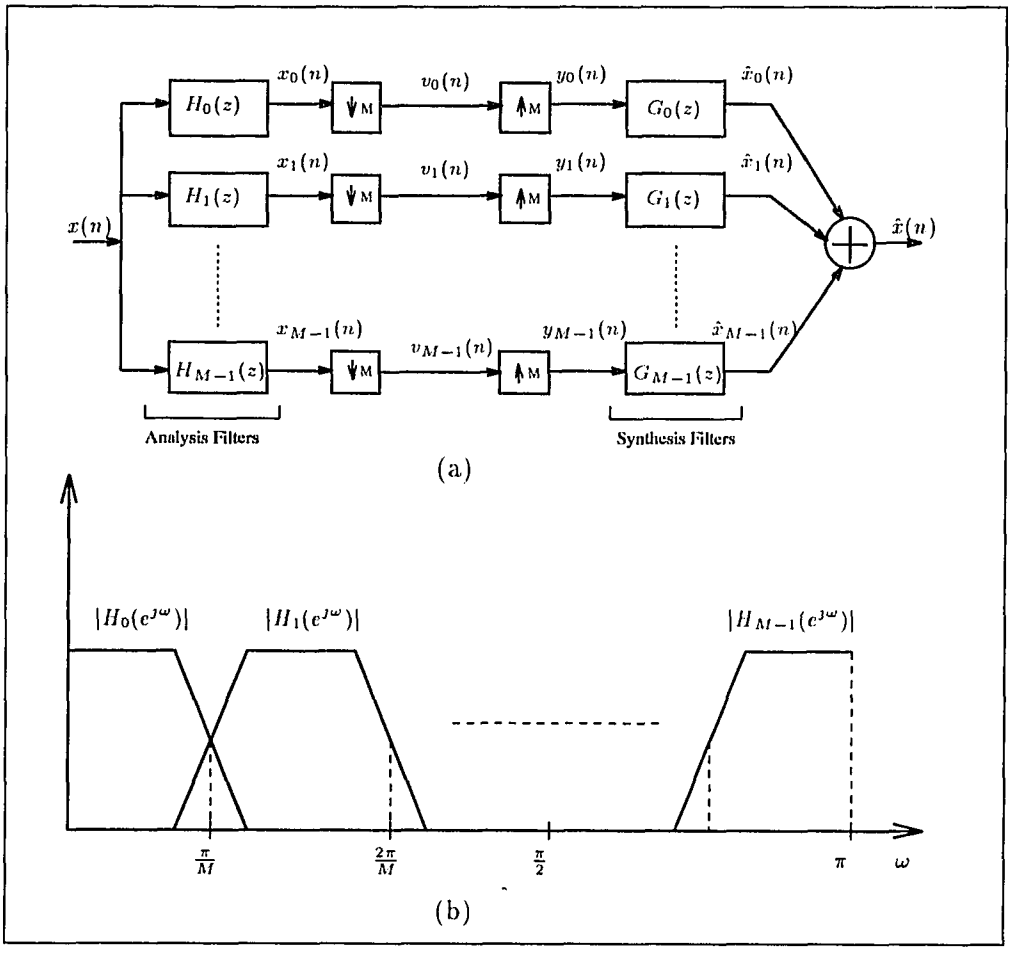

Figure 3.10 (a) Maximally decimated uniform M-band PR-QMF filter bank (b) Generic magnitude response for analysis filters.

$$\underline{X}_{AC}^{T}(z) \;=\; [\,X(z) \quad X(zW) \quad \ldots \quad X_{M-1}(zW^{M-1})\,]. \tag{3.47}$$

Then, the decimated signals have the following form:

$$\underline{V}(z) \;=\; \frac{1}{M}\mathbf{H}_{AC}^{T}(z^{1/M})\underline{X}_{AC}^{T}(z). \tag{3.48}$$

The output of the up-samplers are therefore,

$$Y_l(z) \;=\; V_l(z^M) \;=\; \sum_{k=0}^{M-1} H_l(zW^k)X(zW^k), \tag{3.49}$$

so that the output signal is

$$\begin{aligned}\hat{X}(z) \;&=\; \sum_{l=0}^{M-1} G_l(z)Y_l(z) \;=\; \frac{1}{M}\sum_{k=0}^{M-1} X(zW^k)\sum_{l=0}^{M-1} H_l(zW^k)G_l(z) \\ &=\; \sum_{k=0}^{M-1} T_k(z)X(zW^k),\end{aligned} \tag{3.50}$$

where

$$T_k(z) \;=\; \frac{1}{M}\sum_{l=0}^{M-1} H_l(zW^k)G_l(z). \tag{3.51}$$

The following vector notations will help to establish a vector-matrix form. The vector of synthesis filters is

$$\underline{G}^{T}(z) \;=\; [\,G_0(z) \quad G_1(z) \quad \ldots \quad G_{M-1}(z)\,], \tag{3.52}$$

and the equivalent filters' vector is

$$\underline{T}^{T}(z) \;=\; [\,T_0(z) \quad T_1(z) \quad \ldots \quad T_{M-1}(z)\,]. \tag{3.53}$$

Therefore, from Eq.(3.51), we notice that

$$\underline{T}(z) \;=\; \mathbf{H}_{AC}(z)\underline{G}(z), \tag{3.54}$$

where $\underline{T}(z)$ includes the branch filter $\{H_k(z)G_k(z)\}$ as well as its $(M-1)$ uniformly shifted versions. The presence of shifted versions is clearly due to the down-sampling/up-sampling coupling; namely, aliasing. Hence, the output can now be written as

$$\begin{aligned}\hat{X}(z) &= \underline{T}^T(z)\underline{X}_{AC}(z) \\ &= \frac{1}{M}\underline{G}^T(z)\mathbf{H}_{AC}^T(z)\underline{X}_{AC}(z). \end{aligned} \tag{3.55}$$

Clearly, in order to have alias cancellation

$$\underline{T} = \begin{bmatrix} MT_0(z) \\ 0 \\ \vdots \\ 0 \end{bmatrix}, \tag{3.56}$$

where $T_0(z)$ is the transfer function of the system. Given that Eq.(3.56) is satisfied, if $T_0(z)$ is all-pass and it is linear-phase such that $T_0(z) = cz^{-k_0}$ $(c \neq 0)$, then the system is free from aliasing, amplitude and phase distortion. Essentially, with the above conditions, we have an M-band filter bank with perfect reconstruction.

It was shown in [4][55] that in order to have a paraunitary M-band filter bank made up of FIR filters with N-coefficients, the necessary and sufficient condition is

$$\frac{1}{M}\tilde{\mathbf{H}}_{AC}(z)\mathbf{H}_{AC}(z) = \mathbf{I}, \tag{3.57}$$

where $\tilde{\mathbf{H}}_{AC}(z) \triangleq \tilde{\mathbf{H}}_{AC*}^T(z^{-1})$, and the subscripted asterisk implies conjugation of the coefficients in the matrix. This condition also ensures the power complementary property of analysis filters, which is to say

$$\frac{1}{M}\sum_k \left|H_k(e^{j\omega})\right|^2 = 1. \tag{3.58}$$

In [4], it is shown that the necessary and sufficient PR conditions for an FIR paraunitary filter bank with real-valued filter coefficients are as follows:

$$\Phi_{ij}(z) \triangleq \longleftrightarrow \rho_{ij}(n) = h_i(-n)h_j(n). \tag{3.59}$$

Then,

$$\rho_{ij}(Mn) = \sum_k h_i(k)h_j(k+Mn) = \delta(i-j)\delta(n). \tag{3.60}$$

In case of $i = j$, we notice that $\Phi_{ii} = H_i(z^{-1})H_i(z)$ is the transfer function of an M^{th} band filter and also $H_i(z)$ is a spectral factor of $\Phi_{ii}(z)$. Hence, Eq.(3.60) implies orthogonality, shift-orthogonality and normalization as

$$(1) \quad \sum_k h_i(k)h_i(k+Mn) = 0, \quad n \neq 0, \tag{3.61}$$

$$(2) \quad \sum_k h_i(k)h_j(k+Mn) = 0, \quad i \neq j, \tag{3.62}$$

$$(3) \quad \sum_k |h_i(k)|^2 = 1. \tag{3.63}$$

Within this framework, we aim to rank the methodologies of the filter bank design problem. The complexity of the design problem increases significantly and within practical limitations, one may not succeed in obtaining the desired solutions. So essentially, we will restrict our focus on paraunitary M-band systems with symmetries that help to reduce the complexity within the practical limits for moderate values of M ($M < 150$). Obviously, beyond $M > 150$, there is not much help either from theory or from existing technological tools.

Design Examples

In this section, we present the results of applying the discussed M-band design results in two cases. The first is a three-band PR-QMF with special symmetry, which will be explored next. The second is a linear-phase four-band PR-QMF solution.

(a) Three-Band Case:

The purpose of this example is to show PR-QMFs with an odd number of bands. In the general case, it is possible to have a linear-phase M-band solution for $M > 2$.

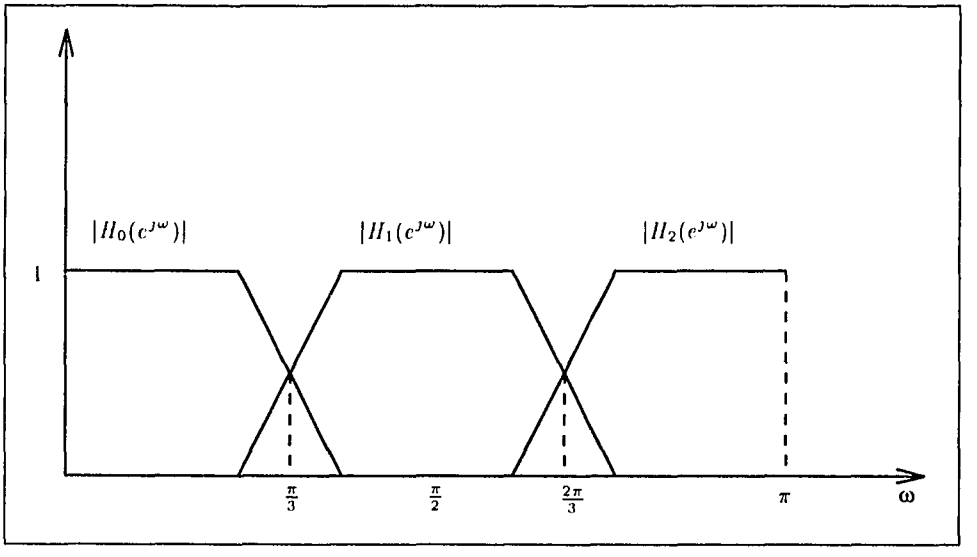

Figure 3.11 Magnitude responses for analysis filters of a generic three-band filter bank.

In some cases such as $M = 3$, however, additional features such as linear phase related symmetry impose more constraints. It was shown in Ref. [35] that if a filter bank has an odd number of bands M, PR is only possible if $(M+1)/2$ bands have symmetric impulse responses and $(M-1)/2$ bands have anti-symmetric impulse responses. Then, the frequency response $|H_{M-1-l}(e^{j\omega})|$ is taken as [55]:

$$\left|H_{M-1-l}(e^{j\omega})\right| = \left|H_l(e^{j(\pi-\omega)})\right|. \tag{3.64}$$

Indeed, Figure 3.11 shows magnitude responses for analysis filters of a generic three-band filter bank. It is clear that a bandpass filter can be chosen to be self-symmetric with respect to $\frac{\pi}{2}$, which immediately turns out to be [55]

$$H_1(z) = f(z^2), \tag{3.65}$$

where $f(.)$ is a real-valued FIR function. This is not the best symmetry solution, but it provides a solution under certain objective criteria. As a consequence of PR

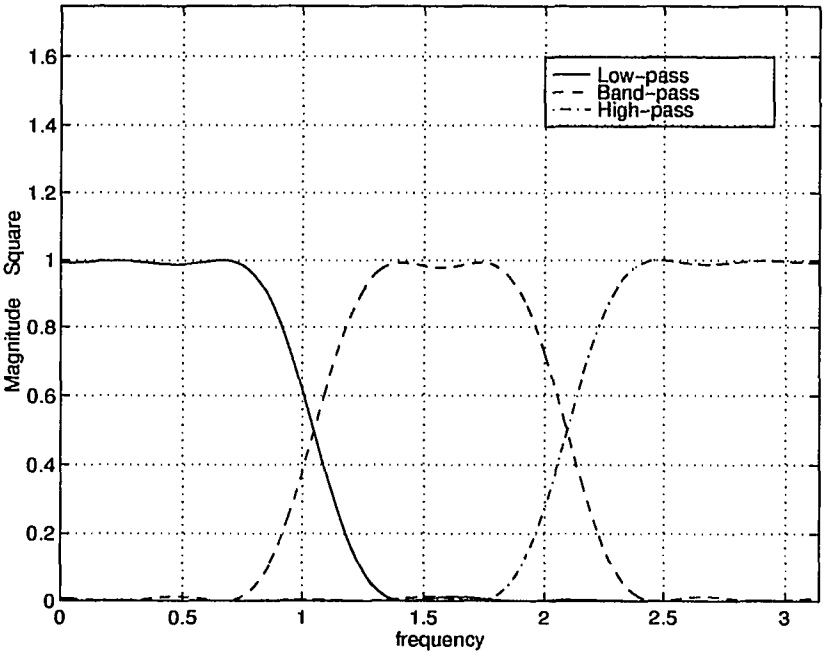

Figure 3.12 Magnitude response of the 15-tap analysis filters of a three-band PR-QMF bank with minimum stop-band energy.

conditions, one can show the filter lengths yields to be multiples of M (which is 3 in this case). Utilizing Eq.(3.64) as $H_2(z) = H_0(-z)$, $H_1(z) = f(z^2)$, and with PR constraints,

$$\begin{aligned} \sum_{k=0}^{(N-1)} h_i(k)h_i(k+3n) &= \delta(n) \\ \sum_{k=0}^{(N-1)} h_i(k)h_j(k+3n) &= 0 \end{aligned}$$

and clearly, zero-mean band-pass and high-pass filters bring two more additional constraints. Figure 3.12 displays a three-band PR-QMF solution for $N = 15$. The filters are optimized for minimum stop-band energy. The synthesis filters of this example are simple time reversal of analysis filters. This choice, however, necessitates the synthesis filters having the same magnitude response as expected.

(a) Four-Band Case:

In this example, we have chosen to impose linear phase and quadrature mirror

properties on the filter coefficients. Also, each analysis filter has a corresponding synthesis filter with a time-reversal relationship. The quadrature mirror and linear phase properties significantly reduce the number of variables and PR constraints. The set of analysis filters' coefficients will serve as the starting point for this example:

$$\begin{bmatrix} H_0 \\ H_1 \\ H2 \\ H3 \end{bmatrix} : \begin{bmatrix} h_0(0) & h_0(1) & \dots & h_0(\frac{N-1}{2}) & h_0(\frac{N-1}{2}) & \dots & h_0(1) & h_0(0) \\ h_1(0) & h_1(1) & \dots & h_1(\frac{N-1}{2}) & h_1(\frac{N-1}{2}) & \dots & h_1(1) & h_1(0) \\ h_1(0) & -h_1(1) & \dots & -h_1(\frac{N-1}{2}) & h_1(\frac{N-1}{2}) & \dots & h_1(1) & -h_1(0) \\ h_0(0) & -h_0(1) & \dots & -h_0(\frac{N-1}{2}) & h_0(\frac{N-1}{2}) & \dots & h_0(1) & -h_0(0) \end{bmatrix}. \tag{3.66}$$

Eq.(3.66) also shows that $H_2(z)$ and $H_3(z)$ have a zero-mean. The dimensionality for this case is two, and hence the total number of parameters to be optimized is N. Table 3.2 shows the 32-tap linear phase four-band PR-QMF filter bank solution for minimum time-frequency localization. The magnitude responses are given in Figure 3.13, respectively. The transform coding gain of a four-band PR-QMF bank for different filter lengths is shown in Figure 3.14. The input source is assumed to be the $AR(1)$ model. As the filter length increases, it is possible to obtain an improvement, but as seen in the figure, the gradient of the gain is marginal. This fact has been previously observed in image coding experiments.

The exact nature of the constraint reduction is tightly related to the filter interrelations as well as phase properties. Indeed, general filter banks may be designed without paraunitary condition. Paraunitary filter banks, however, ensures useful properties along with the perfect reconstruction property. Another design approach uses so called cosine modulated filter banks [55]. In this case, the set of analysis and synthesis filters are all obtained from cosine modulations of a low-pass PR-QMF prototype. Although this is a practical approach for large M, it significantly restricts the possible solutions.

Table 3.2 32-Tap, linear phase four-band PR-QMF filter bank solution for minimum time-frequency localization (the first 16-taps are shown).

Index	$H_0(z)$	$H_1(z)$	$H_2(z)$	$H_3(z)$
1	0.00478209	-0.00011715	-0.00011715	0.00478209
2	0.00011715	-0.00478209	0.00478209	-0.00011715
3	-0.00979620	0.00023988	0.00023988	-0.00979620
4	0.00023988	-0.00979620	0.00979620	-0.00023988
5	-0.02014862	-0.01048618	-0.01048618	-0.02014862
6	0.01048618	0.02014862	-0.02014862	-0.01048618
7	0.03398200	0.02166044	0.02166044	0.03398200
8	0.02166044	0.03398200	-0.03398200	-0.02166044
9	0.02154426	0.04543506	0.04543506	0.02154426
10	-0.04543506	-0.02154426	0.02154426	0.04543506
11	-0.09479339	-0.07508820	-0.07508820	-0.09479339
12	-0.07508820	-0.09479339	0.09479339	0.07508820
13	0.01966555	-0.20568533	-0.20568533	0.01966555
14	0.20568533	-0.01966555	0.01966555	-0.20568533
15	0.39975398	0.52734459	0.52734459	0.39975398
16	0.52734459	0.39975398	-0.39975398	-0.52734459

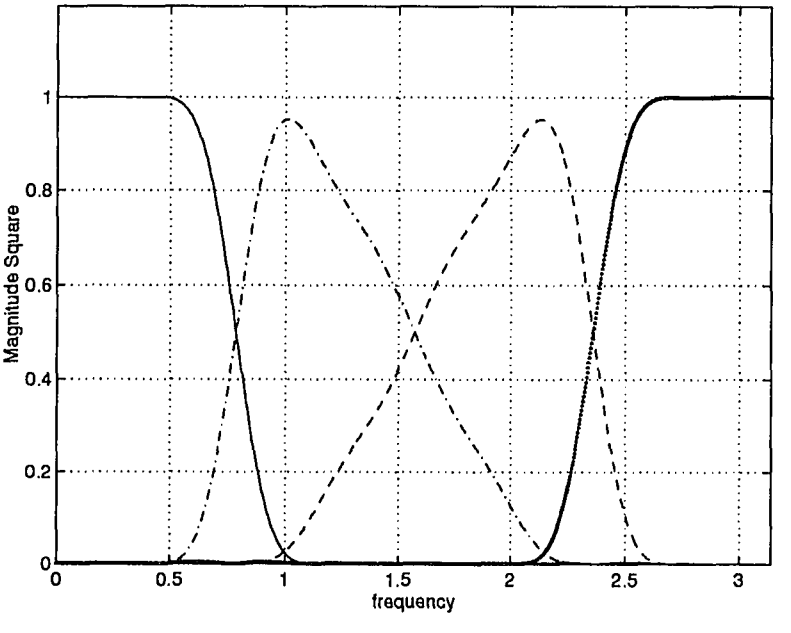

Figure 3.13 Magnitude square response of the 32-tap analysis filters of a four-band PR-QMF bank with minimum time-frequency localization.

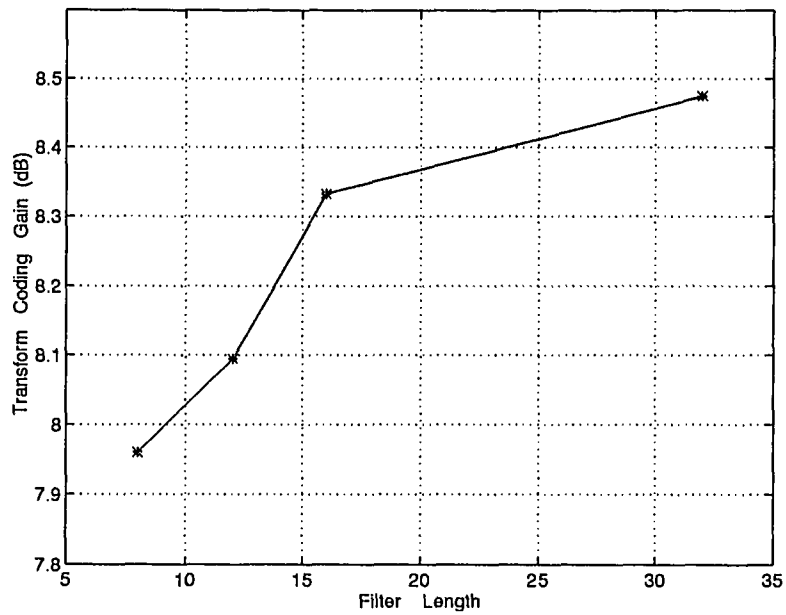

Figure 3.14 Transform coding gain of different length four-band PR-QMF banks.

3.4 Tree-Structured Filter Banks

Non-uniform filter banks decompose a given spectrum into sub-spectra of different bandwidths. In some applications, it is necessary to use such filter banks. Direct design of an M-band non-uniform bandwidth PR-QMF design raises difficult practical problems. On the other hand, non-uniform filter banks can be easily obtained by tree-structures. The two-band filter bank is the building block of tree-structured filter banks, although recently it was noticed that three-band may be also incorporated in order to achieve the desired spectral decomposition [49]. Simply, M-band is obtained by cascading two-band or three-band filter banks appropriately. Thus the product filters will be obtained by proceeding on the decimation stage of a subband tree structure. Suppose we have the following decimation branch and its equivalent structure, as shown in Figure 3.15(a)-(b).The equivalent filter is easily obtained as

$$H(z) = H_0(z)H_0(z^2)H_0(z^4). \tag{3.67}$$

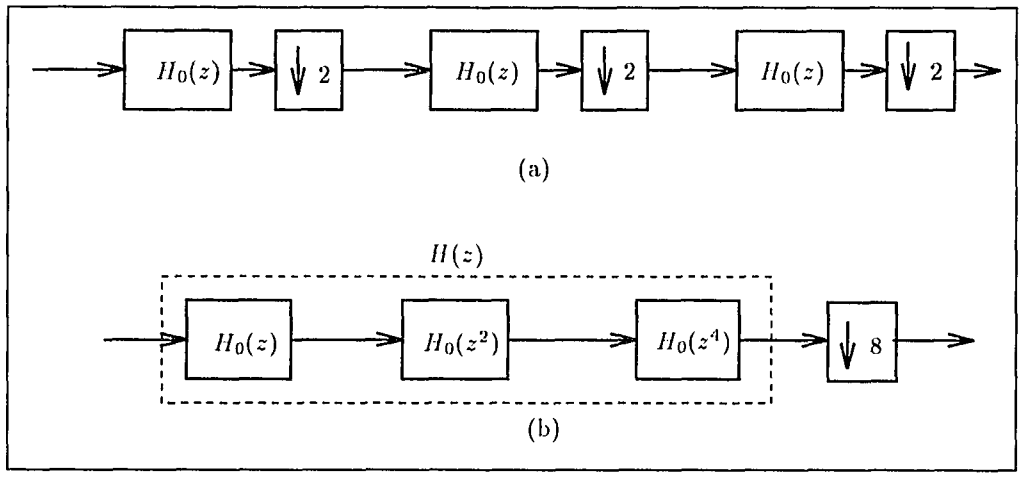

Figure 3.15 (a) Three-stage decimation, (b) its equivalent.

It is clear from Eq.(3.67) that by successively feeding a prototype low-pass filter with its up-sampled version (stretched in frequency), we obtain narrower frequency responses. To demonstrate this operation, the magnitude square responses of a 16-tap low-pass filter ($H_0(z)$) of a two-band PR-QMF bank and its up-sampled versions are displayed in Figure 3.16.

The binary tree structure is shown in Figure 3.17(a). Here a signal is split into two subbands, and after down-sampling, each subband is again split into two band and down-sampled $\{y_0(n)\ ,\ y_1(n)\ ,\ y_2(n)\ ,\ y_3(n)\}$. Clearly, the total structure is developed from nested two-band PR-QMFs. Suppose the filters $\{H_0(z),\ G_0(z),\ H_1(z),\ G_1(z)\}$, $\{H_0^I(z),\ G_0^I(z),\ H_1^I(z),\ G_1^I(z)\}$ and $\{H_0^{II}(z),\ G_0^{II}(z),\ H_1^{II}(z),\ G_1^{II}(z)\}$ satisfy PR conditions independently and so the overall structure can be also said to be PR as well. Figure 3.17(b) shows the equivalent four-band structure. Each filter in Figure 3.17(b) is realized as the product filter. Since there is no solution for the two-band linear phase PR-QMF, the M-band linear phase configuration can not be realized by nested two-band PR-QMFs.

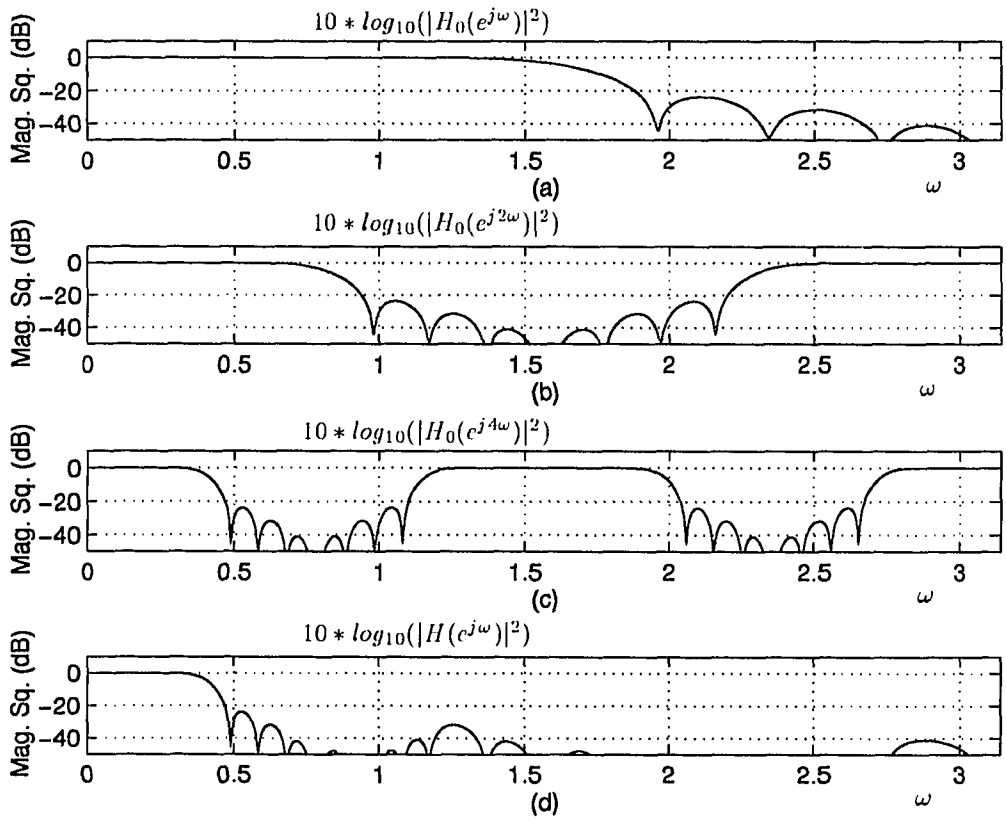

Figure 3.16 Magnitude square functions of (a) 16-tap low-pass prototype $H_0(z)$, upsampled versions (b) $H_0(z^2)$, (c) $H_0(z^4)$, and (d) the equivalent filter $H(z)$ obtained by multistage decimation.

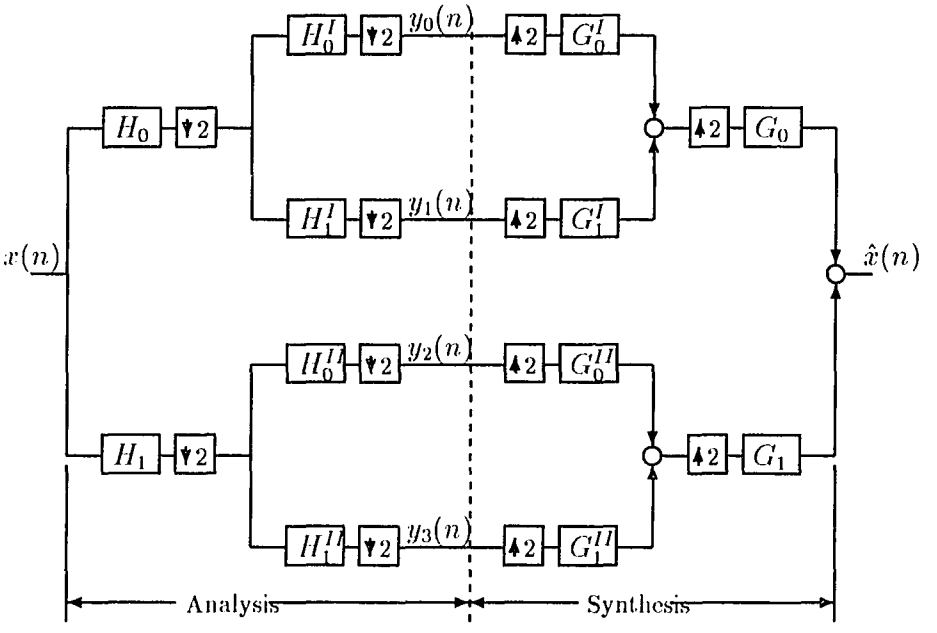

(a)

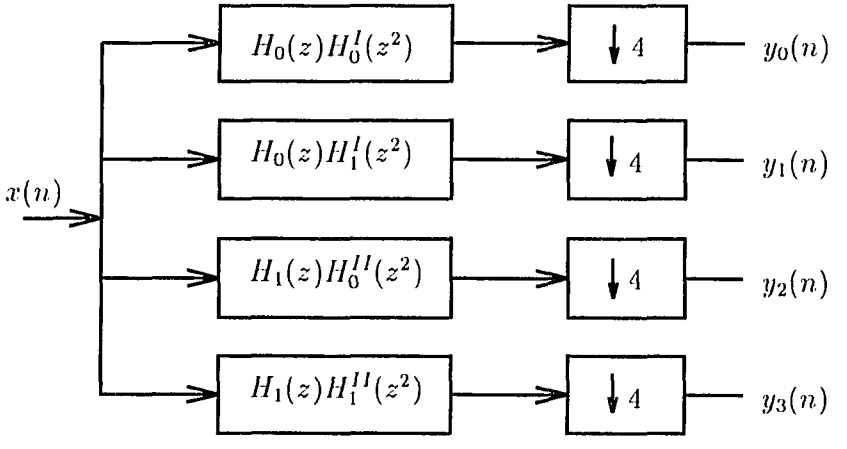

(b)

Figure 3.17 (b) Four-band two-level binary analysis/synthesis tree structure, (b) four-band single-level equivalent analysis filter bank.

The *dyadic* or octave-tree decomposition is obtained by successively decomposing just the low-pass signal in the tree structure. The three-level dyadic analysis filter bank and its ideal octave-band split are displayed in Figure 3.18(a)-(b). We see that the input signal has a rate of f_s and the output signals have rates of $f_s/2$, $f_s/4$, $f_s/8$ $f_s/8$, consecutively. As we move towards lower frequencies, the bandwidths of filters (similarly subbands) decrease in factors of two. Naturally, the frequency resolution of the lower frequency subband increases while higher frequency subbands preserve their time resolution. Thus, we can say that at any particular level, the low frequency component is the *coarse* approximation, and the high frequency term may be considered the *detail* at that resolution. Dyadic filter banks have been widely used in subband image and audio coding applications. If the four transfer functions $\{H_0(z), H_1(z), G_0(z), G_1(z)\}$ form a two-band PR-QMF bank, then the entire dyadic tree is PR if all the subbands have the same delay. The corresponding synthesis dyadic filter bank is shown in Figure 3.19.

Another type of tree structure is an irregular tree. In this case, a non-uniform decomposition is obtained. Any subband in a particular stage is split further if decomposition is justified. The irregular tree is the fundamental block of our discussion in Chapter 4. Therefore, we shall treat it in detail in the next chapter.

3.5 Progressive Optimality

In the M-band ($M > 2$) design framework, certain symmetries and mirror image properties may simplify particularly the non-linear optimization problem. In the general case, there are an infinite number of solutions in the problem. One major drawback arises from the richness of this situation— the convergence of the solution to the global optimum. Now, we will try to exploit this point for different design examples.

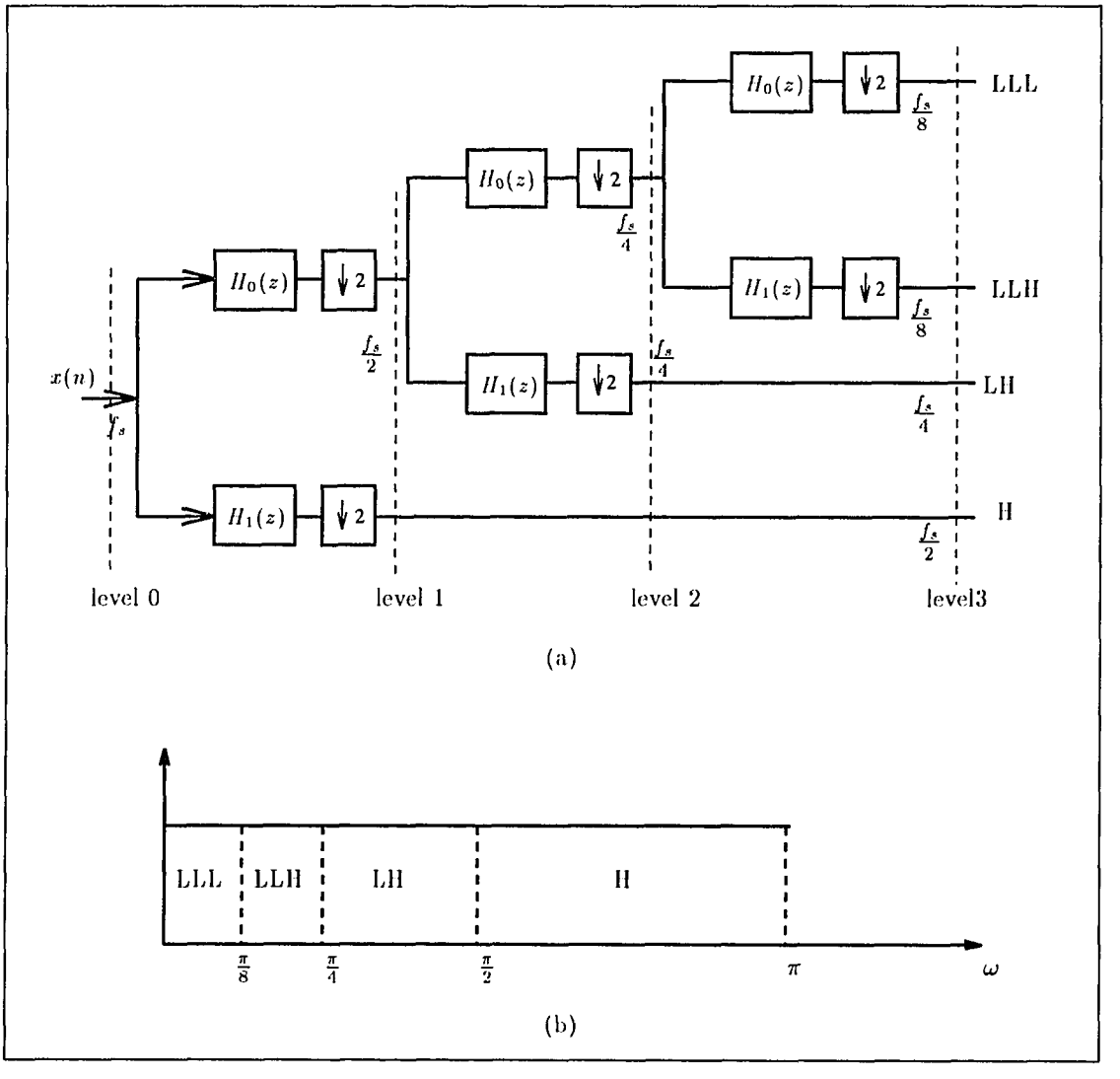

Figure 3.18 (a) Three-stage dyadic subband tree decomposition, and its (b) idealized spectral split.

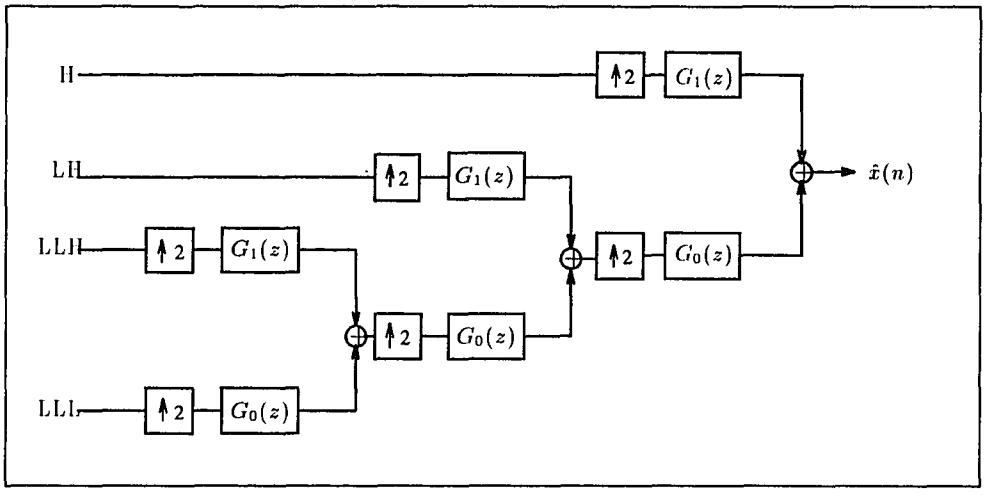

Figure 3.19 Three-stage synthesis dyadic filter bank.

Consider the direct M-band design problem displayed as a block diagram in Figure 3.20. The goal is to optimize the M-band solutions $\{S_1, S_2, \ldots, S_M\}$ constrained to $\underline{C}$, $\{C_1, C_2, \ldots, C_L\}$ with maximization (or minimization) of a certain optimality criterion (O). The vector $\underline{X}$ is an initial guess. For large values of M, the number of PR constraints become very large, even though paraunitary structures are utilized. Essentially, this condition will impose significant difficulties on the design. For $M > 150$, the direct design is very difficult within the existing optimization tool-boxes. Another practical design approach uses cosine-modulated M-band filter banks [55]. In this case, a PR-QMF low-pass prototype is designed first and the rest of the $(M-1)$ filters are obtained by the cosine modulation of that prototype. Although this is a practical solution to the problem, it may not yield robust solutions in all applications, because the solutions of M filters are simply restricted by a single prototype function.

On the other hand, an M-band subband decomposition can also be achieved by hierarchical filter banks. These structures try to achieve the spectral split in a repetitive fashion. In other words, the signal spectrum is split into its subspectra in

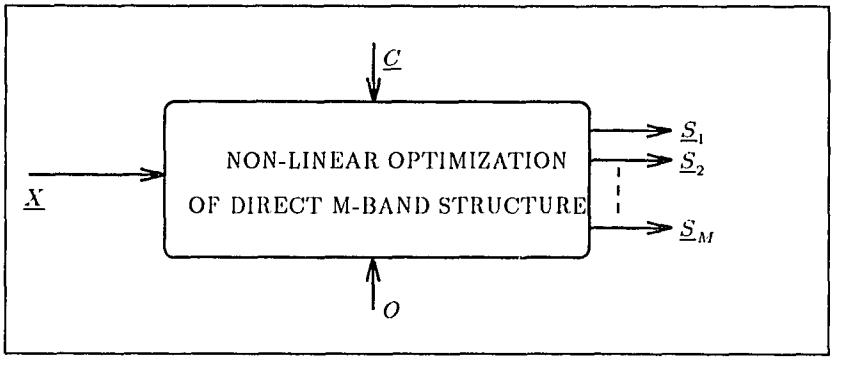

Figure 3.20 Schematic of optimal direct M-band design problem.

several stages of the hierarchy by using the same prototype filter bank. Figure 3.21 displays an eight-band regular subband tree using the same two-band PR-QMF in three steps of the hierarchy. The main problem here is that even though the prototype two-band PR-QMF is optimal, the product filters are not necessarily optimal. This can be shown with the following example. Figure 3.17(a) displays a two-stage, four-band, regular hierarchical subband structure. The two-band filter banks that are used in the different stages of the tree, even at each node of the same tree level, can be different for the most general case. All of the two-band filter banks employed in the tree are assured to be PR-QMF in order to satisfy the unitary property of the hierarchical structure.

The equivalent subband product filters for the regular tree displayed in Figure 3.17 can be easily found as

$$\begin{aligned} H_1(z) &= H_0(z)H_0^I(z^2), \\ H_2(z) &= H_0(z)H_1^I(z^2), \\ H_3(z) &= H_1(z)H_0^{II}(z^2), \\ H_4(z) &= H_1(z)H_1^{II}(z^2). \end{aligned} \tag{3.68}$$

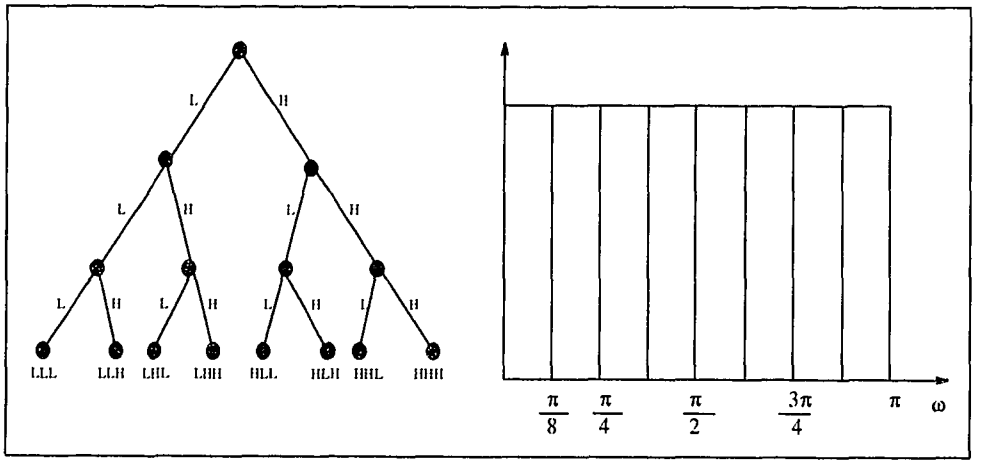

Figure 3.21 Eight-band regular tree and its ideal frequency decomposition.

Whenever the same prototype filter bank $[H_0^{(p)}(z)\ H_1^{(p)}(z)]$ is used in all of the nodes, say,

$$\left\{ \begin{array}{ccccccc} H_0(z) & = & H_0^I(z) & = & H_0^{II} & = & H_0^{(p)}(z) \\ H_1(z) & = & H_1^I(z) & = & H_1^{II} & = & H_1^{(p)}(z) \end{array} \right\},$$

then the conventional hierarchical subband tree structure is obtained. Now, the product filters become

$$\begin{aligned} H_1'(z) &= H_0^{(p)}(z)H_0^{(p)}(z^2), \\ H_2'(z) &= H_0^{(p)}(z)H_1^{(p)}(z^2), \\ H_3'(z) &= H_1^{(p)}(z)H_0^{(p)}(z^2), \\ H_4'(z) &= H_1^{(p)}(z)H_1^{(p)}(z^2). \end{aligned} \tag{3.69}$$

Obviously, the product functions in Eqs.(3.68) and in Eq.(3.69) are not necessarily equivalent; thus,

$$H_i(z) \neq H_i'(z), \qquad i = 1,2,3,4. \tag{3.70}$$

In the general case, an M-band filter bank may be obtained from hierarchical subband trees.

We have pointed out the difficulties with optimal M-band design; namely, (i) the direct structure M-band design (Figure 3.10) is too complicated for large values of M, (ii) cosine-modulated filter bank design is restricted with a single prototype. In a hierarchical M-Band filter bank (Figure 3.21) repetition of an optimal two-band PR-QMF does not yield optimal product filters. Now, we like to solve the optimal M-band filter bank design problem from the standpoint that optimal design criteria are still carefully monitored while the number of bands are increased without increasing the complexity of the design significantly. Indeed, we shall proceed with the very well known Ceasar's strategy, "*divide and conquer*," which we call *progressive optimality*.

Remark 1: The product subband filters in Eq.(3.68) are the special four-band PR-QMF solutions with the factorization properties. They provide the hierarchical as well as the direct split of the spectrum.

Remark 2: The time and frequency properties of the product filters, $H_i(z)$, $i = 1, 2, 3, 4$, along with the first level filters, $H_0(z)$ and $H_1(z)$, are important. Therefore, the intermediary filters of the second stage can be manipulated (since there are an infinite number of solutions) in order to achieve the desired time and frequency domain characteristics of the product filters. Thus, this observation naturally yields to the concept of progressive optimization in hierarchical M-band filter banks.

From the previous discussions it is essential we state that any M-band factorizable filter bank can be optimally designed step by step or progressively in a hierarchical tree structure. In each stage and branch, different filters are customized in order to achieve the desired optimality. Figure 3.22 displays the schematic of the progressive design procedure. For generalization, it is assumed that for a particular stage all the branches use a K-band structure, thus in this case $M = K^L$. For the i^{th} stage, the solutions from the previous stages $\{1, 2, \ldots, (i-1)\}$ are utilized. The optimal solution is searched for the overall objective function O_i, which is a function

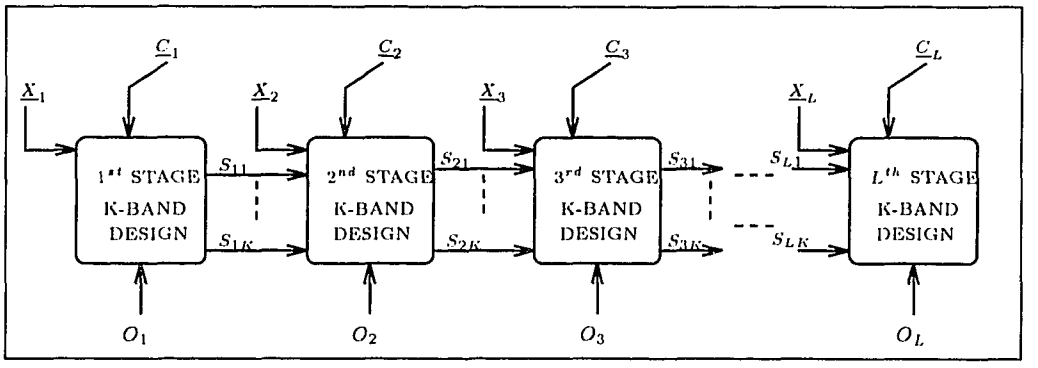

Figure 3.22 Progressive optimization schematic of M-band hierarchical structure.

of all previous filters and the actual filters. Hence,

$$O_i(S_{11}, S_{12}, \ldots, S_{1K}, \ldots, S_{i1}, S_{i2}, \ldots, S_{iK}) = f(S_{11}, S_{12}, \ldots, S_{1K}, \ldots, \ldots, S_{i1}, S_{i2}, \ldots, S_{iK}), \quad (3.71)$$

where $f(.)$ is usually a nonlinear function and $\{\underline{X}_1, \underline{X}_2, \ldots, \underline{X}_i\}$ are independent initial conditions for different stages. The final product filters $[H_0(z), \ldots, H_{M-1}(z)]$ are functions of branch filters $S_{ij}(z)$, $(i = 1, .., K; j = 1, .., K)$. For example, the low-pass of the M-band equivalent can be written as [4]

$$H_0(z) = S_{11}(z)S_{21}(z^K) \ldots S_{L1}(z^{(\frac{M}{K})}) \quad (3.72)$$

Thus, the optimization algorithm is displayed in Figure 3.23. Hence, the progressively optimal design of the M-band (L-stage) filter bank can be summarized as:

begin

initialize

while $(k \leq L)$

set

{PR Constraints, k^{th} stage initial conditions, additional constraints}

Optimize (k^{th}) stage filters with respect to O_k

$k = k + 1$

end

Generate product filters

end

Now, let us consider the two-stage four-band filter bank given in Figure 3.17. For this example, the progressive design procedure is as follows:

(i) First, an optimal two-band PR-QMF solution for the first stage is searched based on the design criteria.

(ii) Then, an intermediary two-band PR-QMF solution that optimizes the product subband filters is searched. Therefore, the product subband filters of Eq.(3.69) are tuned to satisfy the desired criteria of optimality, e.g. energy compaction, frequency localization, joint time-frequency localization, etc. [46][45].

Figures 3.24 and 3.25 display the time and frequency functions of two different hierarchical filter bank scenarios. Table 3.3 provides the time and frequency localizations of the product subband filters of those hierarchical filter banks. Figures 3.24-3.25 and Table 3.3 imply the richness of possible product function solutions with different time-frequency properties. Figures 3.26 and 3.27 display the frequency functions of the optimal two- and progressively optimal four-band product subband filters. The optimalities in these examples are based on joint time-frequency localization and energy compaction. In these figures, the optimal first stage two-band 6-tap PR-QMFs are designed. Then, in the second stage, two-band 4-tap PR-QMF solutions are searched in order to achieve the optimal 12-tap product subband filters based on the design criteria.

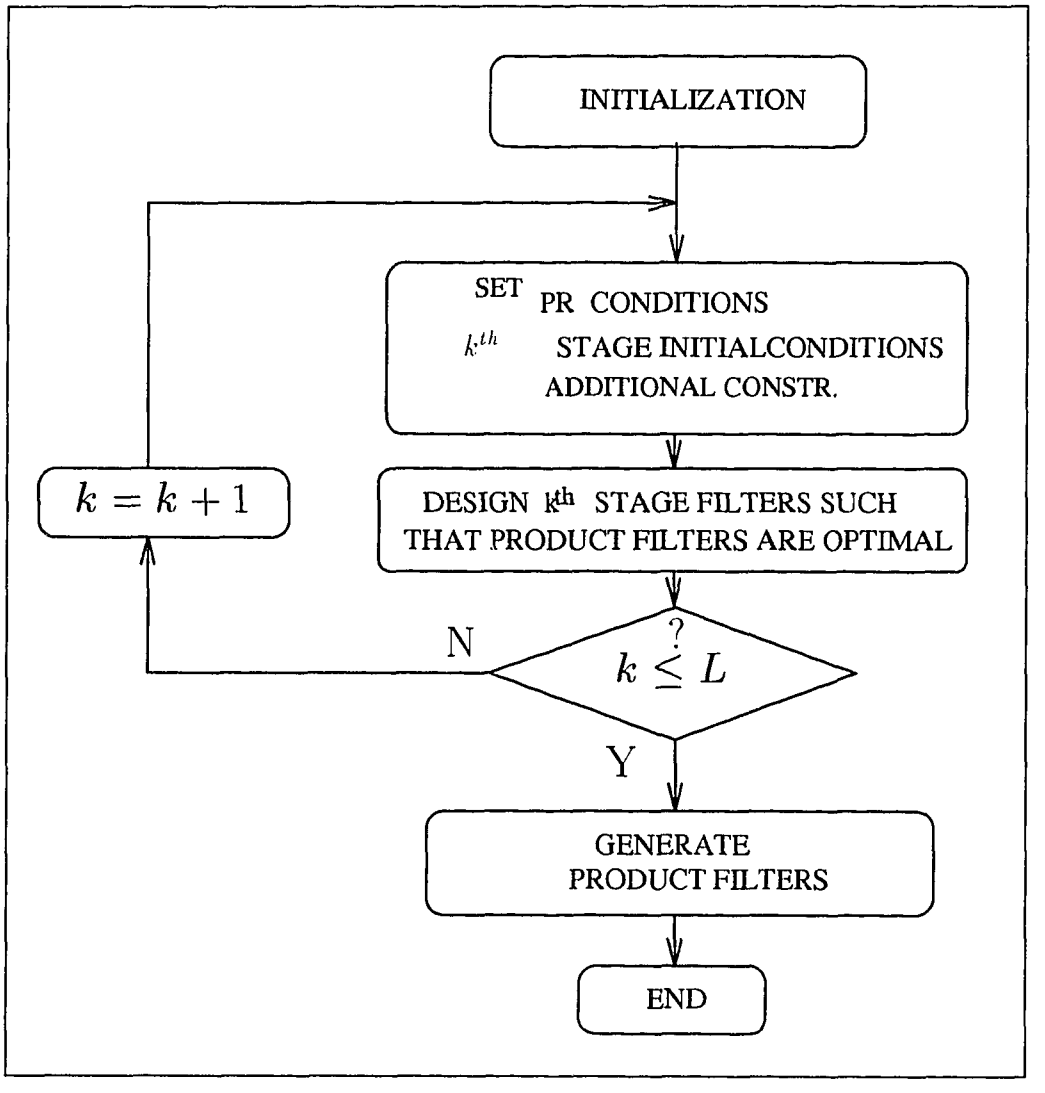

Figure 3.23 Flow diagram of progressive optimality algorithm.

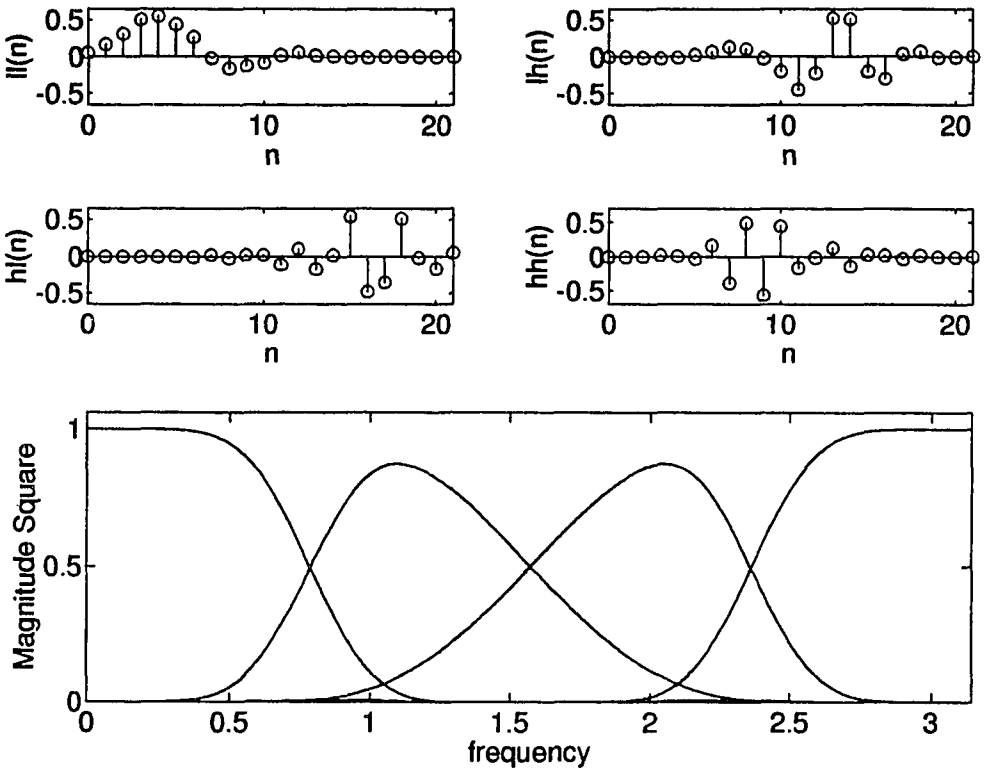

Figure 3.24 Time and frequency functions of the product subband filters in a 2-level, four-band hierarchical filter bank using an 8-tap Binomial QMF-Wavelet filter bank [4] repetitively at any node of the tree.

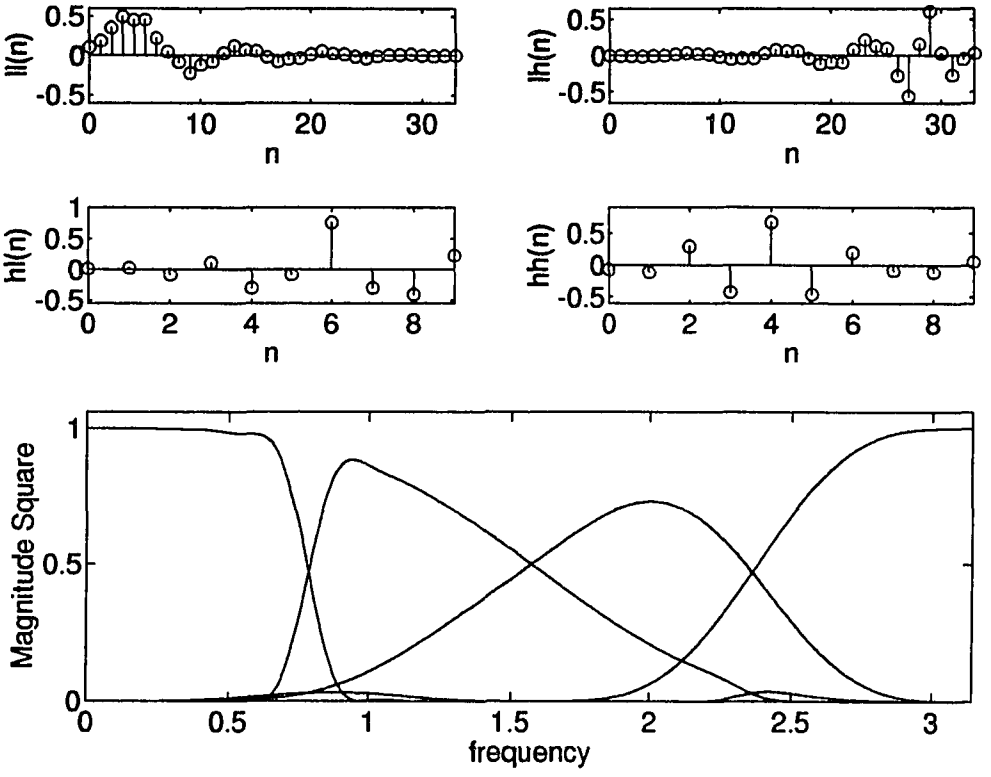

Figure 3.25 Time and frequency functions of the product subband filters in a 2-level, four-band hierarchical filter bank using a 4-tap Binomial QMF-Wavelet filter bank [4] at the first stage, a 16-tap version at the low, and a 4-tap version at the high-pass node of the second stage.

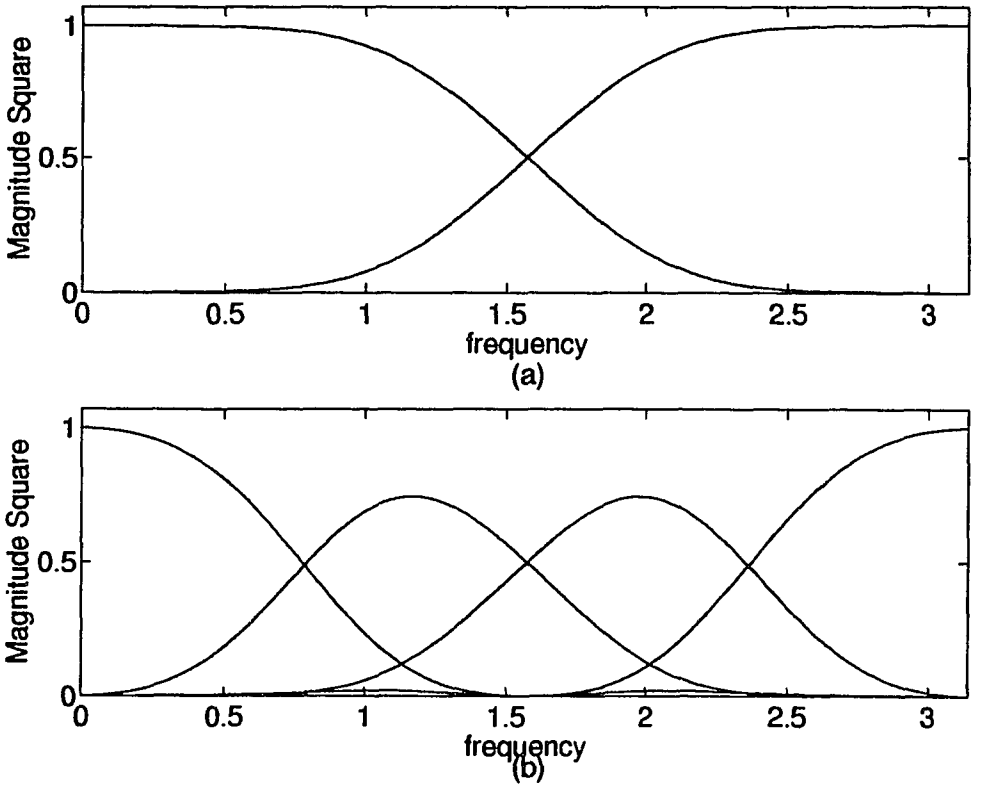

Figure 3.26 The frequency functions of a (a) 6-tap optimal two-band PR-QMF (optimality is based on the minimization of the joint time-frequency spread), (b) 12-tap product subband filters of progressively optimal four-band PR-QMF (optimality is based on the progressive optimization of the product filters with the minimization of the joint time-frequency spread).

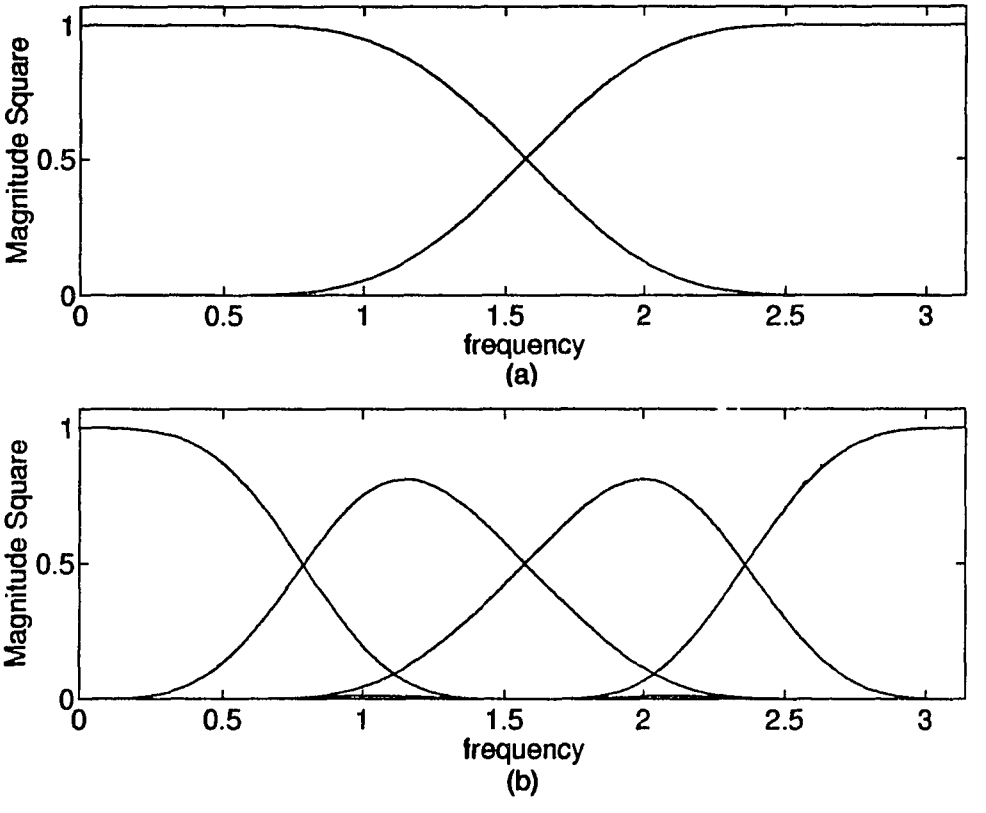

Figure 3.27 The frequency functions of a (a) 6-tap optimal two-band PR-QMF (optimality is based on the energy compaction measure), (b) 12-tap product subband filters of progressively optimal four-band PR-QMF (optimality is based on the progressive optimization of the product filters with the energy compaction measure).

Table 3.3 Time and frequency localizations of hierarchical filter banks displayed in Figures 3.24, 3.25, 3.26 and 3.27.

	$\overline{\omega}$	$\overline{n}$	σ_ω^2	σ_n^2	$\sigma_\omega^2 \times \sigma_n^2$
B-QMF Hierarchical four-band Tree (22 tap product filters)	0	4.05	0.2526	2.7261	0.6886
	1.23	12.88	0.1222	3.8269	0.4676
	1.91	16.28	0.1222	2.7757	0.3392
	π	8.80	0.2526	2.2622	0.5714
Hierarchical 4-Band Tree: 4-tap B-QMF at the first stage, 16-tap B-QMF at the low and 4-tap B-QMF at the high-pass nodes of the second stage	0	4.5535	0.2857	9.8246	2.8072
	1.31	27.1486	0.1447	10.1603	1.4712
	1.88	6.3267	0.1718	1.7254	0.2964
	π	3.9722	0.3697	1.4089	0.5210
Progressively optimized four-band tree, 12-tap product filters (optimality is based on minimization of joint time-frequency spread of the filters)	0	1.8695	0.3562	1.1751	0.4186
	1.20	5.8878	0.1623	1.6811	0.2730
	1.94	8.8042	0.1623	1.6811	0.2730
	π	5.4382	0.3562	1.1751	0.4186
Progressively optimized four-band tree, 12-tap product filters (optimality is based on the energy compaction measure)	0	2.5664	0.2910	1.5319	0.4458
	1.21	5.6715	0.1385	2.2932	0.3177
	1.93	7.9264	0.1385	1.9780	0.2740
	π	5.8354	0.2910	1.3592	0.3955

The design of irregular spectral decomposition tools, irregular in the frequency bandwidths as well as in the time domain properties, can be monitored level-by-level in the subband tree. This approach allows the designer to tune the time and frequency properties of the transform basis to the constraints of the application at hand. The intermediary filters of a given node in the subband tree define the time and frequency properties of the corresponding product subband functions. The repetitive use of an optimal filter bank does not yield the optimal product subband functions in a hierarchical structure.

3.6 A Note on Wavelets

The continuous and discrete wavelet transforms are defined on a continuous time variable. An infinite stage discrete-time dyadic subband tree is the analytical tool to design a band-pass analog wavelet and its complementary low-pass scaling function. Therefore, the two-band perfect reconstruction quadrature mirror filter bank plays a vital role in the theory of compactly supported orthonormal wavelet transforms. The fundamental wavelet and scaling equations lead to the infinite product frequency domain relations as [11][4]:

$$\Psi(\Omega) = H_1(e^{j\omega/2}) \prod_{k=2}^{\infty} H_0(e^{j\omega/2^k}), \tag{3.73}$$

$$\Phi(\Omega) = \prod_{k=1}^{\infty} H_0(e^{j\omega/2^k}), \tag{3.74}$$

where $\Psi(\Omega)$ and $\Phi(\Omega)$ are Fourier transforms of the wavelet and scaling functions. These frequency-domain equations show that continuous-time wavelet and scaling functions are obtained by the infinite products of the Fourier transforms of the discrete-time interscale coefficients $h_0(n)$ and $h_1(n)$, with normalized frequencies $\omega = \Omega$. This is a very important property of multiresolution analysis theory, which allows us to design continuous-time functions by designing discrete-time functions. The dyadic subband tree can serve as the fast wavelet transform algorithm if the transform process is properly initialized. The proper initialization step is the projection of the analog signal onto the scaling space at the full resolution. The sampled data is assumed as the scaling coefficients of wavelet transform theory in most applications reported in the literature. Therefore, they are doing exactly what a discrete-time filter bank does. The wavelet transform on discrete-time signals implies an imperfect representation and is theoretically incomplete. Additionally, from our previous discussion, two-band filter banks used in the different stages of the tree, even at each node of the same tree level, can be different for the most general

subband transform case. The infinite resolution products of the discrete-time inter-scale coefficient sequences of the wavelet and scaling bases merge with the analog wavelet and scaling functions in the Fourier domain, as given in Eqs.(3.73) and (3.74). In reality, all of the analog wavelet and scaling functions displayed by the researchers in the literature are generated by using only 10-15 terms, rather than the infinite resolution required in Eqs.(3.73) and (3.74). Therefore, the practical merits of the optimal wavelet designs based on a prototype two- or M-band optimal discrete-time filter bank need to be seriously questioned. Cohen and Sere also pointed out this concept from a wavelet point of view [1].

3.7 Remarks on Image Coding

The dyadic ten-band and hierarchical 64-band, separable 2-D subband transforms are employed to test the practical impact of using different filter banks in different levels of the hierarchical structures. The available bits are optimally allocated among the subbands based on their variances. Then, uniform quantizers are employed in the generic subband image codec algorithm. The image coding performance of several hierarchical filter bank scenarios are tested. Figures 3.28 and 3.29 display the rate-distortion curves of different 10-band and 64-band 2-D subband codecs for the test images, LENA and BUILDINGAlso, Figure 3.30 compares 10-band and 64-band subband image codecs under the same conditions. The 10-band dyadic tree performs as well as 64-band full tree but with significantly reduced complexity. These figures also indicate different filters employed in the considered hierarchical subband coding experiments. The first index implies the filter used in the first level of the subband tree and the others follow similarly. The known PR-QMF families in the literature are used in these experiments. It is observed from the figures that the different image coding performances are obtained with different subband filter banks. This result is due to different time-frequency properties of the product subband functions of filter

banks employed in the coding experiments. Marginal performance improvements are possible by using different filter bank cells in different levels. In Appendix A, perceptual image coding performance examples are shown for different bit rates. More experimental studies to find the best possible filter bank configurations for certain image families are topics of future research. Future studies should also focus on the subjective coding performance of the subband transform bases.

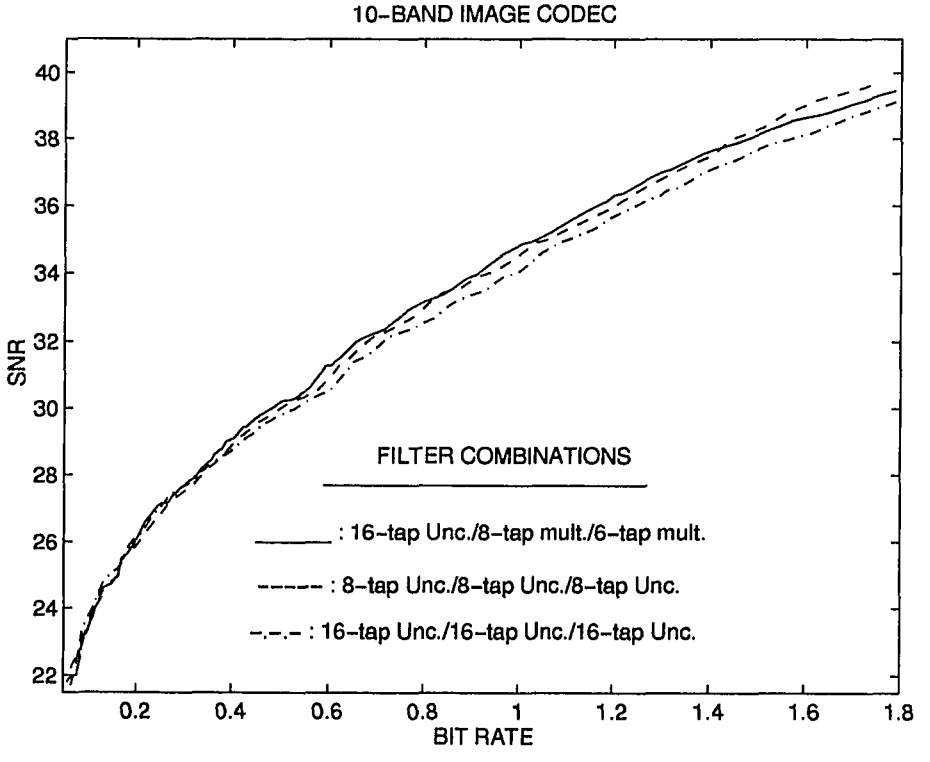

Figure 3.28 10-band 2-D Image codec rate-distortion performance for different filter combinations.

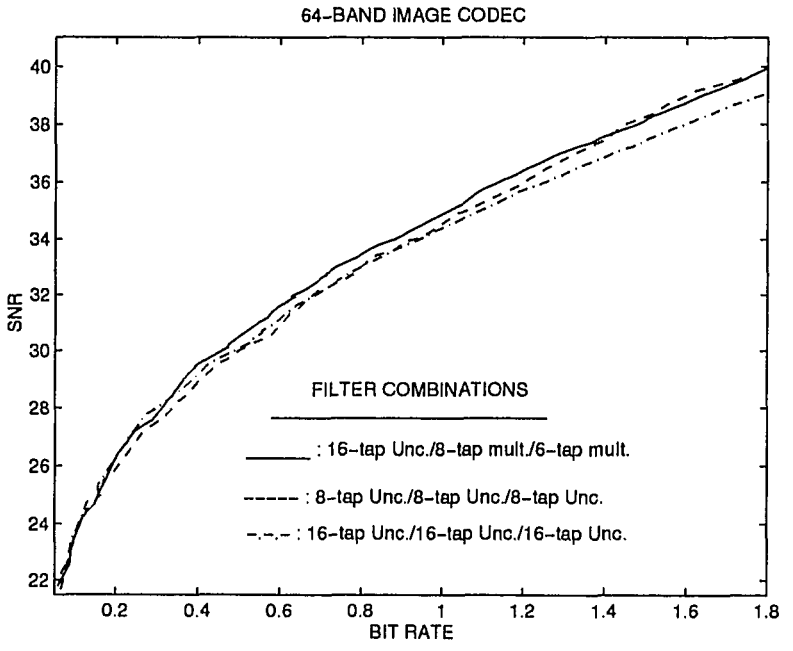

Figure 3.29 64-band 2-D Image codec rate-distortion performance for different filter combinations.

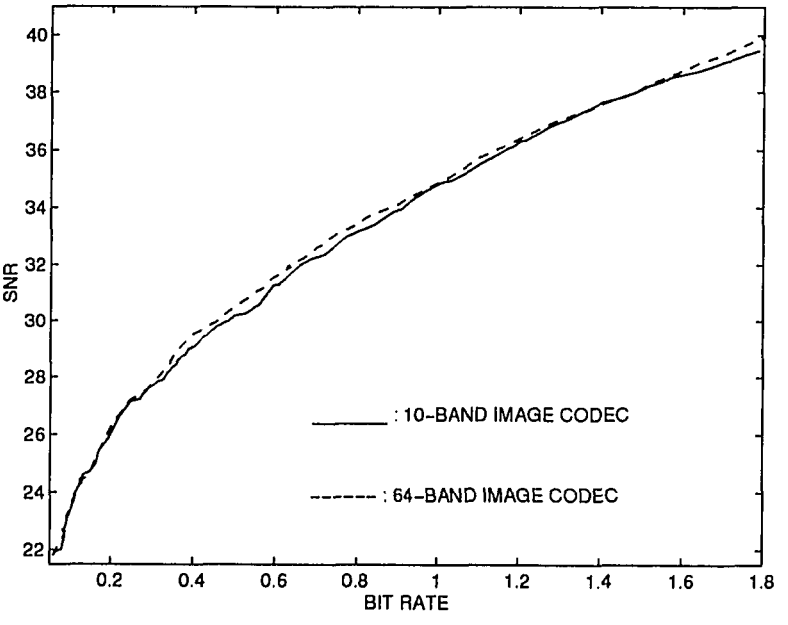

Figure 3.30 Performance comparison of 10-band dyadic and 64-band regular subband codec for same filter combinations

CHAPTER 4

ADAPTIVE FILTER BANKS

In the previous chapter we have given a thorough examination of M-band filter bank design along with some design examples. So far we dealt with stationary structures in the sense that the filters in the filter bank are fixed so that the tree structure itself is fixed. We can easily extend this to the concept of adaptive analysis-synthesis systems. The adaptiveness is not conventional weight iteration or updating but instead adapting the filter bank to the particular signal at hand. This terminology has been frequently used in multiresolution signal processing community [9][22] and it should not mislead the reader to the very well known definition of adaptive signal processing. Given proper adaptation rules, we shall see in examples that we do not have the convergence problem in a conventional sense. The two key points in the adaptive filter bank concept are: **(i)** that the orthogonality and perfect reconstruction are maintained while changing the adapting or changing the filter bank structure, and **(ii)** that an adaptation algorithm keeps track of changes in the input signal.

Recently, other researchers provided new results on the subject of time-varying filter banks [34], which are different from the perspective here. The tree-structuring algorithm discussed in this chapter was first mentioned in an earlier study [5].

4.1 Best Basis Functions Selection

The basis functions for the linear expansion of signals are usually chosen from infinite possible solutions. So generally speaking, it is always desirable to have a set of basis functions by which we represent a given input signal $y(k)$ by

$$y(k) = \sum_{l=1}^{M} \alpha_l \phi_l(k), \tag{4.1}$$

where the set $\{\phi\}$ is chosen optimally based on an objective criterion. For example,

if the objective is decorrelation of transform coefficients then the KLT is optimal in a statistical sense. In other words, the design or selection of KLT basis functions with decorrelation criteria is optimal [4].

A natural question that arises in connection with basis selection is how to choose the objective or optimality criteria. The decomposition of a signal usually reveals transform domain properties. The emphasis of different properties essentially yields different optimality criteria. Now, we can define the best basis selection problem. The projection of a signal in R^N onto a set of basis functions with the optimization of a certain objective criterion is called the *best basis selection* problem.

In some cases, it is possible to analyze the input signal or predict its features. If this advantage is utilized in basis design, drastic improvements over fixed transforms are naturally expected. On the other hand, The DFT and DCT have standard features which may apply very well to certain classes of signals [1]. In recent years, multirate filter banks naturally evolve for a better understanding of time-frequency behaviour of discrete-time signals. M-band filter banks usually provide better time-frequency representation with the price of longer duration basis functions. We have seen in the previous chapter, however, that optimal M-band design is not an easy task if M is a considerably large number ($M > 128$). Adaptive (on the fly) optimization of M-band filter banks, in particular, is almost an impossible task. This fact leads us to suboptimal but more practical and efficient solutions. For example, if a certain degree of frequency localization is present in the particular signal at hand, then we will show that a tree-structured M-band solution that is properly tailored to the input signal exists. Hence, here we will consider the *best basis selection* problem as the *best tree-structured filter bank selection* for the input signal. Although this is a suboptimal solution, we shall see in the following chapters that it will bring significant improvement over the fixed transforms. Considering the price paid for additional computational burden, adaptive transformation algorithms necessarily provide a set

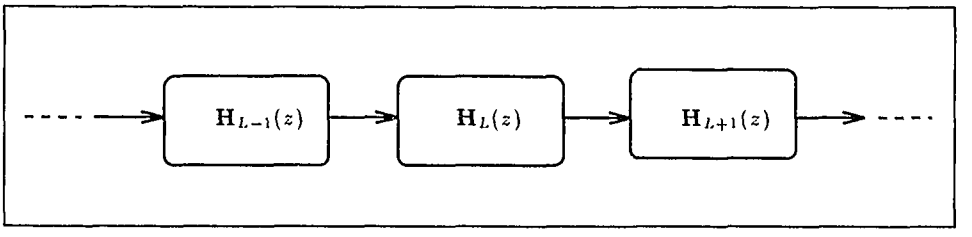

Figure 4.1 Cascaded paraunitary systems.

of orthonormal basis functions that represent the given signal better than the fixed transforms do. The key for achieving adaptive transforms is then tailoring the basis functions (subband filters) for the given input signal.

4.2 Adaptive Subband Tree-Structuring Algorithm

In Chapter 3 we briefly discussed regular binary and dyadic subband tree structures. We mentioned that a tree-structured filter bank is a practical tool for obtaining an M-band filter bank. In this section we investigate adaptive filter banks that allow us to change the tree structure while preserving the paraunitary property. Suppose we have the cascaded paraunitary system displayed in Figure 4.1 Given that each block in Figure 4.1 is paraunitary such that

$$\tilde{\mathbf{H}}_i \mathbf{H}_i \;=\; M\mathbf{I}, \tag{4.2}$$

where $\tilde{\mathbf{H}}$ is the conjugate transpose of $\mathbf{H}$. Then, the cascaded system is said to be paraunitary, as

$$(\ldots \tilde{\mathbf{H}}_{L-1}\tilde{\mathbf{H}}_L\tilde{\mathbf{H}}_{L+1} \ldots)(\ldots \mathbf{H}_{L-1}\mathbf{H}_L\mathbf{H}_{L+1} \ldots) \;=\; C\mathbf{I},$$

or, equivalently,

$$\prod_i \tilde{\mathbf{H}}_i \mathbf{H}_i \;=\; C\mathbf{I}, \tag{4.3}$$

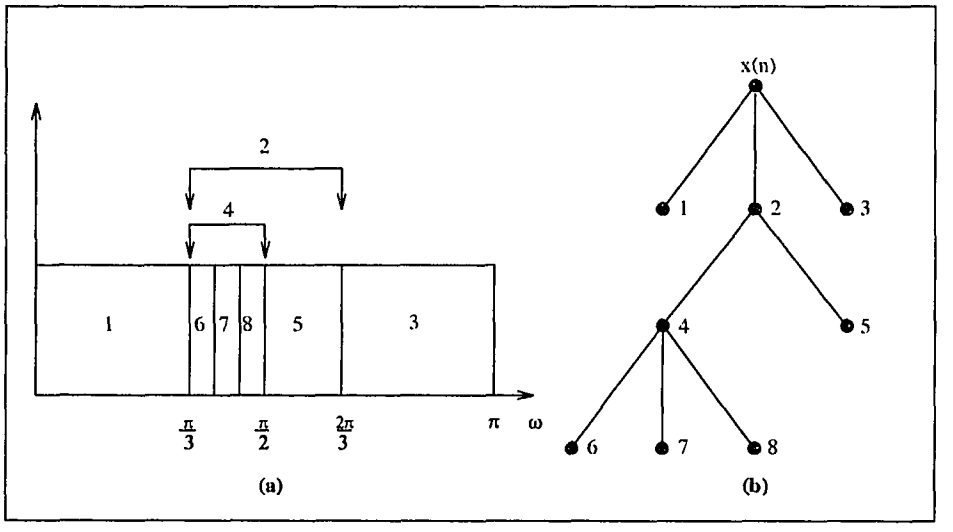

Figure 4.2 An irregular tree structure (a) its ideal spectral decomposition, (b) tree structure for (a).

where $\mathbf{I}$ is the identity matrix. Essentially, a hierarchical filter bank structure is paraunitary if and only if each branch of the hierarchy is paraunitary. If this is so then that structure can be said to be instantaneously paraunitary and it sufficiently satisfies the PR.

Besides full-band and dyadic trees, irregular tree structures bring flexibility to the signal decomposition problem. Figure 4.2 displays one possible example for the eight-band structure. One other important issue here is the delay synchronization between different branch filters. Clearly, different branch filters may have different durations. Unless a full-band tree is used, delay synchronization must be provided, otherwise PR can not be satisfied.

The discussion so far has been concerned with tree-structured subband transforms and their orthogonality properties. Now, we shall present how the adaptation of the subband tree structure is performed. First of all, it is essential that we have a *decision rule* for interacting decisions during adaptively growing the tree structure. At a particular node, a node metric $m_k(i,j)$ is calculated for the i^{th}

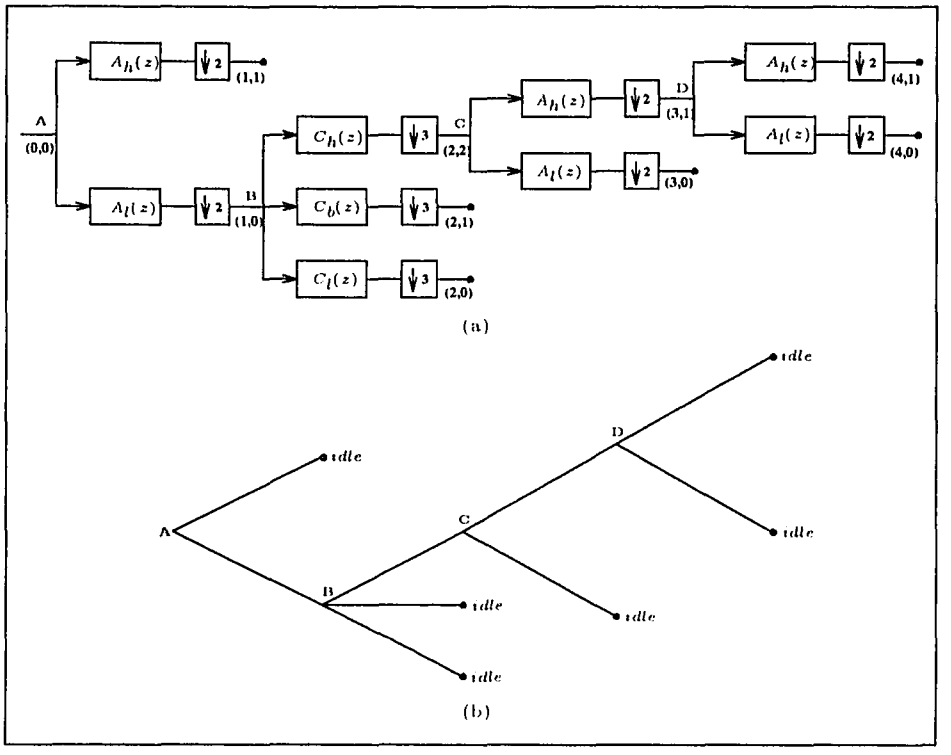

Figure 4.3 Six-band irregular hierarchical subband decomposition (a) actual implementation, (b) tree diagram for (a).

stage, j^{th} node and k is the running index for k different M-band filter bank schemes. In general, two-band decomposition is not the only possibility in tree-structuring. In fact, utilization of "only" the two-band solution is restricting the decomposition problem significantly. At any node under consideration, the decision rule must perform two different decisions:

(I) continue or terminate further splitting of that particular node,

(II) if decision (I) is justified for further splitting then choose M-band splitting.

These rules are evaluated for every decomposition possibility. The first node is called the *root*; similarly the particular node under consideration is called the *active node*. If a splitting decision is made for an active node then the *children nodes* are born and

the active node becomes the *parent node*. During tree growing, if any active node is terminated from further splitting, it becomes an *idle node*.

Now, in order to have a better understanding, we shall discuss the following example shown in Figure 4.3 before we present the generic adaptive tree-structuring algorithm. Figure 4.3(a) displays the hierarchical decimation stages; the corresponding tree diagram is shown in 4.3(b). In this example, a two-band low-pass/high-pass prototype analysis PR-QMF banks $[A_l(z), A_h(z)]$ and/or a three-band low-pass/band-pass/high-pass analysis PR-QMF banks $[C_l(z), C_b(z), C_h(z)]$ are utilized in each generated stage. We notice that the effect of cascade of decimation stages yield similar stop-band attenuation as discussed in section 3.4. At point **A**, node **(0,0)** is the root and active node. The node metrics $m_2(0,0)$ (for two-band PR-QMF) and $m_3(0,0)$ (for three-band PR-QMF) are calculated first. According to decision rule (I), if any of these metrics exceed a certain threshold then rule (II) is evaluated by comparing $m_2(0,0)$ and $m_3(0,0)$. Evidently, the root node **(0,0)** becomes the parent node for nodes **(1,0)** and **(1,1)**. In the first stage, further splitting for node **(1,1)** is not justified, so it becomes idle. On the other hand, the active node **(1,0)** proceeds with three-band splitting as decision rules (I) and (II) suggest. In second stage, nodes **(2,0)** and **(2,1)** are idle while node **(2,2)** is active and two-band splitting is performed. This process continues until all nodes become idle. The nodes at points **A**, **B**, **C** and **D** are active nodes during adaptation. Thus, the idle nodes represent the final product filters as:

$$\begin{aligned} E_0(z) &= A_h(z) \\ E_1(z) &= A_l(z)C_l(z^2) \\ E_2(z) &= A_l(z)C_b(z^2) \\ E_3(z) &= A_l(z)C_h(z^2)A_l(z^6) \\ E_4(z) &= A_l(z)C_h(z^2)A_h(z^6)A_l(z^{12}) \end{aligned} \tag{4.4}$$

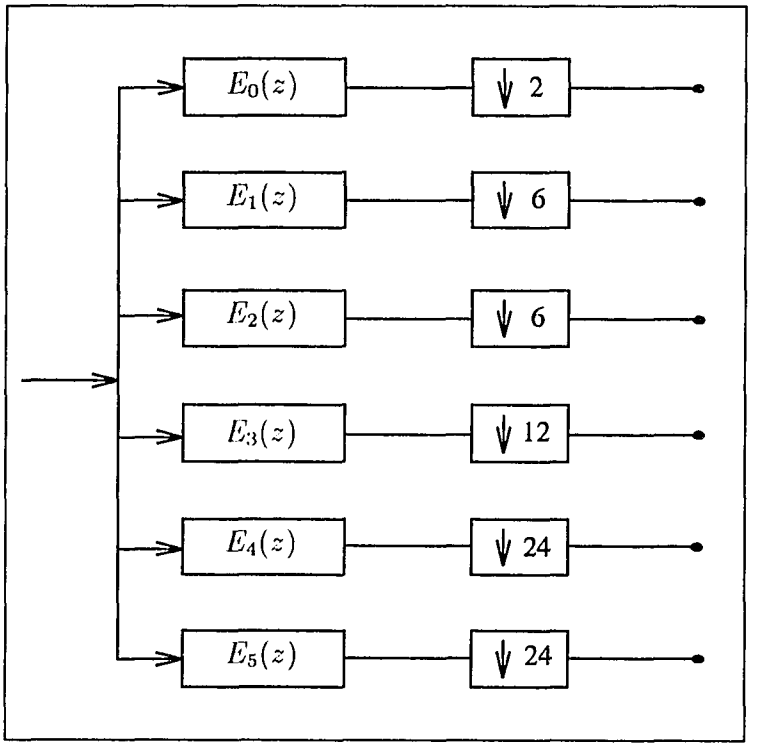

Figure 4.4 Equivalent structure for Figure 4.3.

$$E_5(z) = A_l(z)C_h(z^2)A_h(z^6)A_h(z^{12}).$$

The equivalent structure is shown in Figure 4.4. The corresponding synthesis tree and its equivalent can be easily obtained as time reversal of analysis filters. It is worthwhile to mention that the tree not only grows through one node but may also grow through different nodes. Clearly, the example tree structure is generated for a particular input signal. If the input signal varies over time, so does the tree structure. The generic adaptive tree-structuring algorithm (TSA) can be given as follows:

Begin

initialize (i,j) = (0,0)

set {active nodes} = root

```
calculate m_k(i,j) for {active nodes}
while ({active nodes} ≠ NULL)
    while ([any of m_k(i,j)] ≥ Threshold )
    for all active nodes at i^th stage
        choose the largest m_k(i,j) for i^th stage, j^th point active node.
        proceed with M-band subband decomposition (M children nodes are
        born).
        remove (i,j) from {active nodes} and label it as parent node.
        for all children nodes of parent node (i,j)
            calculate m_k(i',j') for children nodes
            if ([any of m_k(i',j')] ≥ Threshold) then
                add (i',j') to {active nodes}
            else
                label (i',j') as idle
            end
        end
    end
end
```

The TSA starts from the root and proceeds towards the leaves of the tree while checking the node metrics. The adaptive process can utilize any M-band prototype filter bank. The node metrics are calculated in all active nodes and in their children nodes. These metrics are evaluated as to whether the node becomes idle for further splitting or active for expansion. In case of activity, the current node becomes

the parent node in the following step. If all active nodes become idle, then tree-structuring is terminated and the corresponding product filters are generated.

4.3 Energy Compaction-Based Tree-Structuring

An adaptive tree structuring algorithm, by utilizing an energy compaction measure as a node metric, can effectively track the variations of frequency-localized input signals. The concept of tree structuring based on the energy compaction measure was first mentioned in [Akansu and Liu]. Thus, the energy compaction measure quantifies the unevenness of the given signal spectrum. The TSA analyzes the energy distribution of the subband spectrum at each node of the tree with the assumption of ideal filters used. A subband node is further decomposed if and only if the energy compaction at this node exceeds a predefined threshold.

Now, we will present a simple example for energy compaction-based TSA utilizing two-band and three-band prototype PR-QMFs. The TSA simultaneously considers two-band and three-band PR-QMFs in order to handle transition frequencies such as $\frac{\pi}{3}$, $\frac{\pi}{2}$, or $\frac{2\pi}{3}$. The input signal or any subband in the tree is decomposed into its sub-projections employing two- or three-band orthogonal subspaces if the decomposition criterion is met. Figure 4.5 displays a special case of TSA for narrowband signal identification [50]. In this example, only one active node is searched at a particular stage. The TSA, however, evaluates every possible node in the tree for general case.

In the most general case, the different nodes of the tree in a particular stage are independent from each other. This advantage can be used especially for parallel growing the tree. Since each path starting from the root node employs PR-QMFs, the nested paths of the overall subband tree will also be PR. This natural conclusion implies practically implementable tree structuring algorithms by parallel structuring.

The flowchart shown in Figure 4.5 can be outlined as follows:

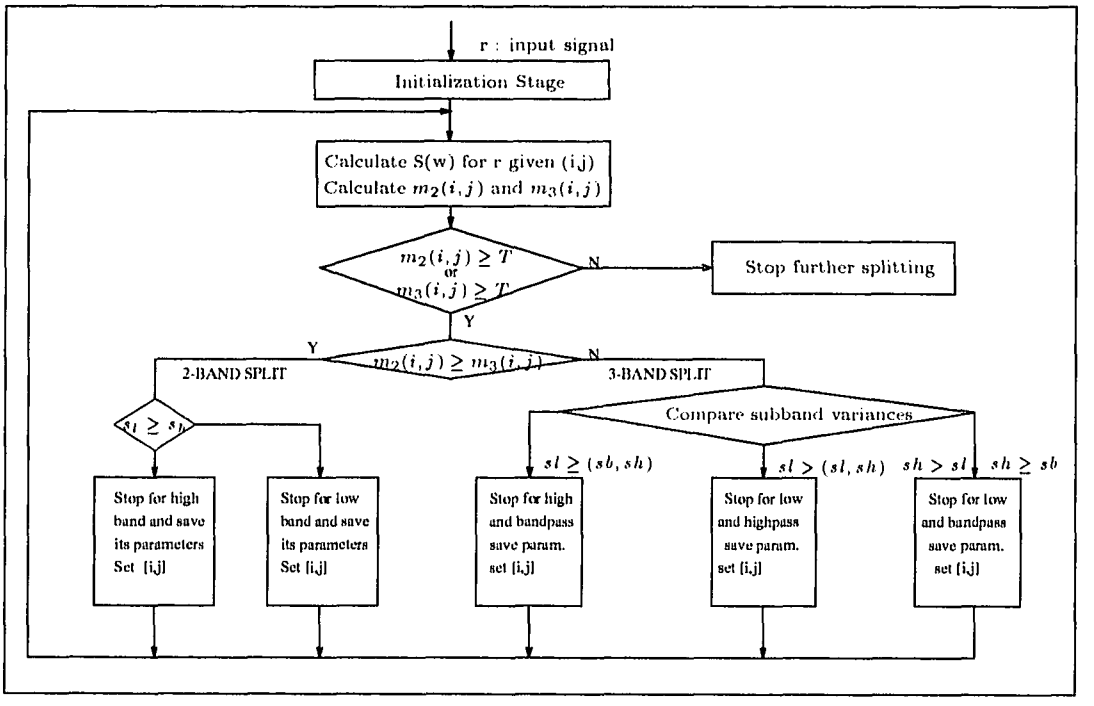

Figure 4.5 A simple example for the energy compaction-based TSA algorithm.

Begin

Initialize {(i,j) = root}

while {all nodes are not idle → (spectral flatness does not exist)}

- Measure the power spectral density, $P_{xx}(\omega)$, of the received signal.
- Calculate subband variances σ_{2l}^2 and σ_{2h}^2 for the two-band split assuming ideal brick-wall filters.
- Calculate $m_2(i,j)$.
- Calculate subband variances σ_{3l}^2, σ_{3b}^2 and σ_{3h}^2 for the three-band split.
- Calculate $m_3(i,j)$.

  If $m_2(i,j) \leq T$ and $\leq T$, then

  spectral evenness exists. Stop tree structuring,

else if $m_2(i,j) \geq m_3(i,j)$ then

proceed with the two-band split

else

proceed with the three-band split

end

Check the subband variances.

Set (i,j).

end

end

4.4 Adaptation of the Tree Structure and Its Significance

In order to expand the branches in the tree, it is essential to calculate the node metrics in each active node. Usually, the node metrics are compared to heuristic thresholds. The different applications require different thresholds (maybe different metrics as well) and unfortunately, there are not any closed-from solutions for the general case. Hence, if the metric is chosen as energy compaction then energy-localization or spectral evenness may fall under this category. This is because the energy compaction measure indirectly considers those situations. If a flat input spectrum is considered, then any M-band subband decomposition will yield

$$m_k(0,0) \;=\; 1, \quad \forall k \tag{4.5}$$

which is a lower bound for the energy compaction measure-based metric. On the other hand, if an uneven spectrum is considered, we usually have $m_k(.,.) >> 1$ for some k. Therefore, the adaptation of the tree is tightly related to node metrics and thresholds. The following example considers a composite signal of white Gaussian noise and a sinusoidal signal as

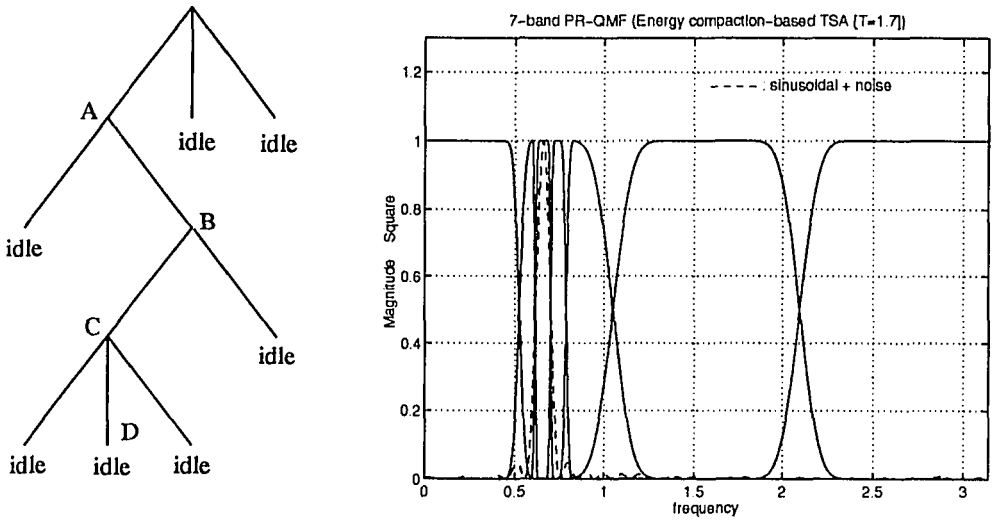

(a) (b)

Figure 4.6 Adaptively generated seven-band irregular tree structure for $threshold = 1.7$, (a) tree diagram, (b) magnitude square functions of analysis filters and input signal (sinusoidal + noise).

$$s(k) = Asin(\omega k) + n_w(k),$$

where $\omega = \frac{5\pi}{24}$ and SNR is $20dB$. Here, the objective is to localize the sinusoidal signal in a minimum bandwidth subband. The frequency of sinusoidal signal is chosen such that only two-band or three-band PR-QMFs are inadequate but both prototypes must be utilized. The energy compaction measure is used as the node metric in this example. The heuristic threshold is chosen as $T = 1.7$. In this case, TSA generates the tree structure displayed in Figure 4.6(a). If FIR prototype filters are used, then the normalized magnitude square functions of seven-band PR-QMF analysis filters are shown in Figure 4.6(b), along with signal (sinusoidal + noise). Figures 4.7, 4.8, 4.9, and 4.10 display the normalized magnitude functions of subband signals at points A, B, C, and D respectively. The TSA stops at the fourth stage and the sinusoidal signal is localized at point D, as shown in Figures 4.6(b) and 4.10. Although the main peak is successfully captured, there is some obvious spill-over from point D

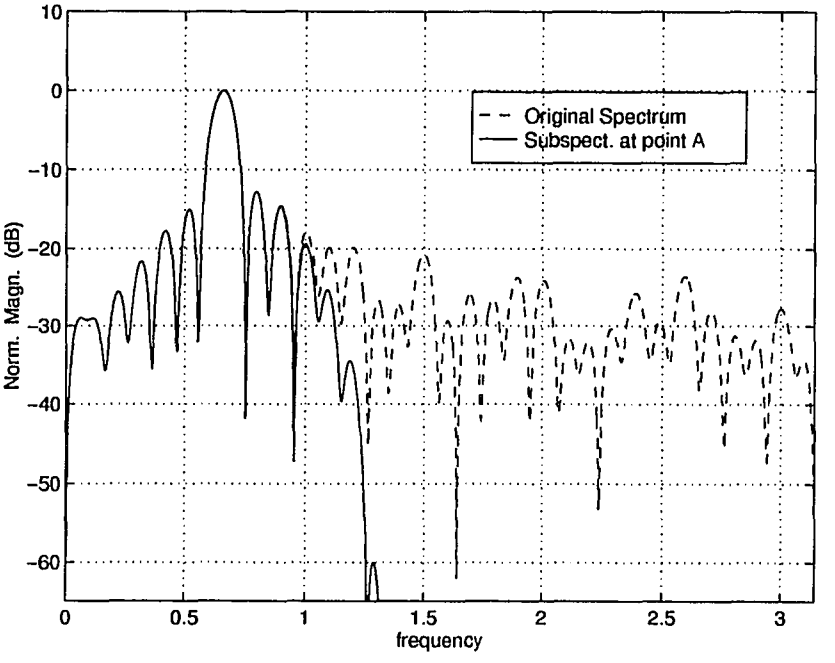

Figure 4.7 Subspectra at point A.

to adjacent subbands. If the threshold is chosen as $T = 2.5$, however, then we will have a different tree structure, shown in Figure 4.11. In this case, TSA stops after five-band decomposition, because any further decomposition is not justified. In other words, node metrics at the third stage are smaller than threshold so further splitting is not performed. This structure localizes almost all the energy of the sinusoidal signal at point C, but, in fact, it also covers some unaffected spectra which we call processing distortion. The trade-off between spillover and processing distortion are fine tuning elements in different applications.

So far we have considered the energy compaction measure as a valuable node metric for adaptation of TSA. Nevertheless, there may be some other measures more usable in other applications.

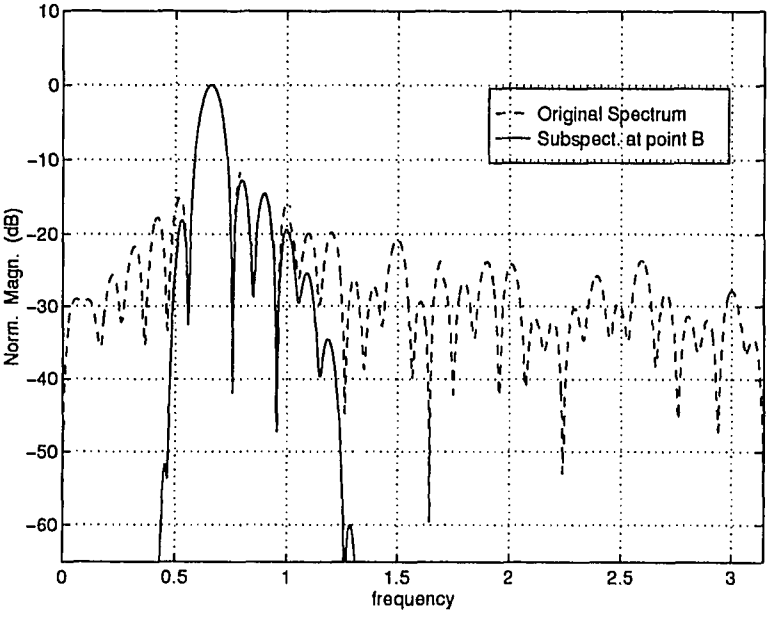

Figure 4.8 Subspectra at point B.

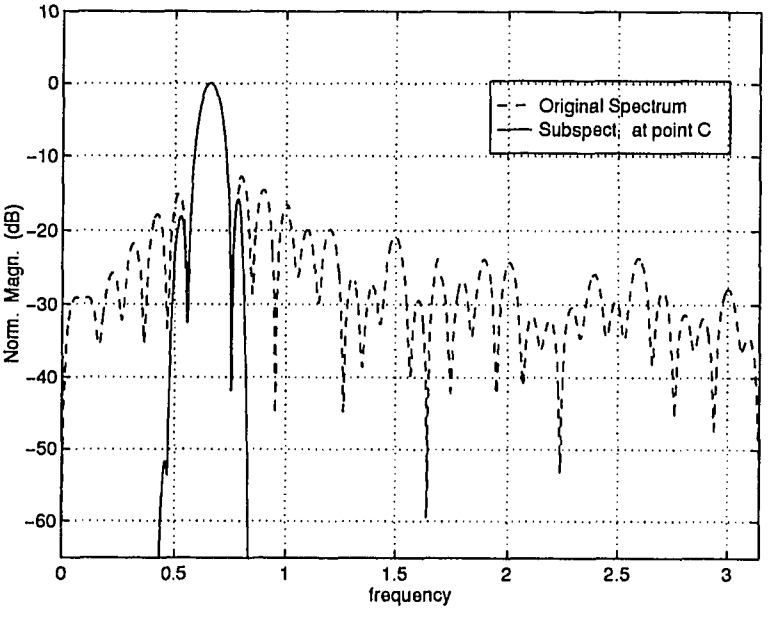

Figure 4.9 Subspectra at point C.

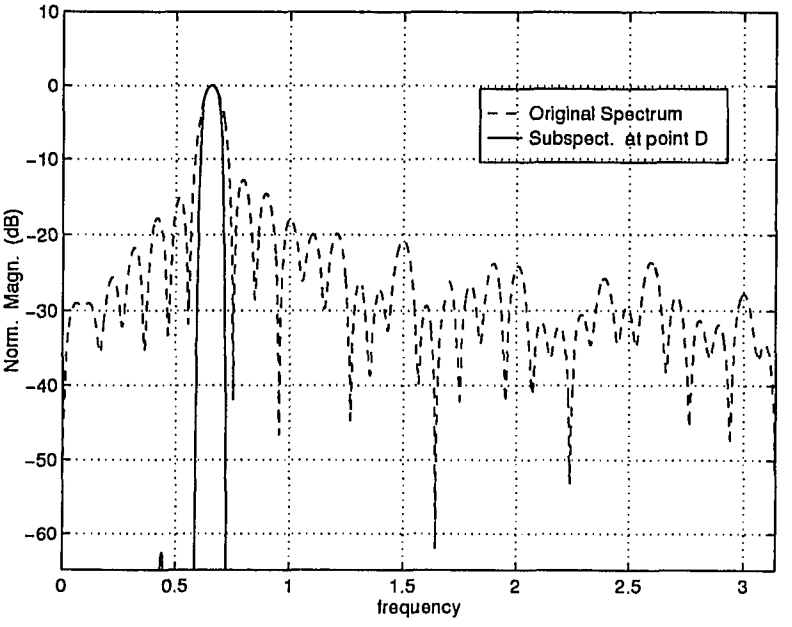

Figure 4.10 Subspectra at point D.

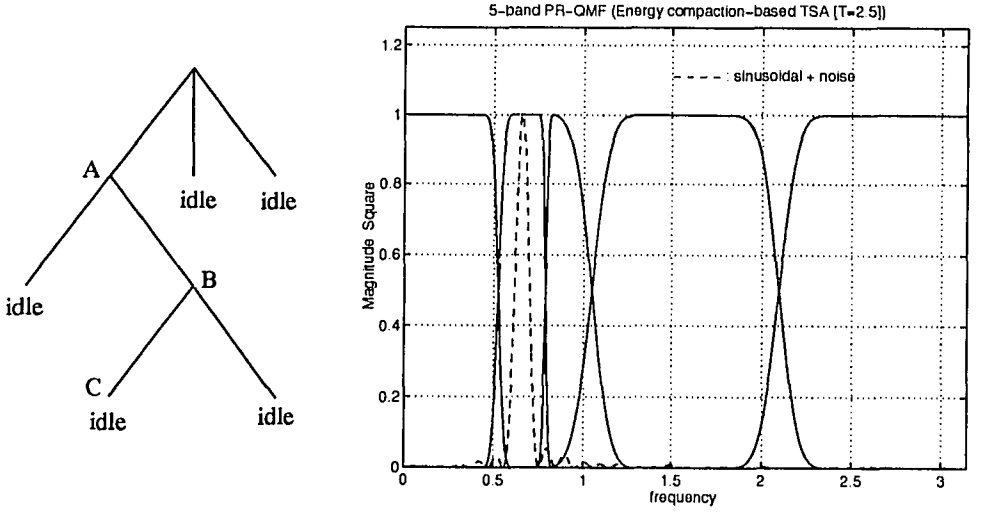

(a) (b)

Figure 4.11 Adaptively generated five-band irregular tree structure for *threshold* = 2.5, (a) tree diagram, (b) magnitude square functions of analysis filters and input signal (sinusoidal + noise).

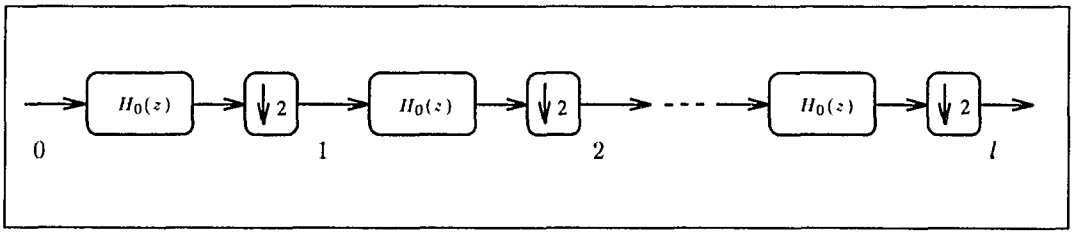

Figure 4.12 The low-pass branch of l-stage tree structure.

4.5 Transition Bandwidths

The previous section showed a discrete-time algorithm for the computation of adaptive filter banks. Indeed, a generic adaptive tree-structuring algorithm was presented. In fact, the tree growing operation (as in cascade) is much more effective using M-band schemes (three-band, four-band, ... , M-band PR-QMF solutions where M is reasonably small) instead of repeating only two-band PR-QMF solutions. As far as finite duration PR-QMF banks are concerned, the aliasing effects are eliminated as a necessary condition of PR. But in some cases, some of the subbands may be discarded, then clearly perfect alias cancellation can not be provided. Evidently, transition bandwidths or overlappings of subband filter banks become critical. Increasing duration of FIR PR-QMFs yield sharper filters with the price of increased complexity.

In tree-structuring, as we have shown, the product filters are obtained from cascaded decimation stages. Essentially, very long duration filters may yield impractically long duration filters. For example, consider an N-tap two-band PR-QMF only in the low branch of an l-stage tree-structure, shown in Figure 4.12. For simplicity, only a two-band prototype $H_0(z)$ is considered in this figure.

The equivalent l^{th} stage branch filter is given by

$$H(z) = \prod_{m=0}^{l-1} H_0(z^{2^m}), \tag{4.6}$$

and it has a total length of

$$N_t = 2^l(N-1) - (N-2). \tag{4.7}$$

Essentially, we notice that

$$N_t \simeq 2^l(N-1) \quad , \quad l >> 1. \tag{4.8}$$

Eqs.4.7 or 4.8 demonstrates the high complexity if one wants to use long duration prototype FIR PR-QMFs repetitively. The energy spillover or overlappings, however, can be overcome by using a very sharp filter in the first couple of stages and then using short duration filters afterwards. Thus, we obtain good transition bandwidths in the first stages but may yield relatively worse stop-band attenuations in the product filters. This, though, is a viable approach if aliasing is critical in the first stages of the tree.

4.6 A Flexible Tiling of the Time-Frequency Plane

The time and frequency properties of discrete-time signals can be jointly explored with the aid of time-frequency (TF) representations. In these representations, the signal is projected on a plane with respect to bases that are functions of both frequency and time. The resulting plots are called TF diagrams.

The TF representation of signals using a short-time Fourier transform (STFT) and the construction of spectrograms has been widely used in speech applications [26]. The time properties may be more visible for certain signals, but, on the contrary, frequency properties may be dominant for some other signals. The joint TF representations take advantage of both domain-properties.

Figure 4.13 shows various orthonormal bases in 64-dimensional transform space. The vertical axis represents discrete-frequency and the horizontal axis represents discrete-time. Now, consider an arbitrary segment of N samples from an arbitrary

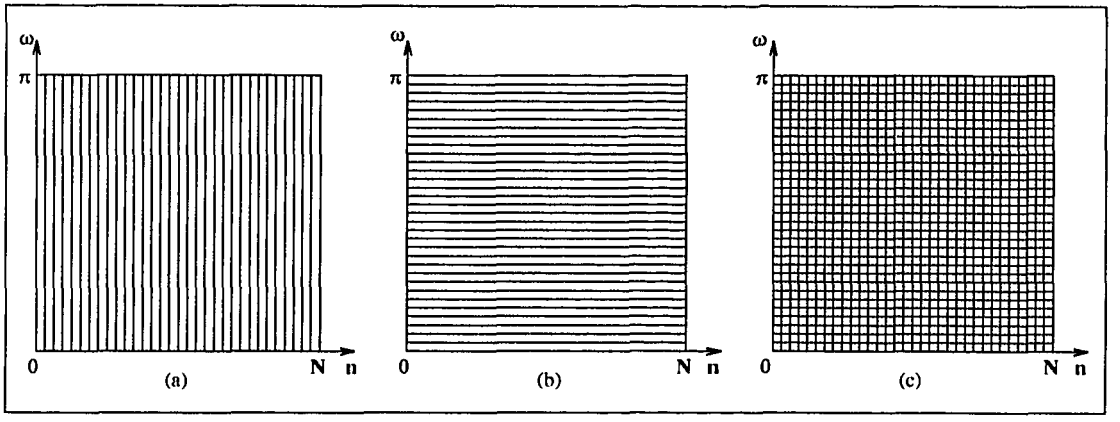

Figure 4.13 The TF diagrams of an arbitrary segment of infinite duration signal x(n), (a) without any transformation, (b) with fixed NxN block transform such as DFT or DCT, and (c) with NxN ideal spectrogram.

signal $x(n)$. We can represent this segment ($\underline{X}_N$) on the TF plane without any transformation, as shown in Figure 4.13(a). Such a representation does not provide any frequency information, but it has a perfect time representation. On the other hand, the block transforms, such as DFT or DCT, provide frequency-domain representation without time information (Figure 4.13(b)). Assuming an ideal NxN partition of the TF plane, we obtain N^2 TF cells on the diagram (Figure 4.13(c)). Such a partitioning is a sensible choice when time and frequency resolutions are equally important. This, however, is not always the case. As we emphasized in Chapter 3, different sets of linear basis functions have different time-frequency properties, so they correspond to different tilings of the time-frequency plane.

In general, arbitrary tiling of the time-frequency plane is possible with unequal bandwidth (with different time duration) transforms such as a tree-structured filter bank system. For example, Figures 4.14 and 4.15 show examples of a three-stage dyadic tree and irregular tree by their tree diagrams and TF diagrams respectively.

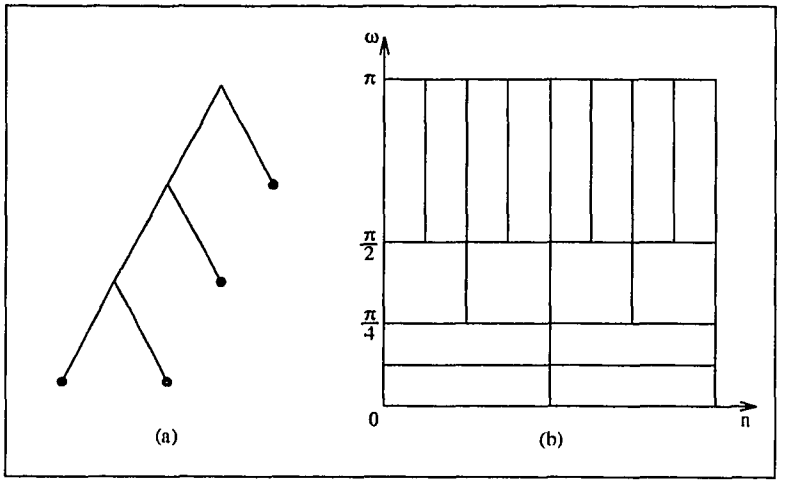

Figure 4.14 Three stage dyadic subband tree-structured filter bank (a) tree diagram, (b) TF diagram for (a).

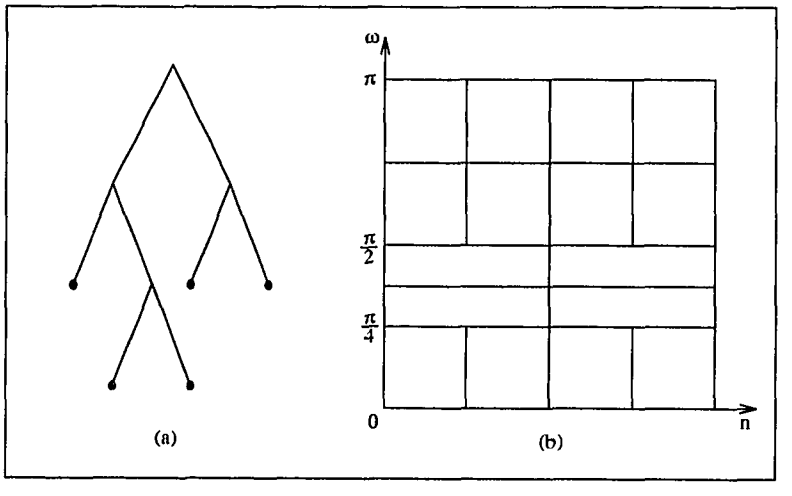

Figure 4.15 Three stage irregular subband tree-structured filter bank (a) tree diagram, (b) TF diagram for (a).

It should be noted that the localization of the energy of a basis function to the area covered by one of the tiles is only approximate. In reality, there is a considerable amount of overlapping energy in between the basis functions. Furthermore, the tiles are shaded based on the energy level of subband components of an input signal. The concept of adaptive subband tree structuring or flexible time-frequency tiling is to split whichever nodes of the subband tree make sense for the given input signal. Essentially, this approach offers more flexibility over fixed transforms.

CHAPTER 5

INTERFERENCE EXCISION IN DSSS COMMUNICATIONS SYSTEMS

Spread spectrum techniques have been successfully employed in many communication scenarios. These techniques bring desired features, such as code division multiple-access, protection against jamming, low probability of intercept, and interference rejection, to communication systems. Among different spreading techniques, the direct sequence spread spectrum (DSSS) or pseudo-noise (PN) modulation system is considered in this study. DSSS modulation techniques produce a transmitted frequency spectrum that is much wider than the information bandwidth. The spreading is done by translating the data bits to a wide bandwidth spreading sequence. This spreading sequence is generated by linear feedback shift registers and is called a pseudonoise (PN) sequence [15][58][40]. This sequence is known by the transmitter and the friendly receiver. An increase in the length of the spreading sequence implies an increase in the bandwidth of the transmitted signal. In practice, transmission bandwidth and system complexity limit the length of the PN code. The increase in bandwidth provides interference suppression, code-division multiple-access, energy density reduction, and good time resolution in digital communications systems [36].

The interference rejection capability of DSSS systems is, however, limited. Both deliberate and unintentional narrowband interference (jamming) can be rejected up to a certain jamming margin. It has been shown that the interference immunity of a DSSS receiver can be further improved by suppressing or excising the interference before the demodulation operation [24][28][25][18].

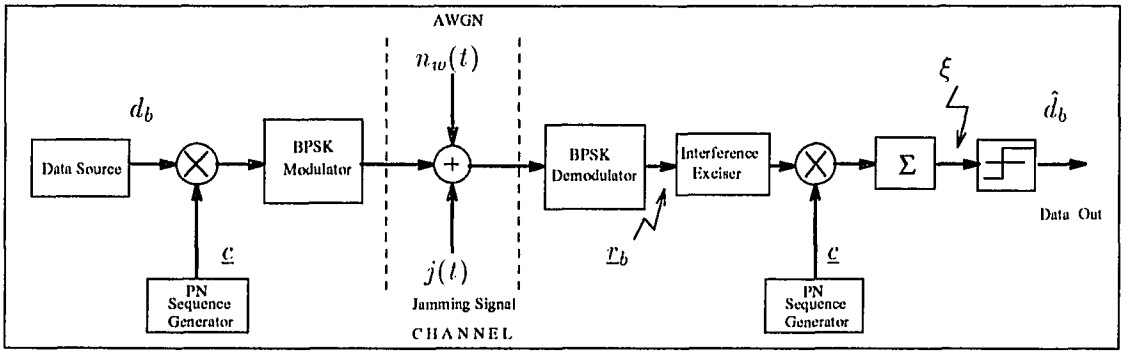

Figure 5.1 Block diagram of a DSSS communication system.

5.1 Interference Exciser-Based DSSS System Model

The DSSS transmitter, shown in Figure 5.1, spreads the incoming data bit stream d_b ($d_b \in \{-1, 1\}$, $\forall b$) and, therefore, its spectrum by multiplying it with the spreading sequence $\underline{c}$ ($c_i \in \{-1, 1\}$, for $i = 1, ..K$). The information-bearing signal is corrupted by additive white Gaussian noise (AWGN) $\underline{n}_b$ and an intentional interference or a jamming signal $\underline{j}_b$ in the communication channel. Therefore, the received signal $\underline{r}_b$ (a row vector) can be written as

$$\underline{r}_b = \sqrt{P} d_b \underline{c} + \underline{j}_b + \underline{n}_b \tag{5.1}$$

where d_b is the information bit (equiprobable ∓ 1), and $\sqrt{P}$ is the signal power at the receiver input. The data bit stream d_b has a bit-to-bit duration of T_d seconds. The PN spreading code has a chipping rate of T_c seconds, where $T_d \gg T_c$. Hence, the length of the PN code can be obtained as $L = \frac{T_d}{T_c}$. Without any interfering signal $\underline{j}_b$, the transmitted DSSS signal has a flat spectrum. The receiver correlates the signal with a properly synchronized version of the spreading sequence $\underline{c}$. The length-K PN spreading code has the energy, $\underline{c}\,\underline{c}' = \sum_{i=1}^{L} c^2(i) = L$ where $\underline{c}'$ is the transpose of the code vector $\underline{c}$. The decision variable is, therefore, obtained as

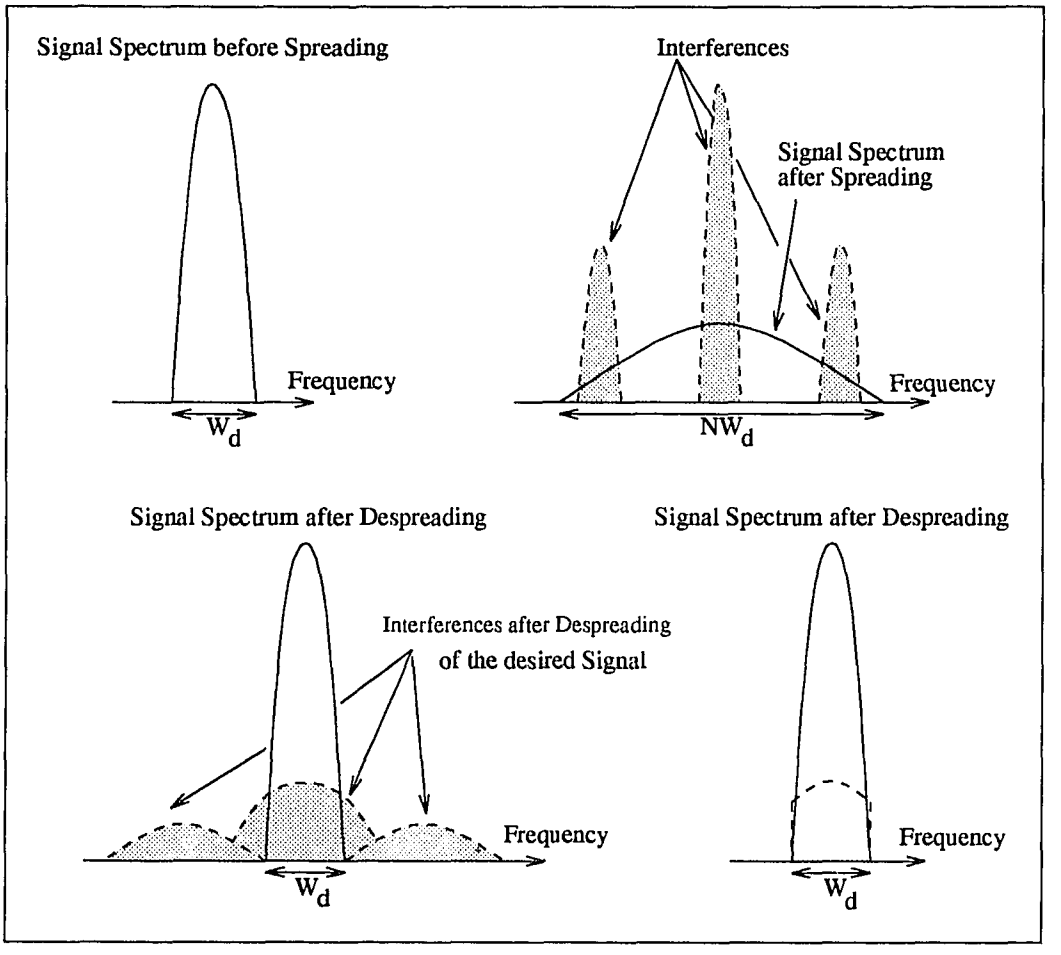

Figure 5.2 The principal steps in DSSS coders/decoders

$$\begin{aligned} U_l &= \underline{r}_b \underline{c}' = d_b \underline{c} \underline{c}' + \underline{j}_b \underline{c}' + \underline{n}_b \underline{c}' \\ &= L d_b + \underline{j}_b \underline{c}' + \underline{n}_b \underline{c}'. \end{aligned} \tag{5.2}$$

Eq.5.2 indicates that the despreading operation recovers the desired signal while spreading the interference, as shown in Figure 5.2. The bandwidth expansion in a DSSS system is translated into a processing gain as a power improvement factor

caused by signal mapping or spreading and, it can be expressed as [15]

$$G_p \triangleq 10 \log (\frac{T_d}{T_c}). \tag{5.3}$$

In a jamming environment, it is usual to define a jamming margin, which determines the performance limitation of a DSSS system [15][36]. In decibels, it is given by

$$M_{jamming} = G_p - [(\frac{S}{N})_{min} + L_{sys}], \tag{5.4}$$

where $(\frac{S}{N})_{min}$ is the minimum acceptable receiver output SNR and L_{sys} is considerable system loss. An intentional interference above the jamming margin significantly degrades the system performance if any excision technique is not used prior to the PN correlator. In fact, if the interference power is much greater than the system's jamming margin, the DSSS receiver fails to operate.

5.2 Narrowband Interference Excision Problem in DSSS Communications

The performance of a DSSS receiver in the presence of frequency-localized interference can be improved by using various types of interference rejection schemes [24][33][32][28]. In this section, two different classes are considered. The first is based on parametric linear prediction using minimum mean square error criteria and the second one is based on non-parametric transform domain processing.

The first class is the parametric modeling and estimation of the interference by means of a linear prediction filter [24][28]. Such a filter forms a linear prediction of the received signal based on previous samples. Since the DSSS signal and white Gaussian process have a flat spectra, they cannot be predicted accurately from their past values. The interfering signal, being narrowband, however, can be predicted accurately. The stationarity and narrow-bandwidth assumptions of the interference are crucial to the performance of this parametric excision technique. Otherwise, the

performance will degrade significantly [29].

An entirely different approach to the excision problem is transform-domain processing [33][32]. The discrete Fourier transform (DFT) has been the most popular transform-domain method used for narrowband interference excision [12][39][14]. The DFT, however, suffers from its fixed frequency resolution and poor side-lobe attenuation. More recently, subband transforms were proposed with improved frequency localization and side-lobe attenuation [27][30]. The optimal Karhunen-Loeve transform (KLT) is optimal in the class of block transforms. Adaptive subband transforms were also used in an adaptive time-frequency (ATF) exciser with excellent frequency localization and very robust performance [49].

The performance of different excision techniques has been examined by analytical evaluations and computer simulations. The probability of error is the performance measure considered in this study.

5.3 Linear Predictive Filtering-Based Excision

The received signal is assumed as the output of an all-pole filter driven by a white noise process in this excision technique. Linear prediction is used to estimate the coefficients of the all-pole source model. The estimated model coefficients specify an appropriate noise whitening filter which is of an all-zero type. The received signal is passed through this all-zero transversal filter in order to suppress the undesired narrow-band interference.

Considering the received signal in Eq.(5.1), the narrowband interference $j(k)$ can be predicted by a linear predictor using N previous samples of $r(k)$ as

$$\hat{j}(k) = \sum_{m=1}^{N} b_m r(k-m), \tag{5.5}$$

where $\{b_m\}$ are the linear prediction coefficients. The narrowband interference $\{j(k)\}$ can be predicted by minimizing the mean square error between $r(k)$ and $\hat{j}(k)$ as

$$\begin{aligned}\mathcal{E}(N) &= E[|e_N(k)|^2] = E[|r(k) - \hat{j}(k)|^2] \\ &= E[|r(k) - \sum_{m=1}^{N} b_m r(k-m)|^2]. \end{aligned} \tag{5.6}$$

The resulting prediction error signal

$$e_N(k) = \sum_{m=1}^{N} h_m r(k-m) \tag{5.7}$$

approximates a white noise process. The coefficients of the prediction error filter (LPEF), Figure 5.3, are related to the prediction coefficients as

$$h_0 = 1\,,\ h_m = -b_m\,,\ m = 1,2,..,N.$$

The minimization of Eq.(5.6) with respect to prediction error filter coefficients yields Yule-Walker equations, which can be solved efficiently by using the Levinson-Durbin algorithm [21]. The linear-prediction-based interference exciser output in Figure 5.3 can be written as

$$e_N(k) = \sum_{m=0}^{M-1} h(m) r(k-m), \tag{5.8}$$

where $M = N + 1$ is the length of the excision filter (Figure 5.3). Eq.(5.8) can be written as

$$\begin{aligned} e_N(k) &= \sum_{m=0}^{M-1} h(m)[c(k-m) + j(k-m) + n(k-m)] \\ &= \sum_{m=0}^{M-1} h(m)c(k-m) + \sum_{m=0}^{M-1} h(m)j(k-m) + \sum_{m=0}^{M-1} h(m)n(k-m) \\ &= c_o(k) + i_o(k) + n_o(k). \end{aligned} \tag{5.9}$$

The excised signal $\{e_N(k)\}$ is then fed to the PN correlator and yields the decision variable ξ at the output of the summer as

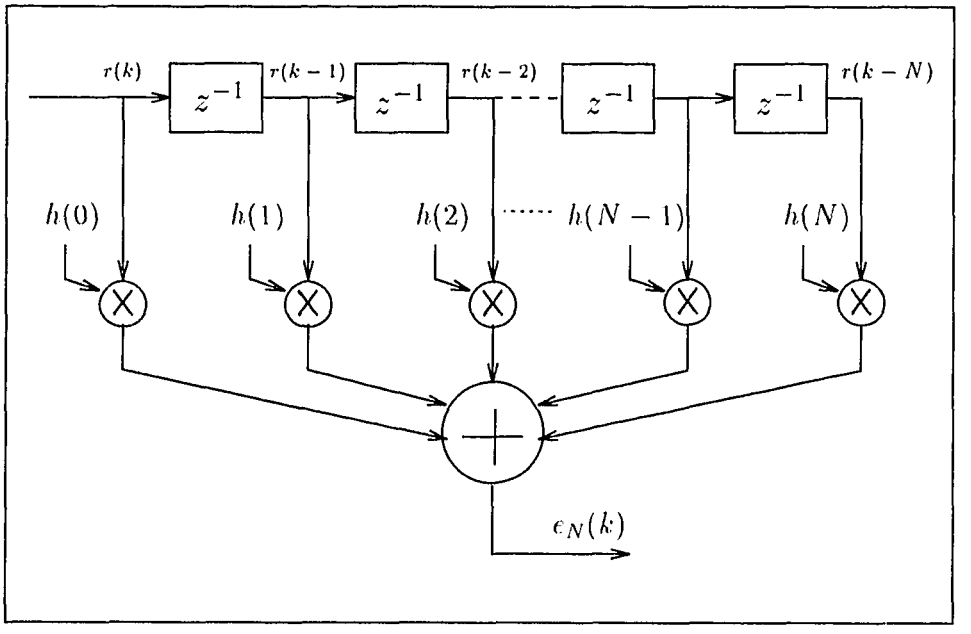

Figure 5.3 Transversal linear prediction filter.

$$\begin{aligned}\xi &= \sum_{k=1}^{L} e_N(k)c(k) = \sum_{k=1}^{L}[c_o(k) + i_o(k) + n_o(k)]c(k) \\ &= \sum_{k=1}^{L} c_o(k)c(k) + \sum_{k=1}^{L} i_o(k)c(k) + \sum_{k=1}^{L} n_o(k)c(k) \\ &= \xi_1 + \xi_2 + \xi_3. \end{aligned} \tag{5.10}$$

The PN sequence is a pseudo-random signal known by both the transmitter and the receiver. The interference $\{j(k)\}$ is assumed to be a wide-sense stationary stochastic process with a zero mean and covariance sequence $\{R_j\}$. The channel noise $\{n(k)\}$ is assumed to be a wide-sense, stationary, white Gaussian process with a zero mean and covariance sequence $\{R_n\}$. It is assumed that all three random variables $\{\xi_1, \xi_2, \xi_3\}$ in Eq.(5.10) are independent and uncorrelated.

5.3.1 Performance Analysis of a Linear Prediction Exciser-Based DSSS Receiver

The signal-to-noise-and-interference power ratio (SNIR) at the output of the summer in Fig. 5.3 is a theoretically tractable performance measure for the narrowband interference exciser case [24]. The total power of the decision variable can be written as

$$E[\xi^2] = E^2[\xi] + var[\xi], \tag{5.11}$$

where $var[\xi]$ is the variance of the decision variable. It is shown that the mean value of the decision variable, thus, corresponds to the desired signal term. The total variance of the decision variable is the sum of the variances due to the thermal noise, the remaining interference, and self-noise created by the excised PN code. The SNIR is calculated only for one bit period. The SNIR at the input of the slicer is defined as [24]

$$(SNIR)_o \triangleq \frac{E^2[\xi]}{var[\xi]}. \tag{5.12}$$

The mean value of the decision variable ξ is derived as (see Appendix B)

$$\begin{aligned} E[\xi] &= E[\xi_1 + \xi_2 + \xi_3] = E[\xi_1] + E[\xi_2] + E[\xi_3] \\ &= h(0)L - \sum_{m=1}^{M-1} h(m). \end{aligned} \tag{5.13}$$

Since $\{c(k)\}$, $\{j(k)\}$, and $\{n(k)\}$ are assumed to be uncorrelated processes, the variance of the decision variable is found as (see Appendix B):

$$\begin{aligned} var[\xi] &= var[\xi_1 + \xi_2 + \xi_3] = var[\xi_1] + var[\xi_2] + var[\xi_3] \\ &= L\sum_{m=1}^{M-1} h^2(m) + L\sum_{m=0}^{M-1}\sum_{p=0}^{M-1} h(m)h(p)\{R_j(p-m) + \sigma_n^2\delta(p-m)\} \\ &\quad -\frac{1}{L}\sum_{k=1}^{L}\sum_{\substack{l=1 \\ (l\neq k)}}^{L}\sum_{m=0}^{M-1}\sum_{p=0}^{M-1} h(m)h(p)\{R_j(k-m-l+p) + \sigma_n^2\delta(k-m-l+p)\} \end{aligned} \tag{5.14}$$

where σ_n^2 is the variance of white Gaussian noise.

Since $E[\xi]$ and $var[\xi]$ have been determined, the $SNIR_o$ at the output of the summer can be calculated from Eq.(5.12) as

$$SNIR_o = \frac{[h(0)L - \sum_{m=1}^{M-1} h(m)]^2}{L\sum_{m=1}^{M-1} h^2(m) + L\sum_{m=0}^{M-1}\sum_{p=0}^{M-1} h(m)h(p)\{R_j(p-m) + \sigma_n^2\delta(p-m)\}} \cdots$$
$$\cdots \frac{1}{-\frac{1}{L}\sum_{k=1}^{L}\sum_{\substack{l=1 \\ (l\neq k)}}^{L}\sum_{m=0}^{M-1}\sum_{p=0}^{M-1} h(m)h(p)\{R_j(k-m-l+p) + \sigma_n^2\delta(k-m-l+p)\}}. \tag{5.15}$$

Finally, the bit error rate (BER) performance of the linear prediction exciser based DSSS receiver is expressed as [28][25]

$$P_e = Q\left(\sqrt{SNIR_o}\right) = Q\left(\sqrt{\frac{E^2[\xi]}{var[\xi]}}\right) \tag{5.16}$$

where

$$Q(x) \triangleq \frac{1}{\sqrt{2\pi}}\int_x^\infty e^{-y^2/2}dy. \tag{5.17}$$

This analytical BER calculation will be compared with the experimental performance results of linear prediction exciser based DSSS receiver in Sec. 5.7.

5.3.2 SNIR Improvement of an Exciser-based DSSS Receiver

The theoretical SNIR improvement of a DSSS receiver resulting from the use of an interference exciser can be quantified by comparing the SNIRs with and without an exciser cases [24]. We denote signal-to-noise-and-interference ratio without the interference excision as $SNIR_{wo}$. In this case, the mean value and the variance of the decision variable ξ' are found as (assuming that $d_b = +1$)

$$E[\xi'] = L, \tag{5.18}$$
$$var[\xi'] = L\{\sigma_j^2 + \sigma_n^2\} - \frac{1}{L}\sum_{k=1}^{L}\sum_{\substack{l=1 \\ (l\neq k)}}^{L}\{R_j(k-l) + \sigma_n^2\delta(k-l)\},$$

$$= L\{\sigma_j^2 + \sigma_n^2\} - \frac{1}{L}\sum_{k=1}^{L}\sum_{\substack{l=1 \\ (l\neq k)}}^{L} R_j(k-l). \tag{5.19}$$

Therefore,

$$SNIR_{wo} = \frac{E^2[\xi']}{var[\xi']} = \frac{L^2}{L\{\sigma_j^2 + \sigma_n^2\} - \frac{1}{L}\sum_{k=1}^{L}\sum_{\substack{l=1 \\ (l\neq k)}}^{L} R_j(k-l)}. \tag{5.20}$$

As a result, the $SNIR$ improvement factor S_I, from Eqs.(5.15) and (5.20), is expressed as

$$S_I = \frac{SNIR_o}{SNIR_{wo}}. \tag{5.21}$$

5.4 Transform Domain-Based Excision

In the transform-domain excision, the frequency spectrum of the received signal is examined, and the narrowband interference is located. Then, the undesired spectral components of the received signal are excised prior to the correlator. The frequency spectrum of the received signal might be assessed by using different transform techniques. MxM block transform and M-band filter bank are widely used decomposition tools to map the received signal to the spectral domain (forward transform or analysis). The excision operation is a spectral modification of the received signal such that some of the transform coefficients are nulled in order to excise the narrowband interference. Then, the inverse transform (synthesis) is performed on the excised coefficient vector. The resulting excised signal is the input to the correlator.

5.4.1 Fixed Transform-Based Excisers

The most common block transform, DFT, decorrelates any input signal with a circulant correlation matrix. The discrete cosine transform (DCT) approximates the optimal KLT for highly correlated signals. Considering the fact that only the

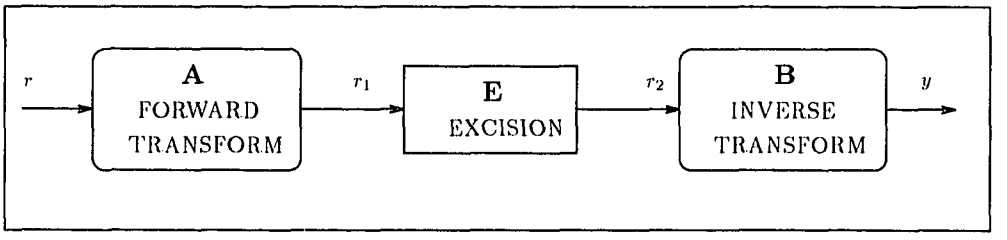

Figure 5.4 Block diagram of the transform domain-based exciser.

interference component of the received signal might have high correlation, the DFT and the DCT are expected to perform well. A generic fixed transform domain-based exciser is displayed in Fig. 5.4. In this figure, **A** is the forward transform matrix , **E** is the excision and **B** is the inverse transform matrices, respectively. The excision matrix **E** is a diagonal matrix which has ones for the transform bins that are not excised and zeros for the excised transform bins. There are two linear transform families considered in this thesis..

(a) Block Transform: The excised signal based on a block transform can be written as

$$\underline{y} = \mathbf{B}\,\mathbf{E}\,\mathbf{A}\,\underline{r}, \tag{5.22}$$

where $\underline{r}$ is the received input vector.

An M-point transform matrix is utilized in the DFT and DCT exciser-based DSSS receivers. In the KLT exciser-based DSSS receiver case, the optimal basis for the given input statistics is obtained via the eigenanalysis as [26]

$$\mathbf{R}\mathbf{\Phi} = \mathbf{\Phi}\mathbf{\Lambda}, \tag{5.23}$$

where $\mathbf{R} = E[\underline{r}\underline{r}^T]$ is the input covariance matrix. The diagonal matrix $\mathbf{\Lambda}$ has the eigenvalues of $\mathbf{R}$. The matrix $\mathbf{\Phi}$ consists of the eigenvectors of $\mathbf{R}$. In this scheme, eigenfunctions with higher coefficient values contain the narrowband interference.

5.4.2 Uniform M-Band Filter Bank Case

An M-band analysis/synthesis filter bank is considered in this case, see Fig. 5.6. Each analysis filter (and synthesis filter) has approximately π/M bandwidth and N-tap duration. The synthesis filters are equivalent to the time reversals of the analysis filters [4][55]. The M-band filter banks naturally provide a better frequency resolution than the block transforms since they utilize longer duration basis functions. The following matrix notation is used for the terms in Fig. 5.6

$\underline{r}$: received signal vector $[L\text{x}1]$

$\mathbf{H}_i$: convolution matrix for the i^{th} analysis filter $[(N+L-1)\text{x}L]$.

$\mathbf{E}_i$: excision matrix for the i^{th} branch operation $[(N+L-1)\text{x}(N+L-1)]$.

$\mathbf{G}_i$: convolution matrix for the i^{th} synthesis filter $[(2\{N-1\}+L)\text{x}(N+L-1)]$.

$\mathbf{T}_i$: truncation matrix for the i^{th} subband vector $[L\text{x}(2\{N-1\}+L)]$.

$\underline{y}_i$: the i^{th} subband vector $[L\text{x}1]$.

The i^{th} subband output of Fig. 5.6 can be easily written in the matrix form as

$$\underline{y}_i = \mathbf{T}_i\, \mathbf{G}_i\, \mathbf{E}_i\, \mathbf{H}_i\, \underline{r}. \tag{5.24}$$

The excised signal is therefore obtained by the sum of all branch outputs of the filter bank as

$$\begin{aligned} \underline{y} &= \mathbf{T}_1\, \mathbf{G}_1\, \mathbf{E}_1\, \mathbf{H}_1\, \underline{r} + \mathbf{T}_2\, \mathbf{G}_2\, \mathbf{E}_2\, \mathbf{H}_2\, \underline{r} + \cdots + \mathbf{T}_M\, \mathbf{G}_M\, \mathbf{E}_M\, \mathbf{H}_M\, \underline{r} \\ &= \sum_{i=1}^{M} \mathbf{T}_i\, \mathbf{G}_i\, \mathbf{E}_i\, \mathbf{H}_i\, \underline{r} = \sum_{i=1}^{M} \mathbf{S}_i\, \underline{r}, \end{aligned} \tag{5.25}$$

where $\mathbf{S}_i \triangleq \mathbf{T}_i\, \mathbf{G}_i\, \mathbf{E}_i\, \mathbf{H}_i$. The analysis/synthesis filter bank is assumed to be of perfect reconstruction [4][55]. Therefore, whenever all $\mathbf{E}_i$ are identity matrices, no excision is performed, $\underline{y} = \underline{r}$.

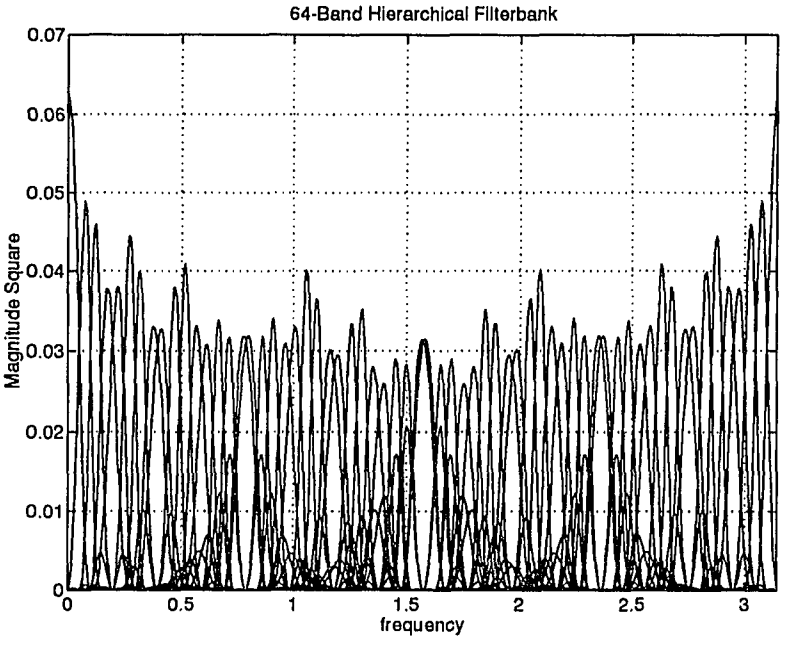

Figure 5.5 Frequency responses of progressively optimized hierarchical 64-band product filters $[0\ ,\ \pi]$.

The shortcomings of fixed block transforms and filter banks are twofold: fixed time-frequency resolution and a high-level of interband spectral leakage. A narrowband interference falling into one of the transform bins or subbands can be efficiently suppressed. The spectral variations of the interference between the transform bins (or subbands), however, cause a dynamic contamination in the desired signal (Fig. 5.5). In order to suppress this kind of jammer, more transform bins have to be removed, causing more loss of the desired signal energy [18].

5.4.3 Adaptive Subband Transform-Based Excision

An MxM block transform and an M-band filter bank achieve a fixed and uniform spectral resolution. In fixed transform-based excisers, the location of the interference spectrum and side-lobe attenuations of the basis functions are critical on the system performance. An adaptive subband transform tracks the variations of the input

spectrum and minimizes the interband spectral leakage. This naturally reduces the undesired effects of the exciser on the desired signal spectrum. Hence, it improves the system performance.

An adaptive subband transform basis can be generated by using a simple subband tree structuring algorithm (TSA), as explained in chapter 4 [5][49]. For a given input spectrum, TSA recommends the best subband tree, regular or irregular, consisting of 2-band and/or 3-band prototype filter bank cells. The TSA considers both 2-band and 3-band PR-QMFs in order to handle the frequency regions around $\frac{\pi}{3}$, $\frac{\pi}{2}$, or $\frac{2\pi}{3}$. The input spectrum or any subspectrum in the tree is hierarchically decomposed into its constituent orthogonal projections employing the generic two- or three-band subspaces. Therefore, the best subband tree for the given input spectrum is generated in order to localize the undesired interference.

The TSA algorithm analyzes the spectra at each node of the tree, with the assumption of ideal decomposition filters, and either justifies any further decomposition on the tree. For a given DSSS signal with narrowband interference, TSA hierarchically defines a subband tree with the best energy compaction and a minimum number of subbands using the given prototype 2- and 3-band basis functions. By fine partitioning of the spectrum, a superior frequency resolution is obtained. The interband spectral leakage is minimized in the range of narrowband interference by utilizing the frequency-localized filters and avoiding unnecessary splits.

5.4.4 Analysis of Adaptive Filter Bank-Based Interference Exciser

A filter bank-based exciser is displayed in Figure 5.6. $\{H_i(e^{j\omega})\}$ and $\{G_i(e^{j\omega})\}$ are the discrete-time Fourier transform of the analysis $\{h_i(n)\}$ and synthesis $\{g_i(n)\}$ filter functions, respectively. The $\{E_i\}$ coefficients represent the excision weights. If particular subbands are excised, then corresponding bins are multiplied by zero, otherwise by one. The input-output relationship of the analysis/synthesis filter bank

can easily be traced. The i^{th} branch output in Fig. 5.6 is written as

$$Y_i(e^{j\omega}) = E_i H_i(e^{j\omega}) G_i(e^{j\omega}) R(e^{j\omega}), \tag{5.26}$$

where $R(e^{j\omega})$ discrete-time Fourier transform of input signal $r(k)$. The excision coefficient E_i is defined in the frequency domain as

$$E_i = \begin{cases} 1 & , \quad 1 \leq i < i_1 \\ 0 & , \quad i_1 \leq i \leq i_p \\ 1 & , \quad i_p < i \leq i_M \end{cases} . \tag{5.27}$$

where bins $i_1 \leq i \leq i_p$ are assumed to be excised. The exciser output is therefore expressed as

$$Y(e^{j\omega}) = \sum_{i=1}^{M} Y_i(e^{j\omega}) = \sum_{i=1}^{M} E_i H_i(e^{j\omega}) G_i(e^{j\omega}) R(e^{j\omega}) \tag{5.28}$$

The equivalent filter for the i^{th} branch can be defined as

$$T_i(e^{j\omega}) \triangleq E_i H_i(e^{j\omega}) G_i(e^{j\omega}). \tag{5.29}$$

Hence, the output spectrum is expressed as

$$Y(e^{j\omega}) = \sum_{\substack{i=1 \\ \{i \neq i_1, i_2, \cdots, i_p\}}}^{M} H_i(e^{j\omega}) G_i(e^{j\omega}) R(e^{j\omega}). \tag{5.30}$$

The signal power at the output of the exciser is calculated as

$$\begin{aligned} \sigma_y^2(\Delta\omega) &= \frac{1}{2\pi} \int_{-\pi}^{\pi} |Y(e^{j\omega})|^2 d\omega \\ &= \frac{1}{2\pi} \int_{-\pi}^{\pi} |\sum_{\substack{i=1 \\ \{i \neq i_1, i_2, \cdots, i_p\}}}^{M} H_i(e^{j\omega}) G_i(e^{j\omega}) R(e^{j\omega})|^2 d\omega, \end{aligned} \tag{5.31}$$

where $\Delta\omega$ is the total excision bandwidth. It is a function of the number of excised bins or subbands $\{i_1, i_2, \cdots, i_p\}$.

A similar result can also be obtained in the time domain. The i^{th} branch output is expressed as

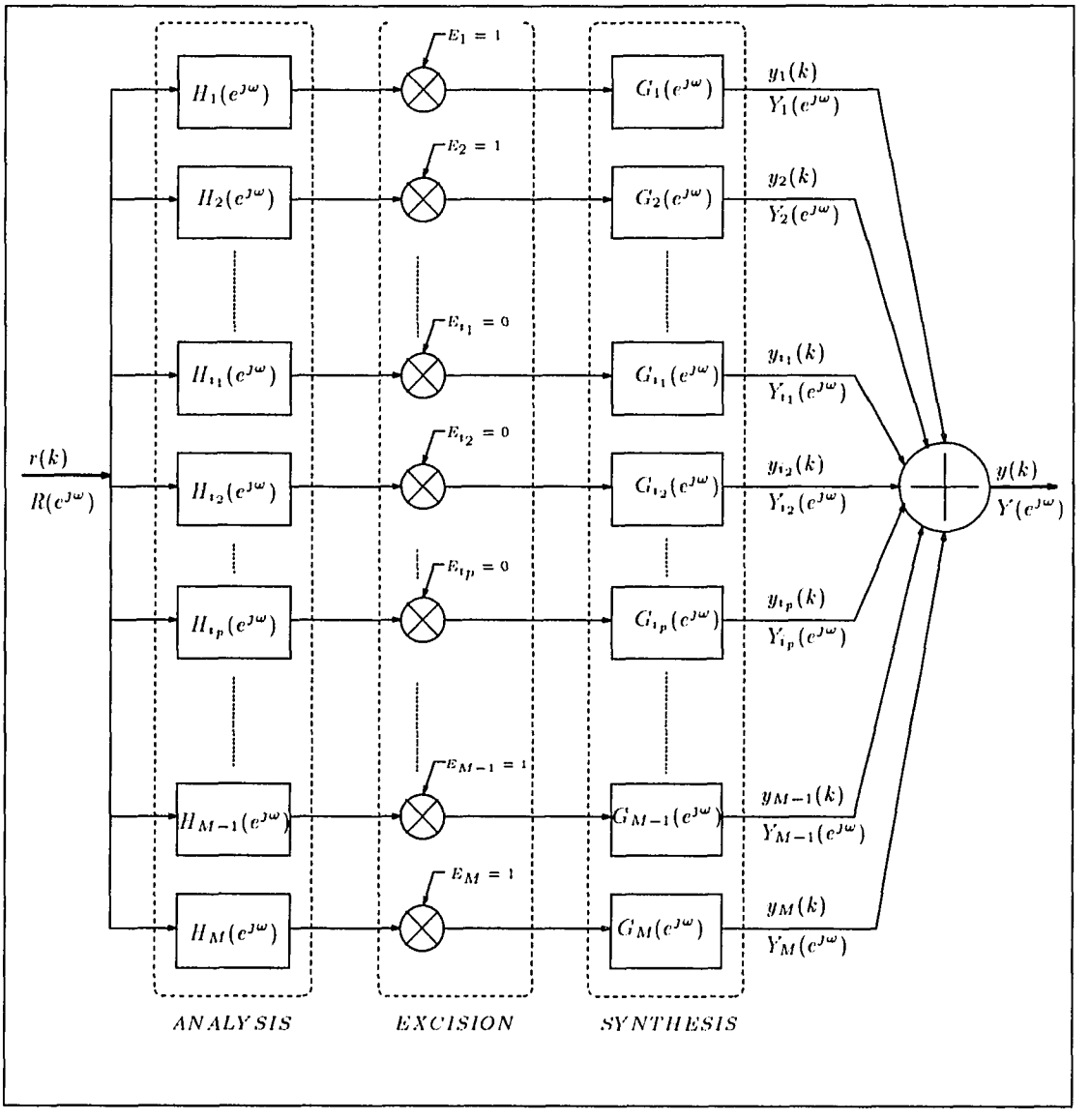

Figure 5.6 Generalized filter bank-based interference exciser.

$$\tilde{y}_i(k) = [e_i(k) * h_i(k) * g_i(k)] * r(k) \tag{5.32}$$

where $*$ represents a convolution operation. The excision weights $\{e_i(k)\}$ are similarly defined as,

$$e_i(k) = \begin{cases} \delta(k) & , \quad 1 \le i < i_1 \\ 0 & , \quad i_1 \le i \le i_p \\ \delta(k) & , \quad i_p < i \le M \end{cases} \tag{5.33}$$

The equivalent filter of the i^{th} branch is defined as

$$t_i(k) \triangleq e_i(k) * h_i(k) * g_i(k) = e_i(k) * \sum_{m=0}^{N-1} h_i(m) g_i(k-m) \tag{5.34}$$

$t_i(k)$ is a $(2N-1)$-tap linear phase FIR filter since $g_i(k)$ is the time reversed version of $h_i(k)$ [4][55]. For the excised bins

$$e_i(k) = 0 \longrightarrow t_i(k) = 0 \quad for \quad i = i_1, i_2, \cdots, i_p$$

The i^{th} branch output signal (with $e_i(k) = \delta(k)$) is

$$\begin{aligned} \tilde{y}_i(k) &= t_i(k) * r(k) = \sum_{l=0}^{2N-2} t_i(l) r(k-l) \\ &= \sum_{l=0}^{2N-2} \{ \sum_{m=0}^{N-1} h_i(m) g_i(l-m) \} r(k-l). \end{aligned} \tag{5.35}$$

With the assumption of p branches are excised in Figure 5.6, the output signal can be expressed as

$$\tilde{y}(k) = \sum_{i=1}^{M} \sum_{l=0}^{2N-2} t_i(l) r(k-l). \tag{5.36}$$

The transient effects of these FIR filtering operations should be noticed in the time domain. We assume that a $(2N-1)$-tap FIR filter generates an N-tap delay for an L-tap input. Therefore, the excised output signal vector will look like

$$\underline{\tilde{y}} = [d_1 \; d_2 \cdots d_{N-1} \; \underbrace{\tilde{y}_N \; \tilde{y}_{N+1} \cdots \tilde{y}_{N+L-1}} \; d_{N+L} \; d_{N+L+1} \cdots d_{2(N-2)+L}]^T \tag{5.37}$$

where $\{d_i\}$ are the transient. Hence,

$$\underline{y} = [\tilde{y}_N \; \tilde{y}_{N+1} \cdots \tilde{y}_{N+L-1}]^T = [y_1 \; y_2 \cdots y_L]^T$$

is the desired output vector after the delay adjustment, with respect to the input $\underline{r} = [r_1 \; r_2 \cdots r_L]^T$ and the filters used. Similar to Eq.(5.31), the excised output power can be expressed as a function of the excision bandwidth,

$$\begin{aligned} \sigma_y^2(\Delta\omega) &= \sum_{k=1}^{L} y^2(k) = \sum_{k=N}^{N+L-1} \tilde{y}^2(k) \\ &= \sum_{k=N}^{N+L-1} \{ \sum_{\substack{i=1 \\ \{i \neq i_1, i_2, \cdots, i_p\}}}^{M} \sum_{l=0}^{2N-2} \sum_{m=0}^{N-1} h_i(m) g_i(l-m) r(k-l) \}^2 \end{aligned} \tag{5.38}$$

The output signal power is related to the excision bandwidth. Therefore, Eqs.(5.31) and (5.38) are equivalent.

5.4.5 Performance Analysis of a Transform Domain Exciser-Based DSSS Receiver

We extend the performance analysis given in Sec. 5.3.1 to the case of transform domain exciser-based DSSS receiver in this section. The decision variable ξ can be written as similar to Eq.(5.10). The summation, however, runs from $(k = N)$ to $(k = N + L - 1)$ in this case as explained above,

$$\xi = \sum_{k=N}^{N+L-1} \tilde{y}(k) c(k) \tag{5.39}$$

The decision variable can be rewritten in the open-form as

$$\xi = \sum_{k=N}^{N+L-1} [\sum_{i=1}^{M} \sum_{l=0}^{2N-2} t_i(l) r(k-l)] \, c(k) \tag{5.40}$$

where $r(k)$ is the input signal as $r(k) = d_b c(k) + j(k) + n(k)$ and $t_i(l)$ was defined in Eq.5.34. Combining this into Eq.5.40, the decision variable (with the assumption of $d_b = +1$) turns out to be

$$\xi = \sum_{k=N}^{N+L-1} \sum_{i=1}^{M} \sum_{l=0}^{2N-2} \{t_i(l)[c(k-l) + j(k-l) + n(k-l)]\} c(k) \tag{5.41}$$

$$= \sum_{k=N}^{N+L-1}\sum_{i=1}^{M}\sum_{l=0}^{2N-2} t_i(l)c(k-l)c(k) + \sum_{k=N}^{N+L-1}\sum_{i=1}^{M}\sum_{l=0}^{2N-2} t_i(l)j(k-l)c(k)$$
$$+ \sum_{k=N}^{N+L-1}\sum_{i=1}^{M}\sum_{l=0}^{2N-2} t_i(l)n(k-l)c(k)$$
$$= \sum_{k=N}^{N+L-1}\sum_{i=1}^{M} t_i(0)c^2(k) + \sum_{k=N}^{N+L-1}\sum_{i=1}^{M}\sum_{l=1}^{2N-2} t_i(l)c(k-l)c(k)$$
$$+ \sum_{k=N}^{N+L-1}\sum_{i=1}^{M}\sum_{l=0}^{2N-2} t_i(l)j(k-l)c(k) + \sum_{k=N}^{N+L-1}\sum_{i=1}^{M}\sum_{l=0}^{2N-2} t_i(l)n(k-l)c(k).$$

Therefore, we can express the decision variable as

$$\xi = \xi_1 + \xi_2 + \xi_3. \tag{5.42}$$

The mean value of the decision variable ξ (for the case of transform domain-based exciser) is derived as (see Appendix B)

$$E[\xi] = L\sum_{i=1}^{M} t_i(0) - \frac{1}{L}\sum_{k=N}^{N+L-1}\sum_{i=1}^{M}\sum_{l=1}^{2N-2} t_i(l). \tag{5.43}$$

Similarly, the variance of the decision variable is expressed as

$$var[\xi] = E[(\xi_1 + \xi_2 + \xi_3)^2] - E^2[\xi].$$

Since ξ_1 , ξ_2 , ξ_3 are uncorrelated, we can rewrite the variance expression as

$$var[\xi] = var[\xi_1] + var[\xi_2] + var[\xi_3],$$

where

$$var[\xi_1] = L^2\sum_{i=1}^{M}\sum_{r=1}^{M}\sum_{l=0}^{2N-2} t_i(l)t_r(l) - [L\sum_{i=1}^{M} t_i(0) - \frac{1}{L}\sum_{k=N}^{N+L-1}\sum_{i=1}^{M}\sum_{l=1}^{2N-2} t_i(l)]^2, \tag{5.44}$$

$$var[\xi_2] = L\sum_{i=1}^{M}\sum_{r=1}^{M}\sum_{l=0}^{2N-2}\sum_{s=0}^{2N-2} t_i(l)t_r(s)R_j(s-l)$$
$$-\frac{1}{L}\sum_{k=N}^{N+L-1}\sum_{\substack{p=N \\ p\neq k}}^{N+L-1}\sum_{i=1}^{M}\sum_{r=1}^{M}\sum_{l=0}^{2N-2}\sum_{s=0}^{2N-2} t_i(l)t_r(s)R_j(k-l-p+s), \tag{5.45}$$

$$var[\xi_3] = L\sigma_n^2 \sum_{i=1}^{M}\sum_{r=1}^{M}\sum_{l=0}^{2N-2} t_i(l)t_r(l) - \frac{1}{L}\sum_{k=N}^{N+L-1}\sum_{\substack{p=N \\ p\neq k}}^{N+L-1}\sum_{i=1}^{M}\sum_{r=1}^{M}\sum_{l=0}^{2N-2}\sum_{s=0}^{2N-2} t_i(l)t_r(s)\sigma_n^2\delta(k-l-p+s). \quad (5.46)$$

The non-trivial derivation steps of these variance terms are given in Appendix B.

The $(SNIR)_o$ for the transform domain exciser case is similarly defined as Eq.(5.12). Furthermore, the BER performance of the transform domain exciser based DSSS receiver is calculated via Eq.(5.16) as defined earlier in Sec. 5.3.1. The analytical BER calculations of the transform domain exciser based receiver will be presented and compared with the experimental performance results in Sec. 5.7.

5.5 Cosine-Modulated Binomial-Gaussian Filter-Based Excision

The narrowband interference excision can be performed efficiently by using a practical frequency window. Recently, it was shown that the performance of fixed transforms are not robust against non-stationary interferers. This can be explained by their fixed spectral resolution and frequency localizations. A sliding frequency window function with an adaptive bandwidth is more proper for excision. For this purpose, a Binomial-Gaussian function is an appropriate choice because of its simplicity, smooth frequency response, and excellent frequency localization [19]. By calculating the DFT of the received signal, a smart interference localizer examines the frequency localization of the interference and its approximate bandwidth. Using this data, the Binomial-Gaussian window generator calculates the corresponding filter coefficients (Figure 5.7). Then, the prototype filter is modulated to the interference frequency. The interference is excised by filtering the signal with this linear phase FIR filter and subtracting it from its delayed version. A comparator checks whether the excision goal is achieved.

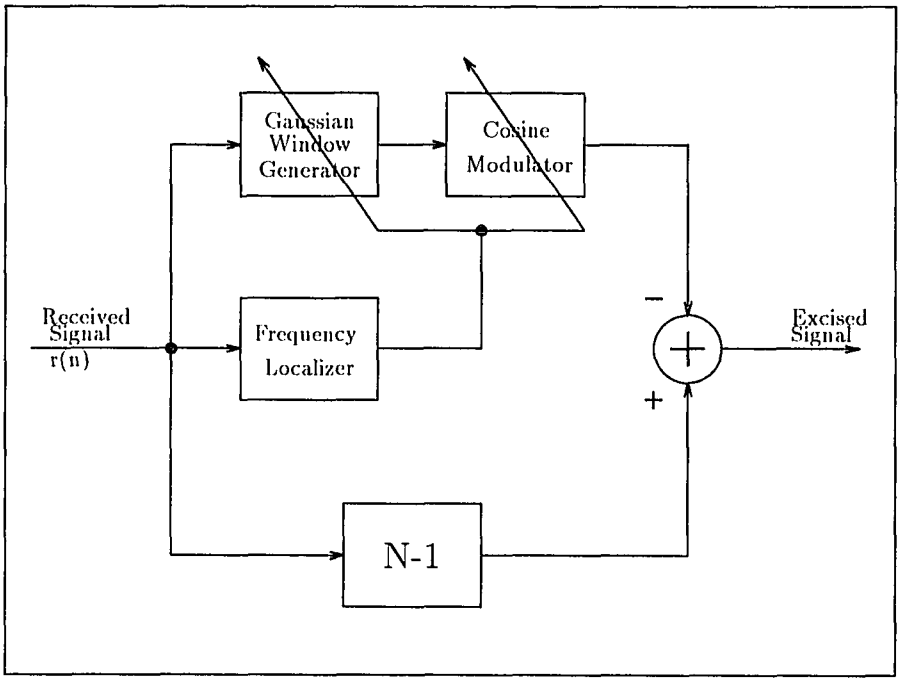

Figure 5.7 Cosine modulated adaptive Binomial-Gaussian frequency exciser.

The Gaussian approximation of the Binomial coefficients can be used to estimate the Gaussian pulse [19]. It can be written for $N \gg 1$,

$$\left(\begin{array}{c} N \\ k \end{array} \right) \sim \frac{2^N}{\sqrt{N\frac{\pi}{2}}} e^{-\left\{ \frac{(k-\frac{N}{2})^2}{\frac{N}{2}} \right\}}. \tag{5.47}$$

This Binomial sequence reassembles the Gaussian pulse successfully for large N. The factor of $(\frac{1}{2})^{N-1}$ normalizes the Binomial function's frequency response to one at $\omega = 0$. Therefore, for a practical implementation of the Binomial-Gaussian function,

$$f(k) = (\frac{1}{2})^{N-1} \left(\begin{array}{c} N \\ k \end{array} \right) \tag{5.48}$$

can be used to replace the Gaussian pulse [19]:

$$f(k) = \sigma \sqrt{\frac{A}{\pi}} e^{-\sigma^2 k^2} \tag{5.49}$$

$$|F(e^{j\omega})|^2 = A e^{-\omega^2/2\sigma^2} \qquad |\omega| < \pi, \tag{5.50}$$

where the constant A is chosen so as to normalize the energy of the function to unity over $[-\pi, \pi]$. The bandwidth of the filter (σ) is determined by the variance of the Gaussian pulse. But the bandwidth in frequency is also related to the duration in time. Therefore, a closed-form relation is necessary between the duration (N) and bandwidth of the filter, which can be approximated by $N = \frac{4}{\sigma^2}$ as shown in [19]. For practical purposes, it is advisable to restrict the length of the filter to $N = 512$ taps. The modulation of the lowpass Gaussian window is performed using cosine modulation. The smart interference localizer estimates the center frequency ω_c of the interference. The window generator modulates the filter $f(k)$ to the desired position according to,

$$f'(k) = f(k)\cos\left(\omega_c(k - \frac{N-1}{2})\right). \tag{5.51}$$

The performance analysis of a Binomial-Gaussian window-based exciser is exactly same as the linear prediction filter-based exciser which is explained in section 5.3.1.

5.6 Adaptive Time-Frequency Domain Exciser

5.6.1 Motivation and Description of ATF Algorithm

Figure 5.8 displays the flow diagram of the proposed adaptive time-frequency (ATF) exciser algorithm [48]. Unlike fixed transform techniques, the ATF exciser is capable of tracking and suppressing the time-varying non-stationary interferences. The novelty of the ATF exciser is two-fold. First, it evaluates the time features of the received signal in order to decide on the domain of the excision. A time window slides through the received signal and captures the samples which exceed an amplitude threshold. Then, the total number of the captured samples (N_c) is compared to a predetermined threshold (N_t). In fact, this threshold is a measure of energy distribution of the signal in the time domain. If N_c is less than or equal to N_t, then

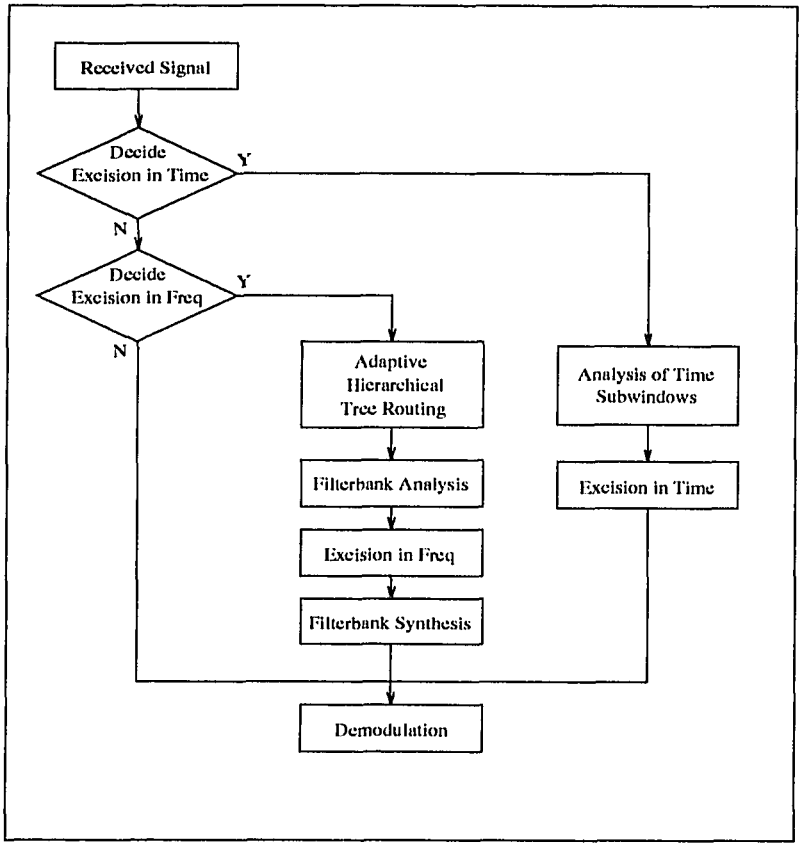

Figure 5.8 The flow diagram of the proposed adaptive time-frequency exciser algorithm.

those interfered samples are nulled in the time domain. In particular, if the interference is time localized, such a simple time domain excision technique can outperform any transform domain technique. It is clear from the uncertainty principle that, for a time localized interference, no transform domain excision technique can be justified.

The second novelty of the ATF excision algorithm is its adaptive subband basis selection mechanism. As explained in Chapter 4, the TSA examines the spectrum of the received signal and defines the most proper subband tree structure. The contaminated or jammed subbands are discarded at the synthesis stage. The subband

tree structure changes whenever the input spectrum varies. The spectral decomposition tracks to the variations of the input spectrum. If the interference does not exist or localize in any domain, the received signal is passed directly to the PN demodulator as it is shown in Figure 5.8.

The superior performance of the ATF over the existing excision techniques was reported in Ref. [49][47]. We will also include the ATF in our performance comparisons in the following section.

5.6.2 Performance of ATF under Time-Localized Wide-band Gaussian Interference

Figure 5.9 displays the performance of ATF and fixed transform-based excisers for pulsed (time-localized) wideband Gaussian interference. This jammer is an on/off type which is randomly switched with 10% duty cycle. The signal to interference power ratio is $-20dB$. In this scenario, as expected, none of the fixed transform-based excisers is effective for interference suppression. However, the ATF exciser identifies the domain of the processing and successfully suppresses interference in the time domain. The dual treatment of signal properties in time and in frequency domains obviously bring significant performance improvements.

5.7 Performance Evaluation of Interference Excision Techniques

Performance evaluations presented in this section have two purposes. First, the validity of the analytical performance analyses presented earlier is checked with the performance simulations of a few DSSS communications scenarios. Second, the performance of several competitive interference excision techniques are compared and ranked under the same test conditions.

In order to evaluate the performance of a DSSS communications receiver employing the ATF exciser, a simulations package was created. The bit error events

are counted for different simulation runs and then the results are averaged. The performance of the proposed ATF exciser along with DFT, DCT and fixed 64-band PR-QMF bank based excisers is evaluated. A 63-chip maximum length PN code is used to spread the input bit stream. This provides a white spectrum for the transmitted signal. The baseband signal bandwidth is normalized to unity and a BPSK modulation is assumed. The resulting DSSS signal is transmitted over an AWGN channel. Three types of interferences are considered; a single tone jammer, and a narrowband Gaussian jammer.

(i) Single Tone Jammer Case: A continuous sinusoidal interference with a frequency of 1.92 rad and uniformly distributed random phase ($\theta \in [0, 2\pi]$) is considered. The signal to interference power ratio is $-20dB$. The ATF exciser employs 7-band irregular filter bank structure given in Figure 5.10. It has a fine spectral resolution around the interference frequency and minimum spectral leakage to uncontaminated bands. Figures 5.11 and 5.12 display the experimental and analytical bit error rate (BER) performance of the ATF exciser-based DSSS system along with a few other fixed block transform exciser-based systems. The ideal curve represents the BPSK performance without any interference. The ATF exciser yields nearly optimal performance for sinusoidal interference. On the other hand, the fixed transforms (64-band filter bank, 128-point DFT and DCT) can not guarantee a good performance. Their performance depends on the frequency location of the interference signal. They perform relatively well if the frequency of the interfering tone exactly matches one of the transform bins. In Figures 5.11 and 5.12, the experimental and analytical BER performance of 63-point KLT and 5^{th} order LPEF are also presented.

(ii) Comparison of Analytical and Experimental Results: Figures 5.13-5.17 display the bit error rate (BER) performance of ATF, 128-point DFT, 63-point KLT, 64-band filter bank and 5^{th} order linear predictor exciser based DSSS receivers,

respectively. Each of these figures jointly presents the analytical and simulation performance results. A sinusoidal interference of $\omega = 1.765rad$ with $SIR = -20dB$ is assumed in these examples. It is observed from these results that the analytical performance studies presented are in match with the simulation performance of the DSSS communications scenarios tested.

(iii) Narrowband Gaussian Jammer Case: A continuous 10% bandwidth narrowband Gaussian interference with a center frequency of $\frac{\pi}{2}$ rad is considered. The signal to interference power ratio is $-20dB$. The 5-band irregular filter bank structure generated by ATF exciser is displayed in Figure 5.18. As seen in the figure, the narrowband interference is confined in the third subband and it is excised within this subband. The BER performances are shown in Figure 5.19. The proposed ATF exciser yields the best performance compared to the other fixed transform-based excisers, the increase in the number of excised transform bins does not necessarily improve the BER performance since the desired components of the received spectrum are also removed during the excision.

(iv) Robustness of Performance: One of the most important attributes of an interference suppression technique must be its robustness to time-varying signals. The BER performance results of the ATF exciser-based DSSS receiver for single tone jammer with varying frequency are displayed in Fig. 5.20. The similar results are displayed in Figures 5.21, 5.22, 5.23, 5.24, 5.25, and 5.26 for Binomial-Gaussian Window, 63-point KLT 64-band filter bank, 128-point DFT, 128-point DCT, and 5^{th} order LPEF exciser-based DSSS receivers. It is seen from these plots that the ATF or Binomial-Gaussian window exciser-based systems achieve an robust performance but the other conventional techniques do not.

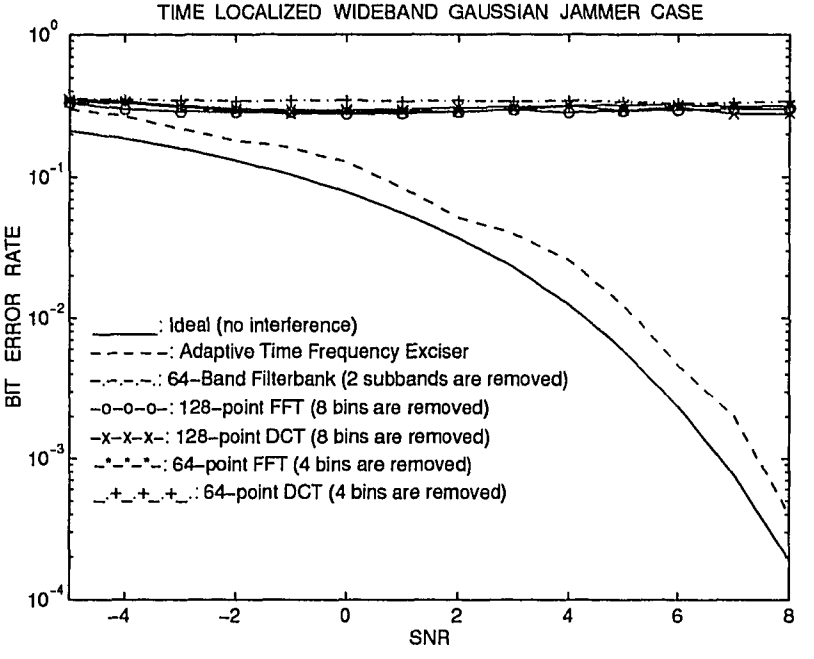

Figure 5.9 Bit error rate curves for time localized wideband Gaussian jammer case (10% duty cycle, SIR $= -20dB$).

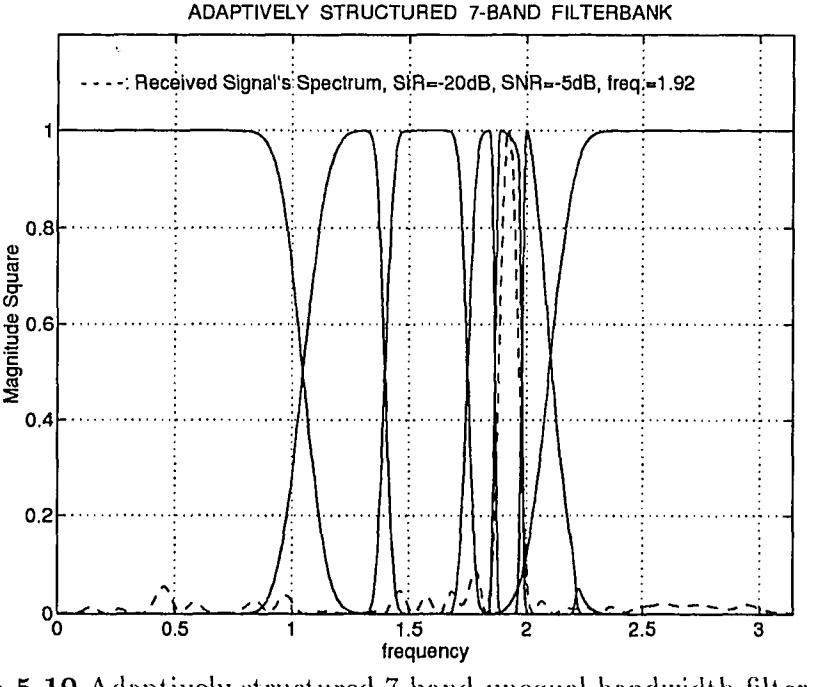

Figure 5.10 Adaptively structured 7-band unequal bandwidth filter bank.

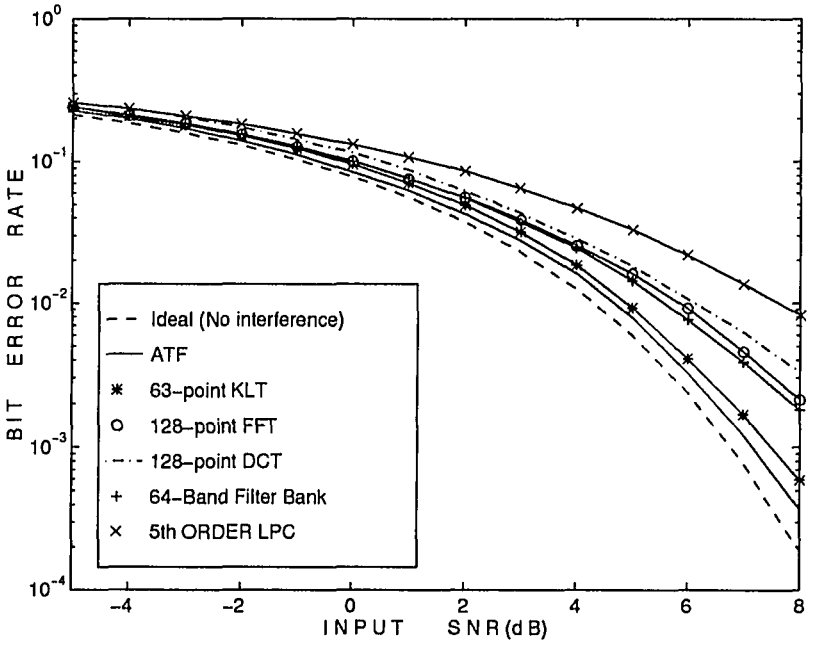

Figure 5.11 Experimental bit error rate curves for sinusoidal jammer, SIR = −20dB, tone frequency = 1.92 rad.

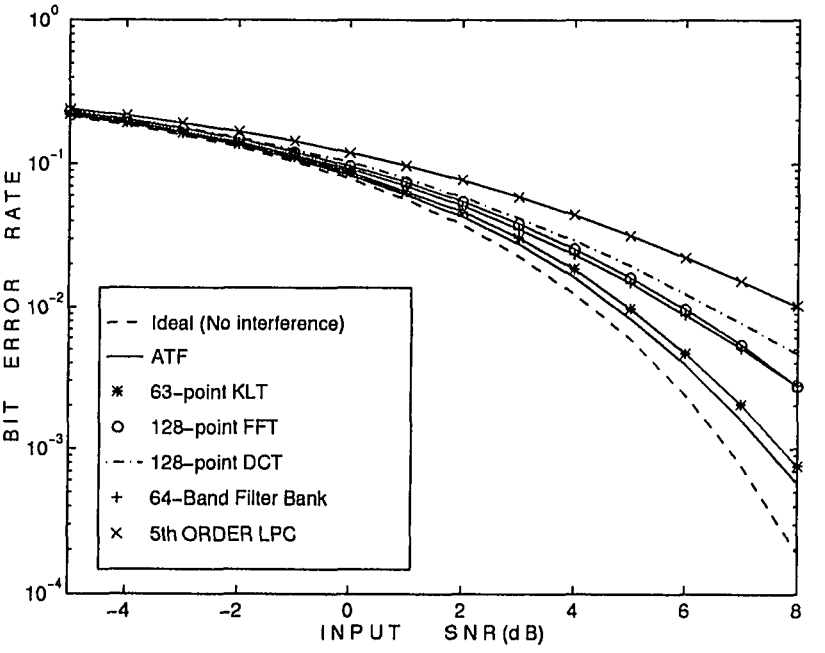

Figure 5.12 Analytical bit error rate curves for sinusoidal jammer, SIR = −20dB, tone frequency = 1.92 rad.

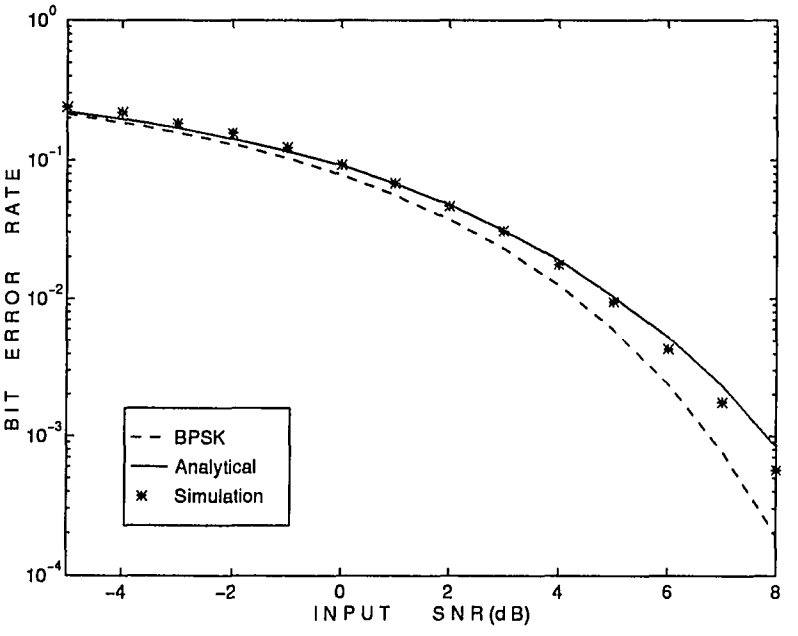

Figure 5.13 Analytical and simulation BER performance of the ATF-based exciser for sinusoidal interference (SIR=-20dB, $\omega = 1.765rad$).

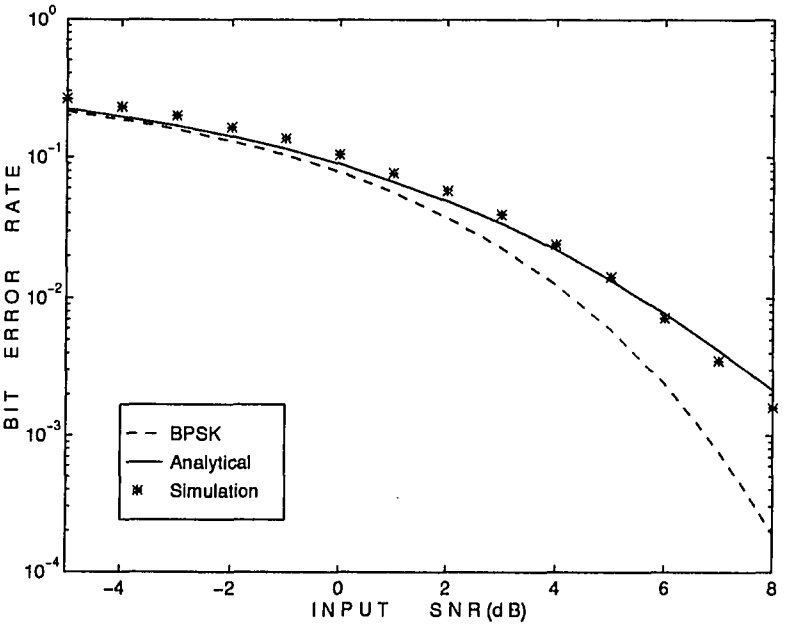

Figure 5.14 Analytical and simulation BER performance of the 128-point FFT-based exciser for sinusoidal interference (SIR=-20dB, $\omega = 1.765rad$).

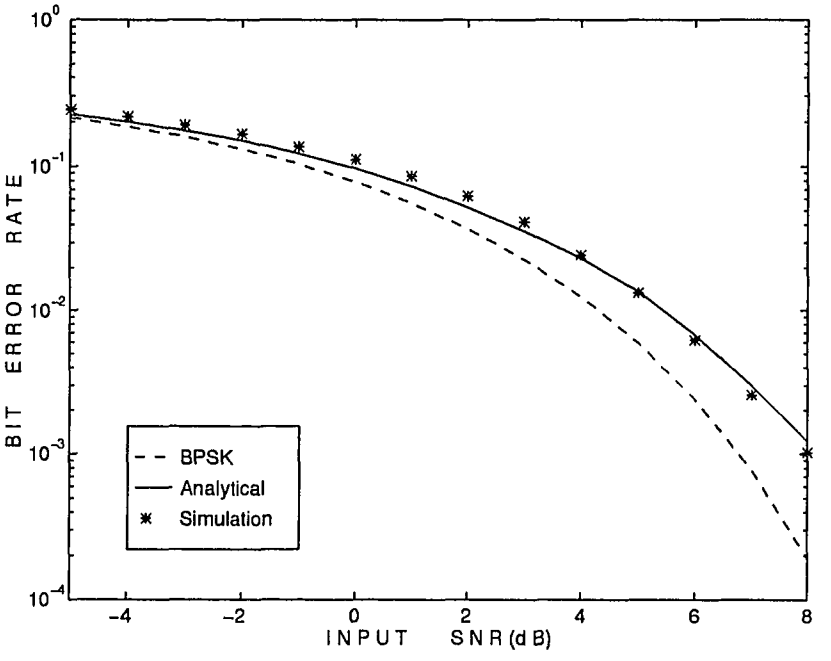

Figure 5.15 Analytical and simulation BER performance of the 63-point KLT-based exciser for sinusoidal interference (SIR=-20dB, $\omega = 1.765rad$).

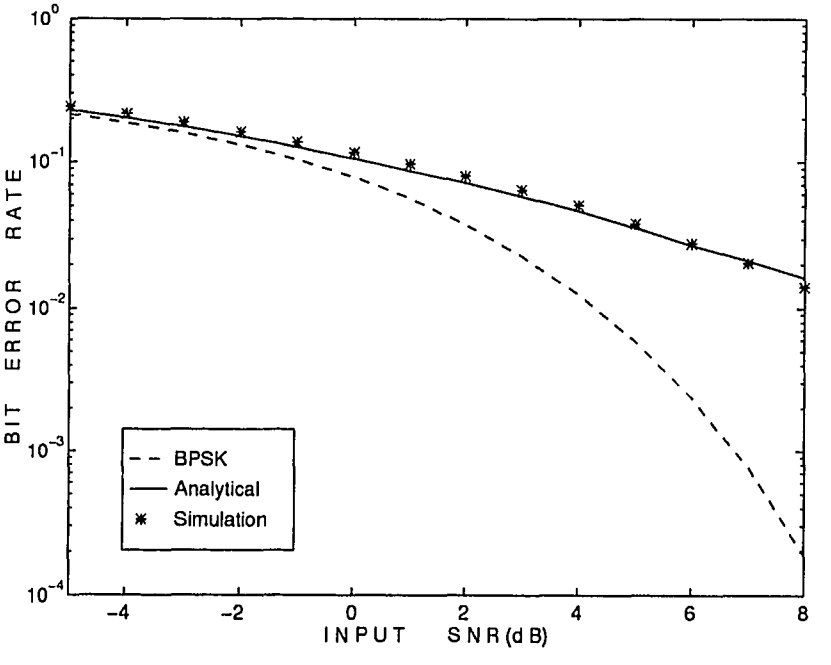

Figure 5.16 Analytical and simulation BER performance of the 64-band filter bank-based exciser for sinusoidal interference (SIR=-20dB, $\omega = 1.765rad$).

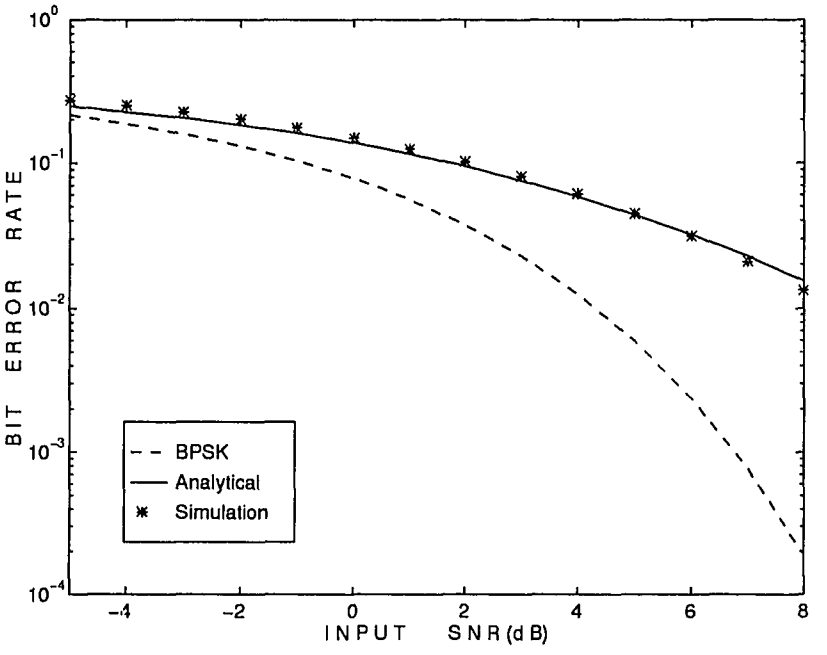

Figure 5.17 Analytical and simulation BER performance of the 5^{th} order LPEF-based exciser for sinusoidal interference (SIR=-20dB, $\omega = 1.765rad$).

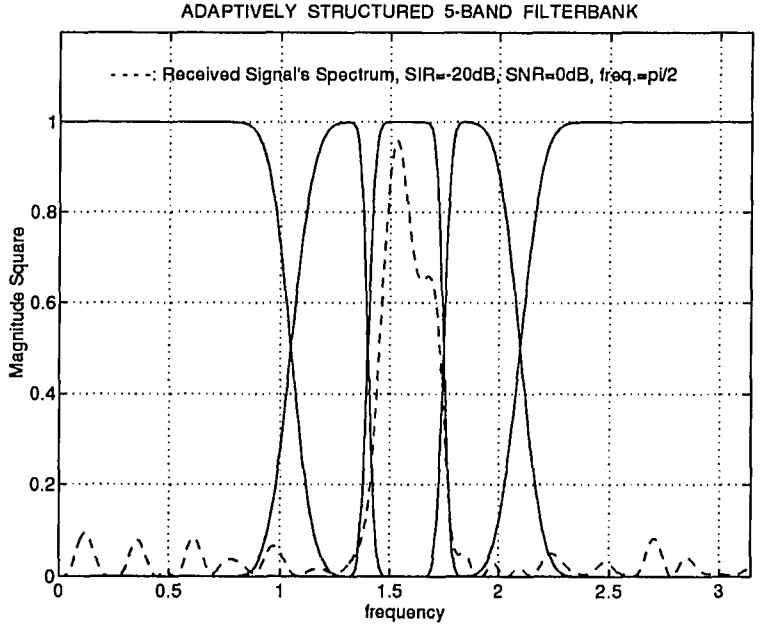

Figure 5.18 Adaptive filter bank structure for narrowband Gaussian jammer case (center frequency = $\frac{\pi}{2}rad$, SIR = $-20dB$, SNR = $0dB$).

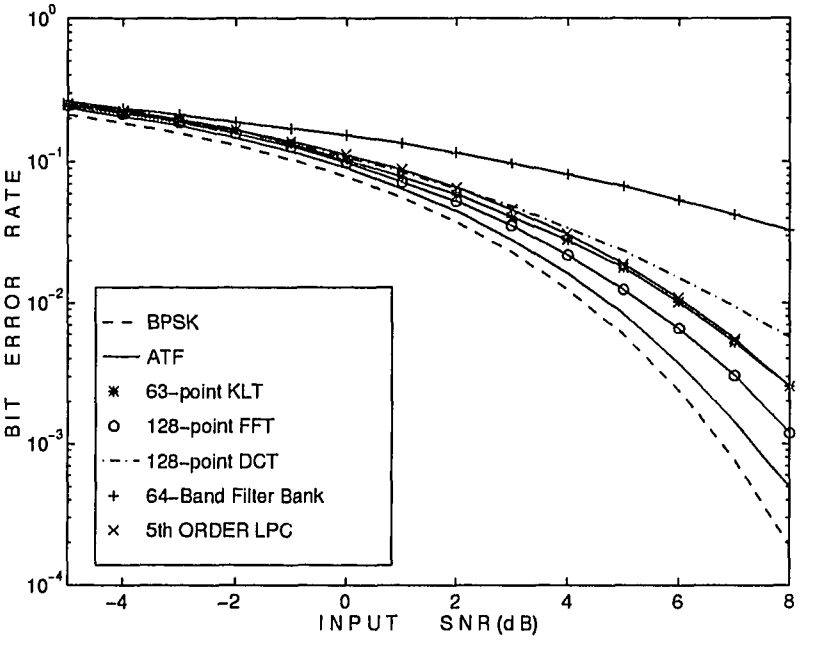

Figure 5.19 Bit error rate curves for frequency localized narrowband Gaussian jammer case (center frequency = $\frac{\pi}{2} rad$, SIR = $-20dB$).

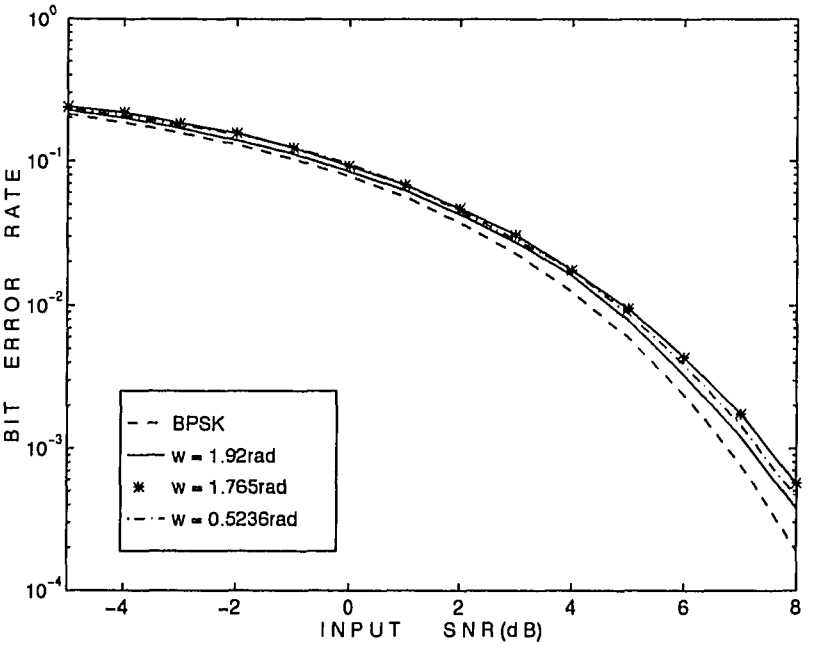

Figure 5.20 Bit error rate curves of adaptive subband transform-based exciser for different frequency tone jammers (SIR = $-20dB$, $\omega_1 = 0.5236 rad$, $\omega_2 = 1.765 rad$, $\omega_3 = 1.92 rad$)

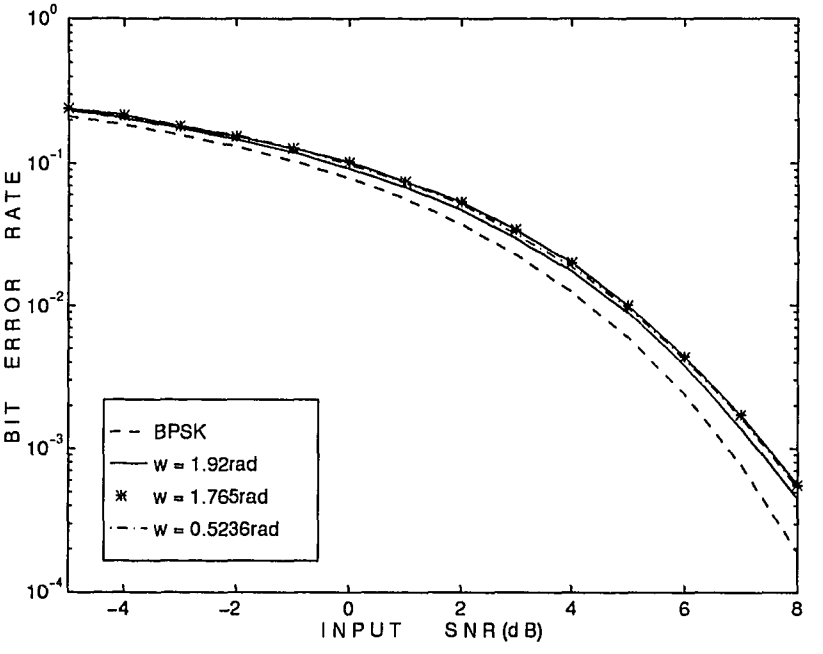

Figure 5.21 Bit error rate curves of cosine modulated Binomial-Gaussian window-based exciser for different frequency tone jammers (SIR = $-20dB$, $\omega_1 = 0.5236rad$, $\omega_2 = 1.765rad$, $\omega_3 = 1.92rad$)

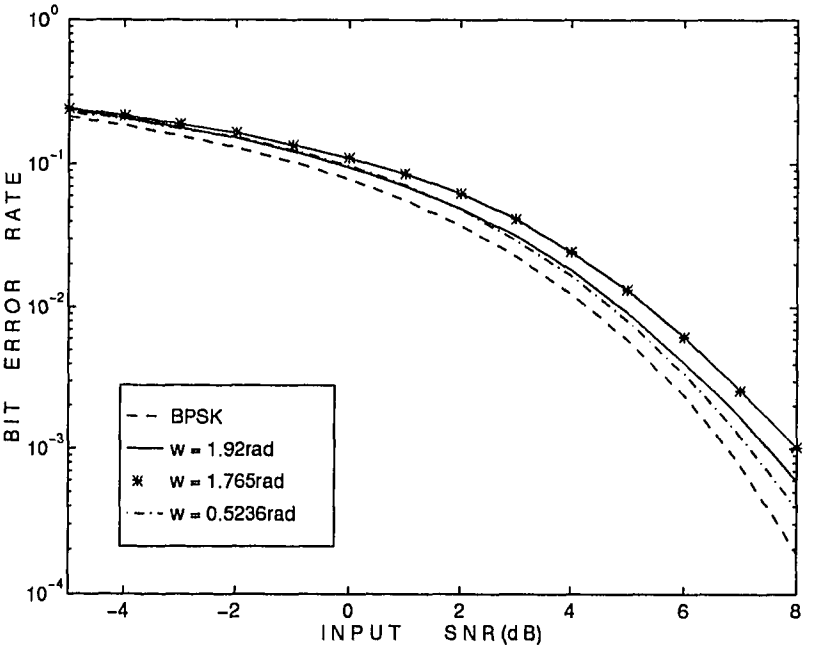

Figure 5.22 Bit error rate curves of 63-point KLT exciser for different frequency tone jammers (SIR = $-20dB$, $\omega_1 = 0.5236rad$, $\omega_2 = 1.765rad$, $\omega_3 = 1.92rad$)

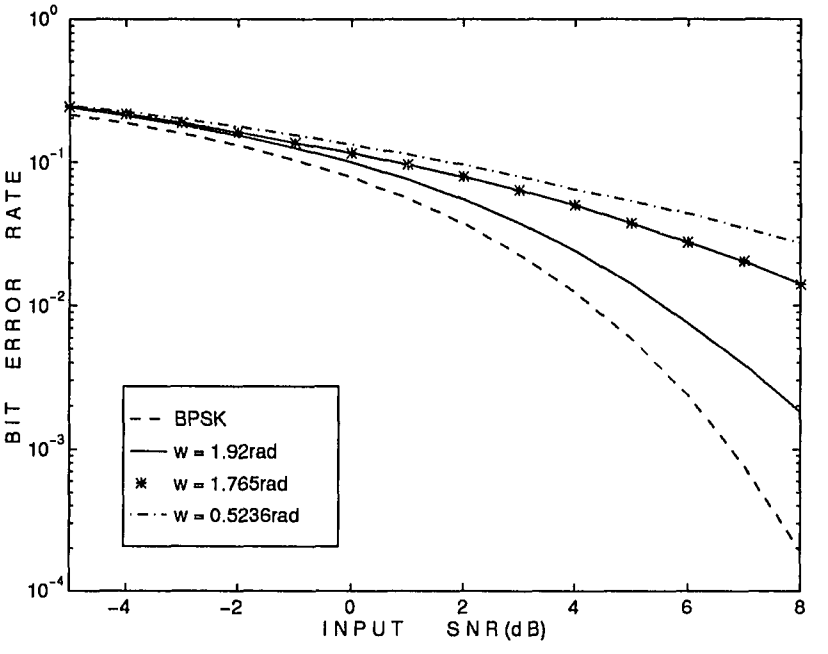

Figure 5.23 Bit error rate curves of 64-band regular filter bank exciser for different frequency tone jammers (SIR $= -20dB$, $\omega_1 = 0.5236rad$, $\omega_2 = 1.765rad$, $\omega_3 = 1.92rad$)

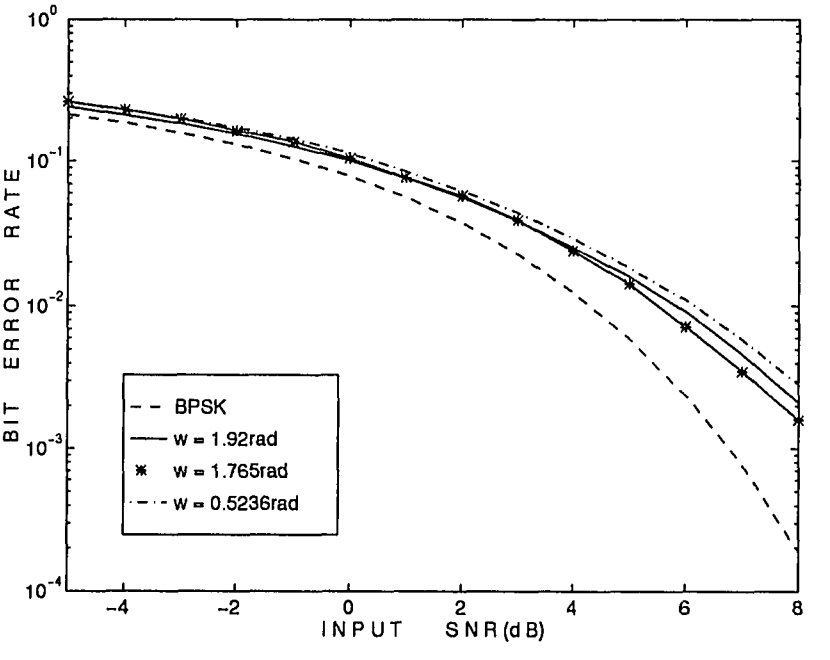

Figure 5.24 Bit error rate curves of 128-point DFT exciser for different frequency tone jammers (SIR $= -20dB$, $\omega_1 = 0.5236rad$, $\omega_2 = 1.765rad$, $\omega_3 = 1.92rad$)

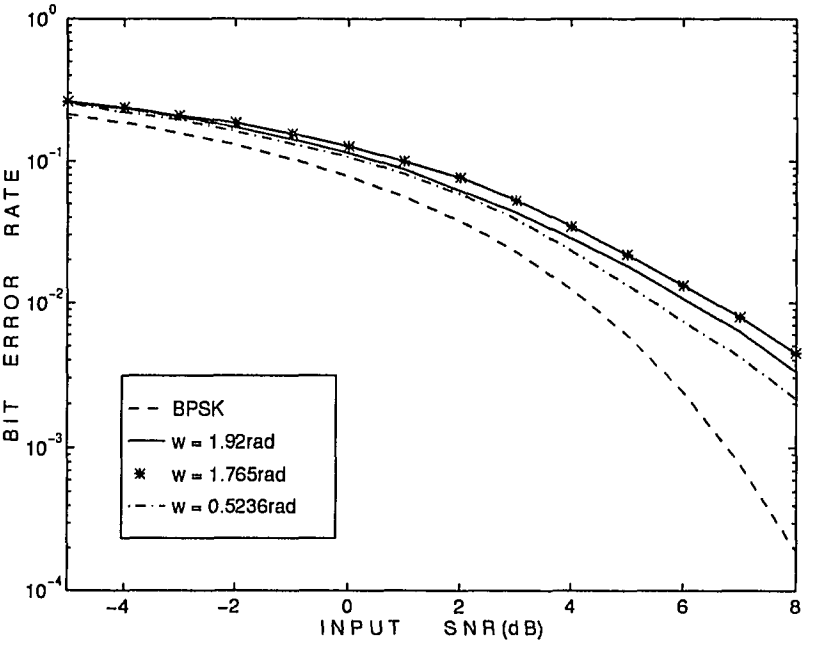

Figure 5.25 Bit error rate curves of 128-point DCT exciser for different frequency tone jammers (SIR = $-20dB$, $\omega_1 = 0.5236rad$, $\omega_2 = 1.765rad$, $\omega_3 = 1.92rad$)

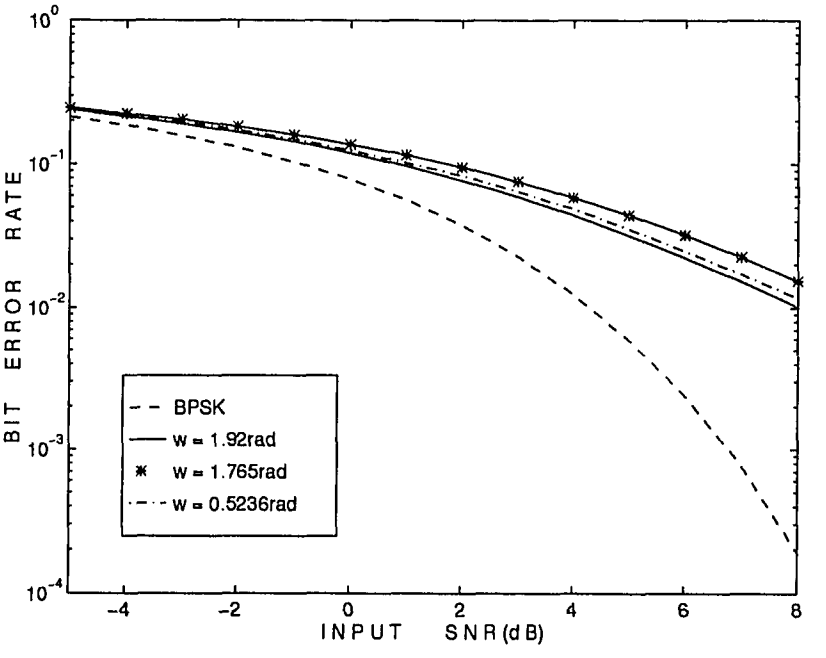

Figure 5.26 Bit error rate curves of linear prediction filter-based exciser for different frequency tone jammers (SIR = $-20dB$, $\omega_1 = 0.5236rad$, $\omega_2 = 1.765rad$, $\omega_3 = 1.92rad$)

CHAPTER 6

TIME-FREQUENCY ANALYSIS OF BIOLOGICAL SIGNALS

Time-frequency signal representations characterize signals over a time-frequency plane. They combine time and frequency information to yield a potentially more revealing picture of the temporal localization of a signal spectrum. Time-frequency (TF) representations have been applied to analyze non-stationary or time-varying signals. Hence, TF representations provide excellent platforms for biological signals because of their high non-stationarity.

The TF representations of signals can be classified as linear and quadratic. The linear TF representations might be the short-time Fourier transform (STFT) and the wavelet transform. All linear TF representations satisfy the superposition or linearity principal. Linearity is a desirable property in any application involving multicomponent signals. On the other hand, the quadratic TF representations provide a time-frequency energy distribution or instantaneous power spectrum [23]. They are called quadratic since the energy is a quadratic signal representation. An energy distribution-based TF representation tries to combine the instantaneous power and the spectral energy density. The temporal and spectral correlations can also be combined as an alternative quadratic representation [23]. In reality signals may have unknown spectral components . In that case, TF representations may suffer significantly from cross-terms of these spectral components. This problem may be partially overcome by designing specific kernels for the signal at hand. This solution, however, requires stationarity in the signal. Unfortunately, this is not always the case, especially, for biological signals.

In the following sections, we explore the possibility of better representation of a particular biological signal, namely heart rate variability (HRV). It is known that there is a close relationship between the autonomic nervous system and HRV. A non-

invasive analysis of sympathetic and parasympathetic components of the autonomic nervous system can be obtained by power spectral analysis of HRV [13][6]. The power spectral analysis, however, does not provide any temporal or time-localized information. Recently, time-frequency analysis of HRV signals has been suggested to provide temporal changes. Hence, the crossterms resulting from some of the TF analysis methods raise significant difficulties. We present a new method to overcome this problem [51]. First, the heart rate signal is analyzed with the existence of a reference signal. Then, HRV is spectrally tailored yielding to parasympathetic activity only. Finally, an STFT is utilized on the processed data in order to obtain a TF representation.

6.1 Heart Rate Variability

Characterizing and quantifying heart rate variability for diagnosis has been shown to be potentially useful in a number of clinically important conditions [6][38]. The HRV signal is basically computed from the electrocardiographic (ECG) signal. The computation of HRV actually involves detection of the R wave in the QRS complex of the ECG signal (Figure 6.1(a)) [42]. The ECG signal is recorded and sampled at a sufficiently high rate ($f_s = 200Hz$) to precisely locate the QRS-complex. The ECG signal is first passed through an R-wave detector which produces a rectangular pulse each time an R wave is detected (Figure 6.1(b)). Then, the interbeat interval (IBI) signal is calculated as a function of intervals between R-waves, as displayed in Figure 6.1(c). The discrete values of IBI are, however, not equidistant along the time axis. In order to produce equidistant IBI signals, interpolation is needed. Thus, there is no new information from one beat to the other one, so all of the interpolated values between a beat at time T_{m-1} and the next beat at time T_m are set to equal to the time difference between T_m and T_{m-1}, which is actually the IBI.

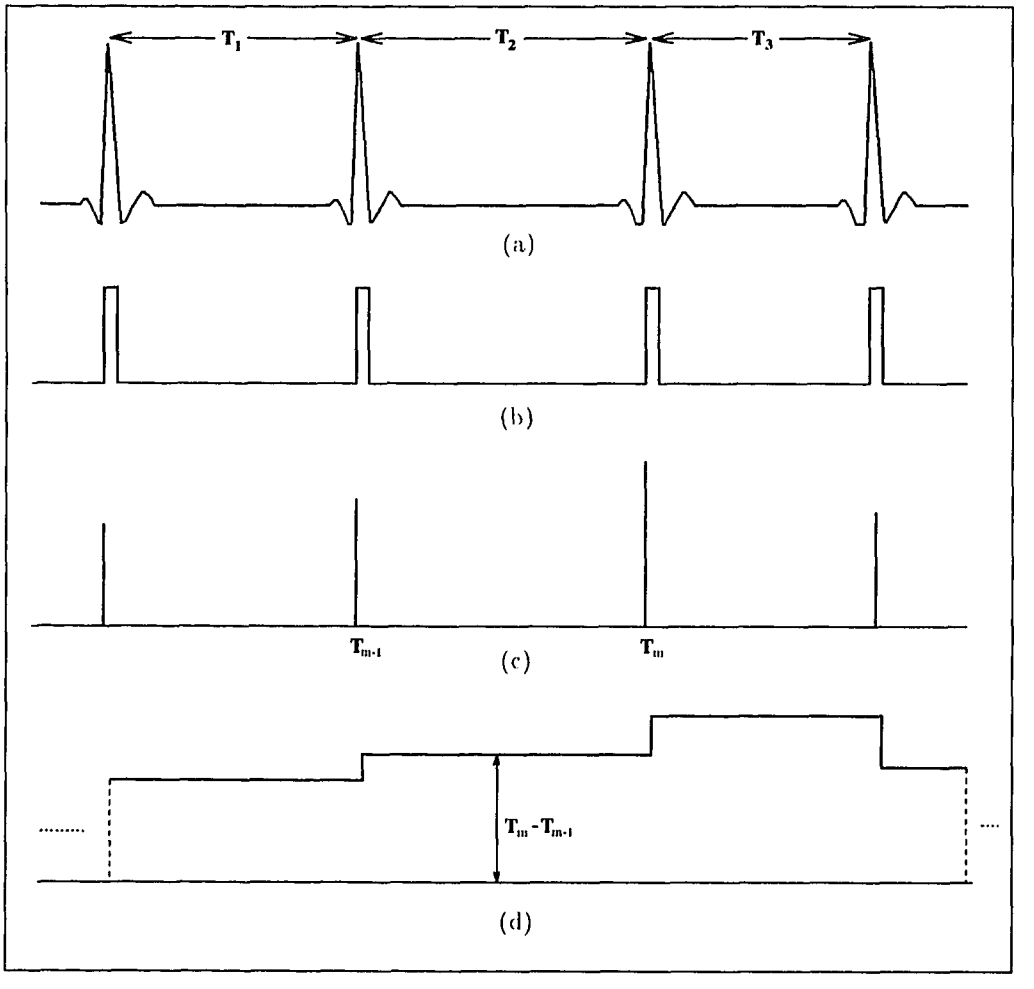

Figure 6.1 The computational steps of the HRV signal: (a) electrocardiographic signal, (b) R-wave detection, (c) interbeat interval, (d) HRV signal (interpolated IBI).

6.2 Linkages of HRV with Autonomic Nervous System and Respiration

The heart rate constantly changes in response to physiological perturbations. Heart rate responses in intact people are mainly due to the integrated responses of both major branches of the autonomic nervous system [7]. Sympathetic input generally increases heart rate while parasympathetic input decreases it. Furthermore, changes in heart rate often reflect the reciprocal action of the sympathetic and parasympathetic systems. It is usually not possible to distinguish sympathetic influences from parasympathetic influences. Typically, this problem has been approached by studying the heart rate changes after one branch of the autonomic nervous system has been blocked surgically or pharmacologically.

Sayers and others have characterized the power spectrum of normal HRV with three major peaks [41][13]. The first peak is in a very low frequency band (VLF, 0.02-0.06Hz). The second one is a in a low frequency band (LF, 0.06-0.15Hz). The last peak is at a high frequency band (VLF, 0.15-0.4Hz). Akselrod et al. studied the origin of these peaks pharmacologically [6]The HF band has been equated to peak frequency of the respiration signal [16]. This respiration peak corresponds to the sinus arrhythmia and it is purely parasympathetic in origin. While the HF band is mediated by parasympathetic pathways, the LF band is mediated by both parasympathetic and sympathetic pathways. Assessment of parasympathetic activity from spectrum analysis can be obtained via a measurement of the area under the HF peak.

6.3 Data Collection

In this study, ten normal subjects (aged 19-53) participated in a cycling protocol. The procedure consisted of riding a cycle ergo-meter at $80 rev/min$. The initial workload consisted of pedaling at $80 rev/min$ in an unloaded condition. Then after, the workload was varied such that the subject was maintained at a heart rate of 70%

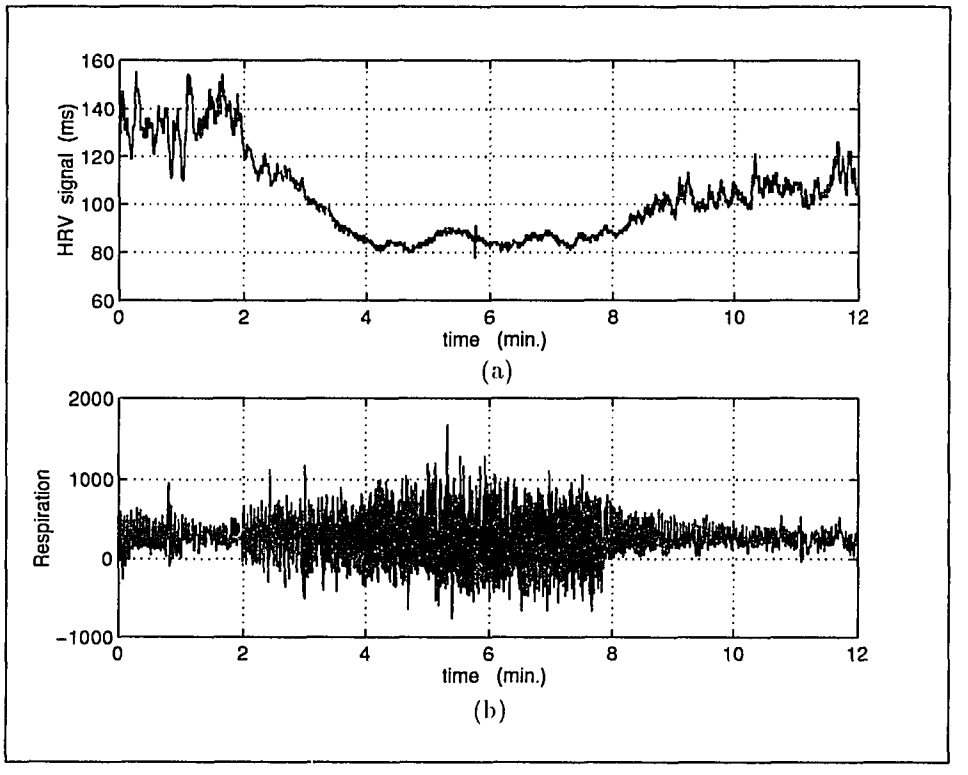

Figure 6.2 (a) The HRV and (b) respiration signals for subject N0719.

of the age-predicted maximum. The subjects first sat on a bicycle for two minutes at rest, and were then instructed to pedal comfortably for two minutes until their heart rate achieved 70% of the age-predicted maximum. This pace was maintained for another four minutes, covering a total of six minutes of exercise. The subjects were then instructed to halt and rest without physical exertion for four minutes.

A ECG monitor was used to acquire leads I,II, and III of the ECG. The resulting signal was then acquired by a computer using an analog-to-digital converter. The time intervals between consecutive peaks of the QRS complexes were stored as the IBI. The IBI was collected during the cycling protocol in a twelve minute continuous file, along with a respiration signal to avoid the loss of any information during

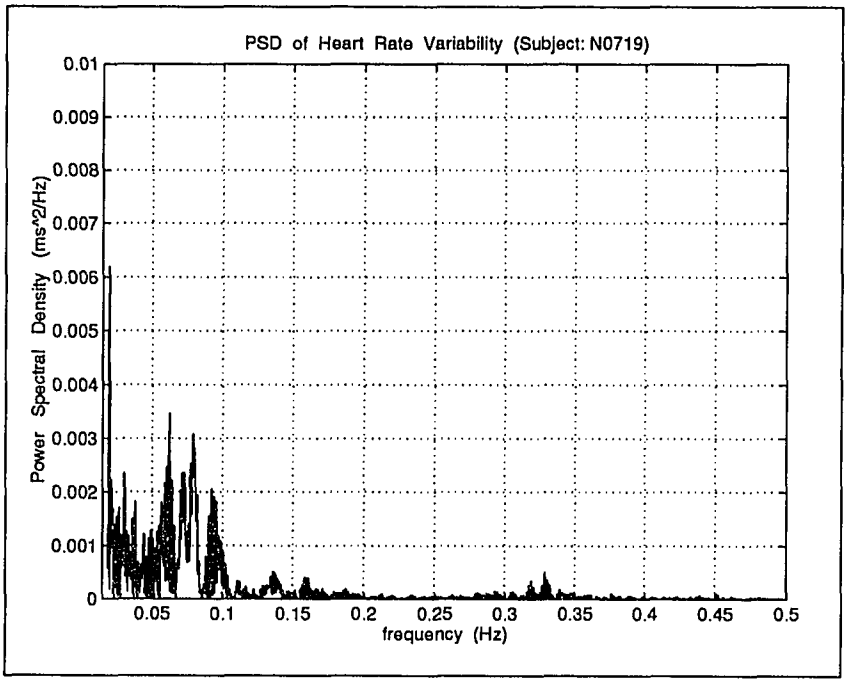

Figure 6.3 The power spectral density function of HRV (Subject: N0719).

transitions. Figure 6.2 displays an example of the HRV signal, along with respiration during the exercise protocol.

6.4 Power Spectral Analysis and STFT of HRV

The power spectral analysis of HRV can not show its temporal changes. There are, however, many situations of physiological interest where heart rate changes rapidly over time and the monitoring of these temporal changes may be of considerable interest. Figure 6.3 displays the power spectral density function of the HRV signal shown in Figure 6.2. It is clear from this figure that the parasympathetic activity in desired frequency band [0.15,0.5] is averaged.

The TF representations are perfect candidates to monitor temporal-spectral changes. For example, the size-N DFT of a sequence extracted from $x(n)$ [from $x(n)$

to $x(n+N-1)]$ can be written as [37]

$$\Gamma(k,n) = \sum_{l=0}^{N-1} x(l+n)e^{-j\frac{2\pi kl}{N}}. \quad (6.1)$$

We can use a sliding window $w(m)$ of length N, which is non-zero only for the interval $(n \leq m \leq n+N-1)$. Thus, we can rewrite Eq.(6.1) as

$$\Gamma(k,n) = \sum_{l=-\infty}^{\infty} x(l)w(l)e^{-j\frac{2\pi k}{N}(l-n)}. \quad (6.2)$$

If $w(l)$ is a rectangular function, then Eqs.(6.1) and (6.2) are equivalent. Figure 6.4 displays a TF representation of a signal (employing a rectangular window for the STFT).

6.5 Adaptive Time-Frequency Analysis of HRV using Respiration Reference

Our motivation is to uncover the region of true parasympathetic activity. It is very well known that parasympathetic activity is highly correlated with the respiration frequency. An adaptive analysis method that traces the respiration frequency and extracts the corresponding parasympathetic activity from the HRV signal is proposed in this section.

In particular, the parasympathetic activity can be precisely extracted from the HRV signal by using a sliding frequency window with an adaptive bandwidth. A cosine-modulated binomial-Gaussian function will be excellent match for this purpose because of its simplicity, smooth frequency response and excellent frequency localization. The generic block diagram of the adaptive time-frequency analysis method is shown in Figure 6.5. The method proceeds as follows:

(I) First, the respiration and HRV signal are broken into overlapping time windows to reflect the temporal changes of vagal activity over time and frequency. For a typical subject, the window length is chosen as 150 samples (7.5 secs), where

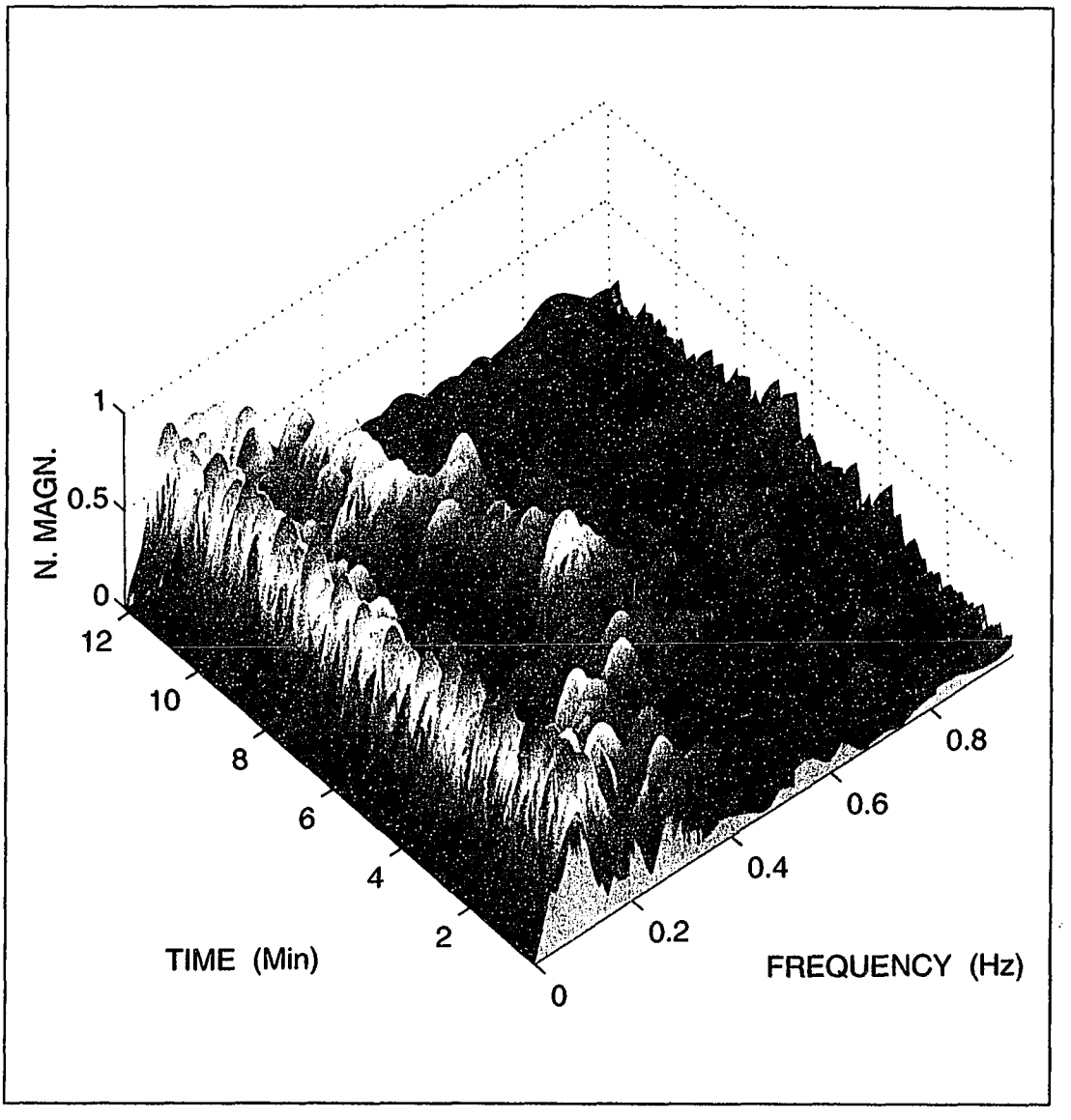

Figure 6.4 TF representation of the HRV, employing the STFT with a rectangular window (length=150 and overlapping amount=32) (Subject: N0719).

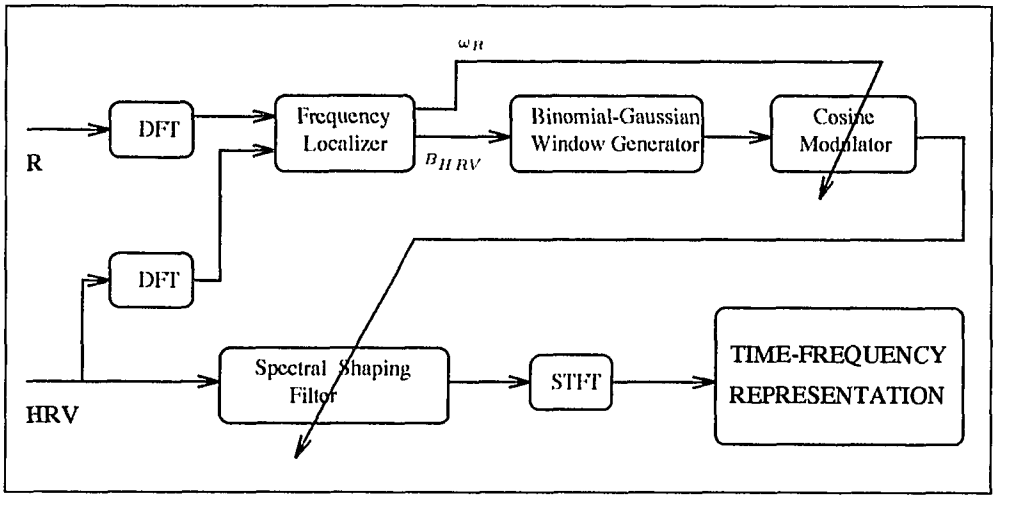

Figure 6.5 The generic block diagram of adaptive time-frequency analysis.

each successive window is shifted by 32 samples (1.6 secs) from the previous one. These particular values are chosen such that the temporal changes can be closely monitored during the analysis.

(II) Second, a smart frequency localizer examines the peak frequency of the respiration (ω_R). Also, the frequency localizer detects the half-power bandwidth of the respiration peak in the HRV (B_{HRV}) in that particular time window.

(III) The binomial-Gaussian generator produces an M-tap, low-pass prototype (f_p), with the given approximate bandwidth (B_{HRV}).

(IV) The low-pass prototype is modulated to the respiration peak frequency by means of cosine modulation, as

$$f(k) = f_p(k)cos[\omega_r(k - \frac{N-1}{2})]. \tag{6.3}$$

(V) The HRV data segment is filtered or shaped with the bandpass filter given in Eq.6.3.

(VI) The STFT is applied on the filtered HRV signal, and TF plots are finally obtained.

(VII) The window is shifted through the HRV and respiration signals. The procedures (through VII) are repeated until the end of the data files.

Figure 6.6 displays a normalized power spectrum of a typical subject's HRV on the time-frequency plane without any processing. As seen from the figure, the desired information is smeared with the undesired information. After adaptive tailoring of the HRV by binomial-Gaussian filtering, however, the desired parasympathetic activity becomes clearly visible, as shown in Figure 6.7. In some cases HRV signal may not be clear (Figure 6.8) then the advantage of this method becomes more clear (Figure 6.9).

Although the proposed method is a non-parametric analysis, the time-frequency properties of the analyzed signals are closely monitored and utilized in TF analysis. The Binomial-Gaussian window used here is by no means optimal, but it does provide precise results. Also the STFT may not be the only alternative for the TF-representation. Other TF-representations such as Wigner-Wille or Choi-Williams are also expected to yield good results after adaptive treatment of the HRV signal. Note that the signal is almost tailored to a single component so that the effect of cross-terms would naturally be minimal. For example, the TF-representation of a chirp signal is perfect since it is a single component signal with time-varying frequency. In conclusion a TF representation would benefit greatly if the biological signal can be tailored before any TF operation.

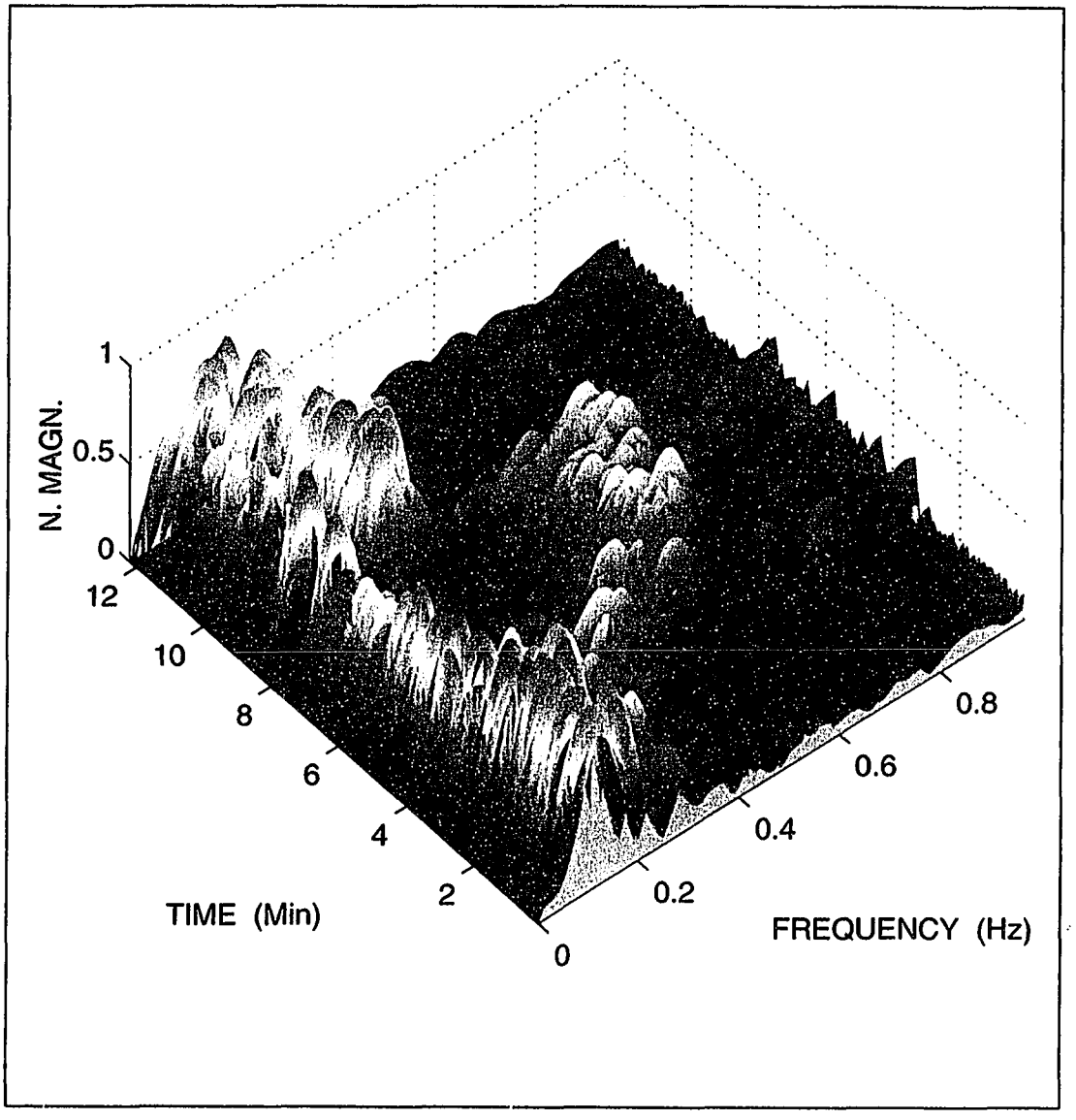

Figure 6.6 TF representation of the HRV without adaptive analysis (length=150 and overlapping amount=32) (Subject: G0719).

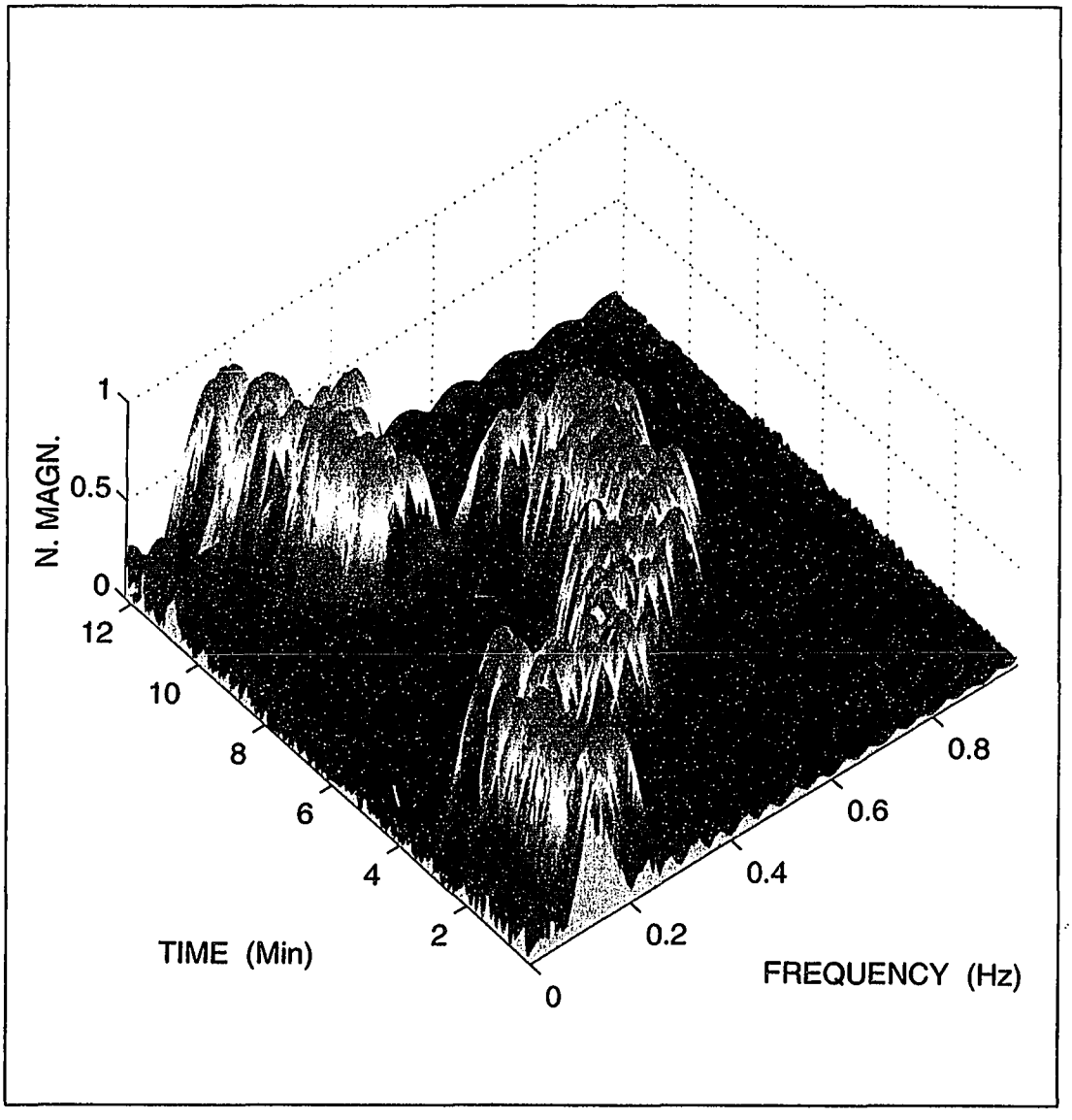

Figure 6.7 TF representation of the HRV with adaptive analysis (length=150 and overlapping amount=32) (Subject: G0719).

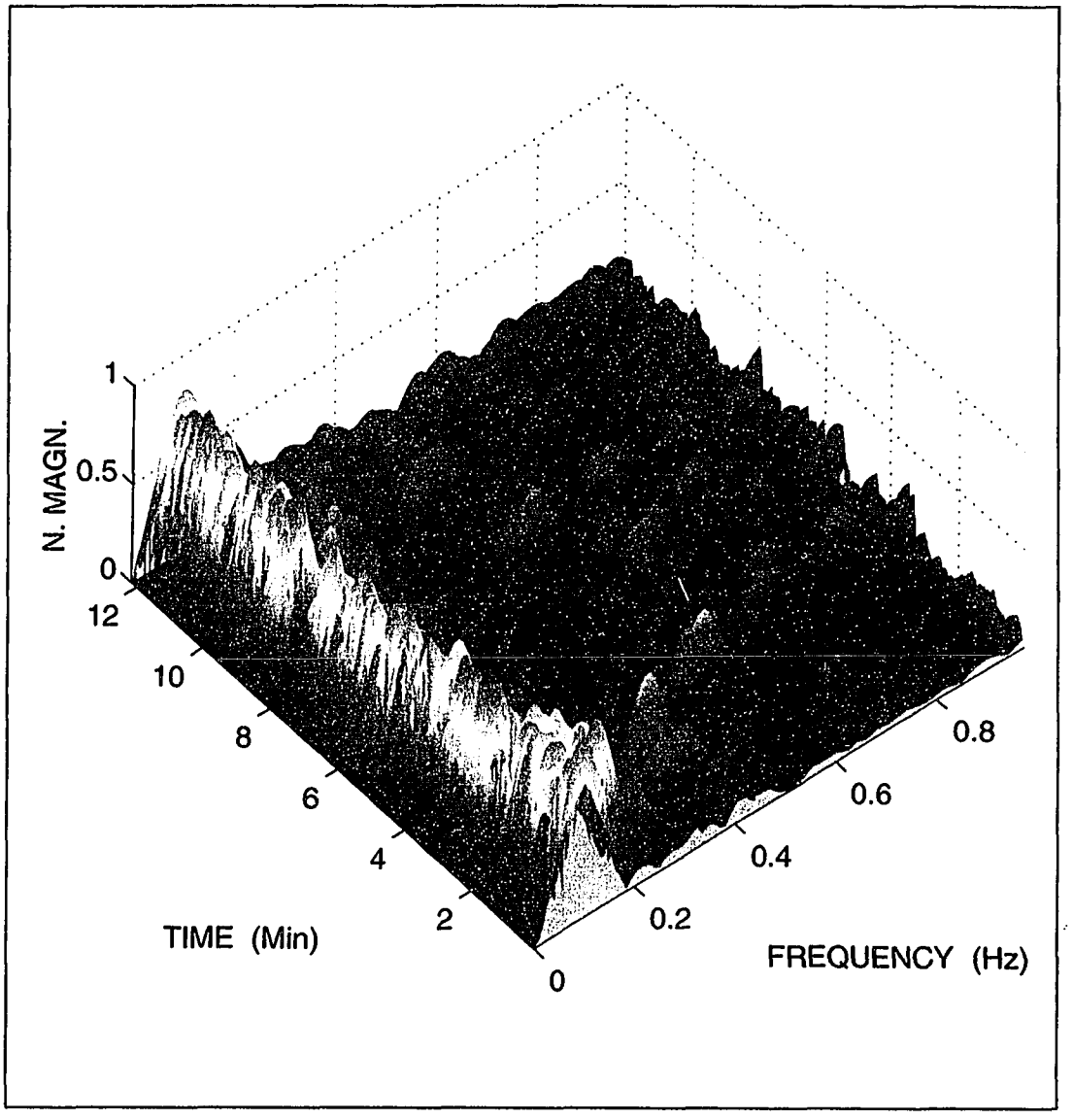

Figure 6.8 TF representation of the HRV without adaptive analysis (length=150 and overlapping amount=32) (Subject: R0719).

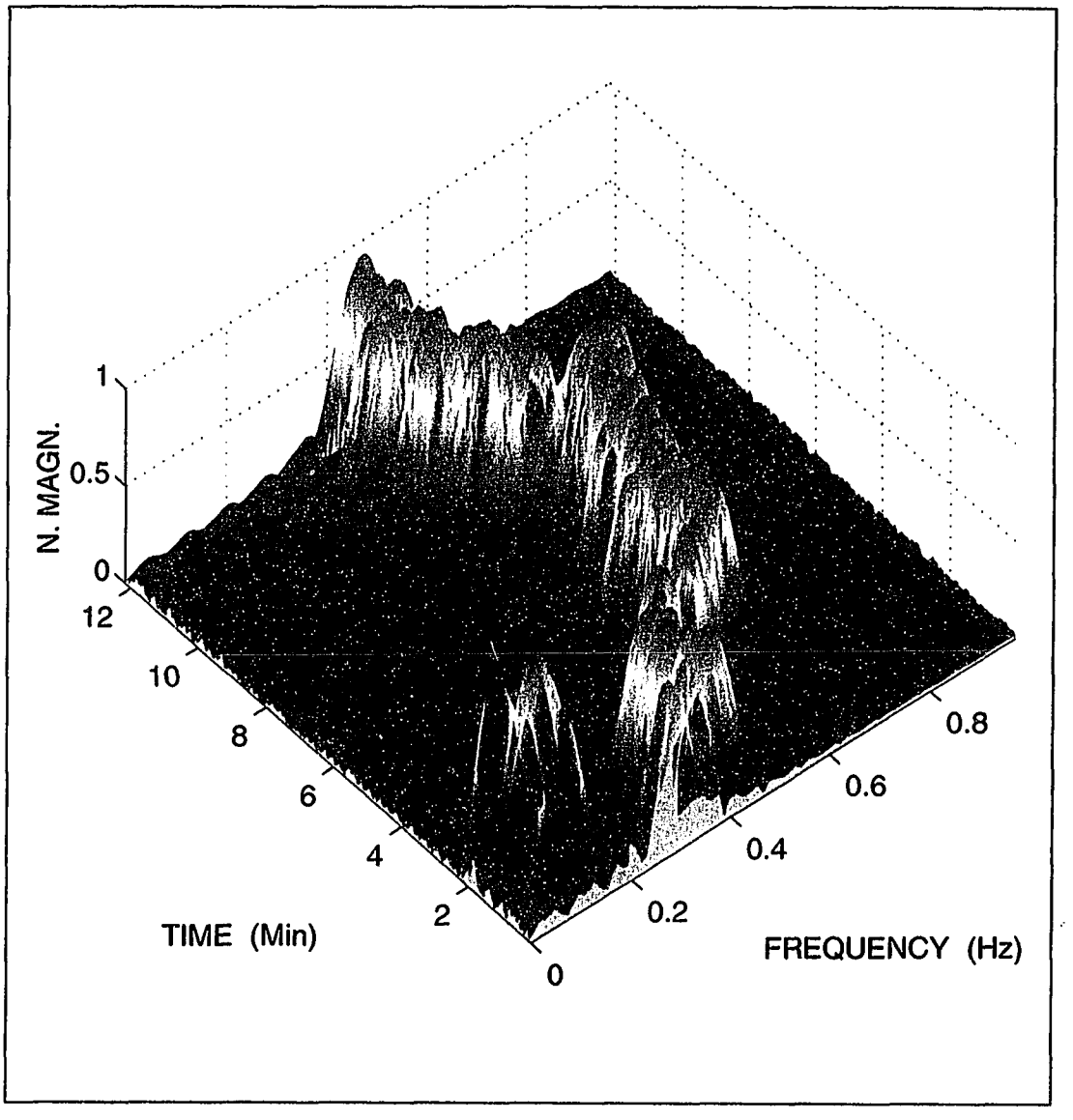

Figure 6.9 TF representation of the HRV with adaptive analysis (length=150 and overlapping amount=32) (Subject: R0719).

CHAPTER 7

CONCLUSIONS

The purpose of this dissertation was to gain insight into multirate signal decomposition through the optimal design problem and potential applications. In examining the design techniques, we found that the optimality of the hierarchical filter banks reported in the literature needs to be seriously questioned. The M-band filter bank hierarchical or direct structure was revisited and a new method, namely progressive optimality, was proposed for the optimal design problem. The progressive optimality concept suggested the step-by-step design of an M-band equal or unequal bandwidth filter bank in a hierarchical tree. As a matter of fact, the M-band hierarchical filter bank was optimized such that the final product filters were assured to be optimal. A number of examples were presented. We also tested several subband image coding scenarios for practical verification. The results highlighted some performance improvements in subband image coding, as expected. The problem of the best basis function selection was also questioned and the adaptive subband transforms based on tree structuring were studied within this context. The adaptability of the tree structures, complexity, and arbitrary time-frequency tiling were briefly examined.

Next, we investigated the applications of linear transforms for an interference excision problem in direct sequence spread spectrum communications. We studied different interference excision techniques along with the proposed adaptive time-frequency excision algorithm. The adaptive time-frequency excision algorithm basically monitors the time and frequency properties of the received signal. Furthermore, a simple windowing method, cosine modulated Binomial-Gaussian, was also proposed as an efficient transform-domain exciser. The robustness of the different methods against different types of jammers were researched. The analytical

results were derived and extensive computer simulations were performed for signal-to-noise-and-interference ratio improvement and bit error rate performance measures of all tested schemes.

The final research topic concentrated on spectral processing of a particular biological signal; namely heart rate variability. It is very well known that HRV and the autonomic nervous system are interconnected. The motivation here was to adaptively extract a certain subspectrum of HRV that corresponds to the parasympathetic activity of the autonomic nervous system. An adaptive pre-processing method based on a cosine-modulated Binomial-Gaussian window was utilized. For this case, the respiration signal's peak frequency is used as a reference. A linear time-frequency representation operator was applied on the resulting signal. Finally, we showed that the pre-processing of an HRV signal clearly improves the time-frequency representation.

APPENDIX A

SUBBAND IMAGE CODING TEST RESULTS

FILTER COMBINATION : FIRST STAGE / SECOND STAGE / THIRD STAGE
16-TAP UNCORR. / 8-TAP MULTIPLIERLESS / 6-TAP MULTIPLIERLESS

10-BAND IMAGE CODEC

bit rate = 0.2bits/pixel
SNR = 26.42dB

64-BAND IMAGE CODEC

bit rate = 0.2bits/pixel
SNR = 26.17dB

Figure A.1 Perceptual performance comparison of 10-band dyadic and 64-band regular 2-D subband image codecs for given filter combination (bit rate = 0.2bits/pixel).

FILTER COMBINATION : FIRST STAGE / SECOND STAGE / THIRD STAGE
16-TAP UNCORR. / 8-TAP MULTIPLIERLESS / 6-TAP MULTIPLIERLESS

10-BAND IMAGE CODEC

bit rate = 0.5bits/pixel
SNR = 30.20dB

64-BAND IMAGE CODEC

bit rate = 0.5bits/pixel
SNR = 30.57dB

Figure A.2 Perceptual performance comparison of 10-band dyadic and 64-band regular 2-D subband image codecs for given filter combination (bit rate = 0.5bits/pixel).

FILTER COMBINATION : FIRST STAGE / SECOND STAGE / THIRD STAGE
16-TAP UNCORR. / 8-TAP MULTIPLIERLESS / 6-TAP MULTIPLIERLESS

10-BAND IMAGE CODEC

bit rate = 1bit/pixel
SNR = 34.88dB

64-BAND IMAGE CODEC

bit rate = 1bit/pixel
SNR = 34.89dB

Figure A.3 Perceptual performance comparison of 10-band dyadic and 64-band regular 2-D subband image codecs for given filter combination (bit rate = 1bit/pixel).

FILTER COMBINATION : FIRST STAGE / SECOND STAGE / THIRD STAGE

16-TAP UNCORR. / 16-TAP UNCORR. / 16-TAP UNCORR.

10-BAND IMAGE CODEC

bit rate = 0.2bits/pixel

SNR = 26.13dB

64-BAND IMAGE CODEC

bit rate = 0.2bits/pixel

SNR = 26.25dB

Figure A.4 Perceptual performance comparison of 10-band dyadic and 64-band regular 2-D subband image codecs for given filter combination (bit rate = 0.2bits/pixel).

FILTER COMBINATION : FIRST STAGE / SECOND STAGE / THIRD STAGE

16-TAP UNCORR. / 16-TAP UNCORR. / 16-TAP UNCORR.

10-BAND IMAGE CODEC

bit rate = 0.5bits/pixel

SNR = 29.80dB

64-BAND IMAGE CODEC

bit rate = 0.5bits/pixel

SNR = 30.08dB

Figure A.5 Perceptual performance comparison of 10-band dyadic and 64-band regular 2-D subband image codecs for given filter combination (bit rate = 0.5bits/pixel).

FILTER COMBINATION : FIRST STAGE / SECOND STAGE / THIRD STAGE

16-TAP UNCORR. / 16-TAP UNCORR. / 16-TAP UNCORR.

10-BAND IMAGE CODEC

bit rate = 1 bit/pixel

SNR = 34.06dB

64-BAND IMAGE CODEC

bit rate = 1 bit/pixel

SNR = 34.43dB

Figure A.6 Perceptual performance comparison of 10-band dyadic and 64-band regular 2-D subband image codecs for given filter combination (bit rate = 1bits/pixel).

APPENDIX B

DERIVATIONS FOR THE MEAN AND THE VARIANCE VALUES OF THE DECISION VARIABLE

B.1 Linear Prediction-Based Exciser Case

(i) The mean value of the decision variable ξ for linear prediction-based exciser case:

We will derive the three terms in Eq. 5.13 as the following. Using Eqs. (5.9) and (5.10)

$$\begin{aligned} E[\xi_1] &= E[\sum_{k=1}^{L} c_0(k)c(k)] = E[\sum_{k=1}^{L}\sum_{m=0}^{M-1} h(m)c(k)c(k-m)] \\ &= E[\sum_{k=1}^{L} h(0)c^2(k) + \sum_{k=1}^{L}\sum_{m=1}^{M-1} h(m)c(k)c(k-m)] \\ &= h(0)\sum_{k=1}^{L} c^2(k) + E[\sum_{k=1}^{L}\sum_{m=1}^{M-1} h(m)c(k)c(k-m)] \\ &= h(0)L + \sum_{k=1}^{L}\sum_{m=1}^{M-1} h(m)E[c(k)c(k-m)]. \end{aligned} \tag{B.1}$$

Since the PN sequence is a deterministic sequence with the well-known correlation properties,

$$E[c(k)c(k-m)] = \begin{cases} 1 & \text{, if } m = 0 \\ \frac{-1}{L} & \text{, otherwise} \end{cases} \tag{B.2}$$

Then Eq. (B.1) can be expressed as

$$E[\xi_1] = h(0)L - \sum_{m=1}^{M-1} h(m) \tag{B.3}$$

Similarly, the second and third terms can be easily derived as

$$\begin{aligned} E[\xi_2] &= E[\sum_{k=1}^{L} i_0(k)c(k)] = E[\sum_{k=1}^{L}\sum_{m=0}^{M-1} h(m)c(k)j(k-m)] \\ &= \sum_{k=1}^{L} c(k)\sum_{m=0}^{M-1} h(m)E[j(k-m)] = 0 \\ E[\xi_3] &= E[\sum_{k=1}^{L} n_0(k)c(k)] = E[\sum_{k=1}^{L}\sum_{m=0}^{M-1} h(m)c(k)n(k-m)] \end{aligned}$$

$$= \sum_{k=1}^{L} c(k) \sum_{m=0}^{M-1} h(m) E[n(k-m)] = 0.$$

Therefore, the mean value of the decision variable is found as

$$E[\xi] = E[\xi_1] = h(0)L - \sum_{m=1}^{M-1} h(m) \tag{B.4}$$

(ii) The variance of the decision variable ξ for linear prediction-based exciser case:

Since $\{c(k)\}$, $\{j(k)\}$ and $\{n(k)\}$ are assumed to be uncorrelated processes, the variance of the decision variable is expressed as the following The three components of the variance expression in Eq. (5.14) are calculated as

$$var[\xi_1] = \sum_{k=1}^{L} \sum_{l=1}^{L} \sum_{m=1}^{M-1} \sum_{p=1}^{M-1} E[c(k)c(k-m)c(l)c(l-p)]h(m)h(p) \tag{B.5}$$

which can be divided into two parts as

$$var[\xi_1] = \sum_{\substack{k=1 \\ (l=k)}}^{L} \sum_{\substack{m=1 \\ (p=m)}}^{M-1} E[c^2(k)c^2(k-m)]h^2(m) + \sum_{k=1}^{L} \sum_{\substack{l=1 \\ l \neq k}}^{L} \sum_{m=1}^{M-1} \sum_{\substack{p=1 \\ (p \neq m)}}^{M-1} E[c(k)c(k-m)c(l)c(l-p)]h(m)h(p).$$

Since $c^2(k)$ and $c^2(k-m)$ are equal to 1, we can rewrite as

$$var[\xi_1] = \sum_{\substack{k=1 \\ (l=k)}}^{L} \sum_{\substack{m=1 \\ (p=m)}}^{M-1} h^2(m) + \sum_{k=1}^{L} \sum_{\substack{l=1 \\ l \neq k}}^{L} \sum_{m=1}^{M-1} \sum_{\substack{p=1 \\ (p \neq m)}}^{M-1} E[c(k)c(k-m)c(l)c(l-p)]h(m)h(p) \tag{B.6}$$

For long PN sequences it can be shown that $E[c(k)c(k-m)c(l)c(l-p)]$ has a non-zero value only for $k = l$ and $m = p$ conditions [24][28]. Obviously these conditions can not be satisfied in the second term of Eq. (B.6). Therefore, Eq. (B.6) becomes

$$var[\xi_1] = \sum_{k=1}^{L} \sum_{m=1}^{M-1} h^2(m) = L \sum_{m=1}^{M-1} h^2(m) \tag{B.7}$$

Similarly,

$$var[\xi_2] = \sum_{k=1}^{L} \sum_{l=1}^{L} \sum_{m=0}^{M-1} \sum_{p=0}^{M-1} E[c(k)c(l)j(k-m)j(l-p)]h(m)h(p) \tag{B.8}$$

Since $\{c(k)\}$, and $\{j(k)\}$ are assumed to be uncorrelated

$$E[c(k)c(l)j(k-m)j(l-p)] = E[c(k)c(l)]E[j(k-m)j(l-p)]$$

$E[c(k)c(l)]$ was given in Eq. (B.2), and

$$E[j(k-m)j(l-p)] = R_j(k-m-l+p),$$

(where $R_j(0) = \sigma_j^2$). Therefore,

$$\begin{aligned} var[\xi_2] &= \sum_{\substack{k=1 \\ (l=k)}}^{L} E[c^2(k)] \sum_{m=0}^{M-1} \sum_{p=0}^{M-1} h(m)h(p)R_j(p-m) + \\ &\quad \sum_{k=1}^{L} \sum_{\substack{l=1 \\ (l\neq k)}}^{L} \sum_{m=0}^{M-1} \sum_{p=0}^{M-1} E[c(k)c(l)]h(m)h(p)R_j(k-m-l+p) \\ &= L \sum_{m=0}^{M-1} \sum_{p=0}^{M-1} h(m)h(p)R_j(p-m) \\ &\quad -\frac{1}{L} \sum_{k=1}^{L} \sum_{\substack{l=1 \\ (l\neq k)}}^{L} \sum_{m=0}^{M-1} \sum_{p=0}^{M-1} h(m)h(p)R_j(k-m-l+p) \end{aligned} \tag{B.9}$$

Finally, the variance of the last term is derived as

$$var[\xi_3] = \sum_{k=1}^{L} \sum_{l=1}^{L} \sum_{m=0}^{M-1} \sum_{p=0}^{M-1} E[c(k)c(l)n(k-m)n(l-p)]h(m)h(p) \tag{B.10}$$

Since $\{c(k)\}$, and $\{n(k)\}$ are assumed to be uncorrelated

$$E[c(k)c(l)n(k-m)n(l-p)] = E[c(k)c(l)]E[n(k-m)n(l-p)]$$

$$E[n(k-m)n(l-p)] = R_n(k-m-l+p) = \sigma_n^2\delta(k-m-l+p).$$

(where $R_n(0) = \sigma_n^2$). Therefore,

$$\begin{aligned} var[\xi_3] &= \sum_{\substack{k=1 \\ (l=k)}}^{L} E[c^2(k)] \sum_{m=0}^{M-1}\sum_{p=0}^{M-1} h(m)h(p)R_n(p-m) \\ &\quad + \sum_{k=1}^{L}\sum_{\substack{l=1 \\ (l\neq k)}}^{L}\sum_{m=0}^{M-1}\sum_{p=0}^{M-1} E[c(k)c(l)]h(m)h(p)R_n(k-m-l+p) \\ &= L\sigma_n^2\sum_{m=0}^{M-1} h^2(m) - \frac{\sigma_n^2}{L}\sum_{k=1}^{L}\sum_{\substack{l=1 \\ (l\neq k)}}^{L}\sum_{m=0}^{M-1}\sum_{p=0}^{M-1} h(m)h(p)\delta(k-m-l+p). \end{aligned} \tag{B.11}$$

Hence the total variance can be written as

$$\begin{aligned} var[\xi] &= L\sum_{m=1}^{M-1} h^2(m) + L\sum_{m=0}^{M-1}\sum_{p=0}^{M-1} h(m)h(p)\{R_j(p-m) + \sigma_n^2\delta(p-m)\} \\ &\quad -\frac{1}{L}\sum_{k=1}^{L}\sum_{\substack{l=1 \\ (l\neq k)}}^{L}\sum_{m=0}^{M-1}\sum_{p=0}^{M-1} h(m)h(p)\{R_j(k-m-l+p) + \sigma_n^2\delta(k-m-l+p)\}. \end{aligned} \tag{B.12}$$

B.2 Transform Domain-Based Exciser Case

(i) The mean value of the decision variable ξ for transform domain-based exciser case:

Since $\{c(k)\}$, $\{i(k)\}$ and $\{n(k)\}$ in Eq. (5.41) are uncorrelated processes, then

$$E[\xi] = E[\xi_1 + \xi_2 + \xi_3] = E[\xi_1] + E[\xi_2] + E[\xi_3]$$

The first term

$$E[\xi_1] = E[L\sum_{i=1}^{M} t_i(0) + \sum_{k=N}^{N+L-1}\sum_{i=1}^{M}\sum_{l=1}^{2N-2} t_i(l)c(k-l)c(k)]$$

$$= L\sum_{i=1}^{M} t_i(0) + \sum_{k=N}^{N+L-1} \sum_{i=1}^{M} \sum_{l=1}^{2N-2} t_i(l) E[c(k-l)c(k)]$$

By considering Eq. (B.2),

$$E[\xi_1] = L\sum_{i=1}^{M} t_i(0) - \frac{1}{L} \sum_{k=N}^{N+L-1} \sum_{i=1}^{M} \sum_{l=1}^{2N-2} t_i(l) = L\sum_{i=1}^{M} t_i(0) - \sum_{l=1}^{2N-2} t_i(l). \quad \text{(B.13)}$$

Similarly, the second term is calculated as

$$E[\xi_2] = E[\sum_{k=N}^{N+L-1} \sum_{i=1}^{M} \sum_{l=0}^{2N-2} t_i(l)[c(k)j(k-l)] \quad \text{(B.14)}$$
$$= \sum_{k=N}^{N+L-1} \sum_{i=1}^{M} \sum_{l=0}^{2N-2} t_i(l) E[c(k)] E[j(k-l)] = 0$$

The last term is expressed as

$$E[\xi_3] = E[\sum_{k=N}^{N+L-1} \sum_{i=1}^{M} \sum_{l=0}^{2N-2} t_i(l)[c(k)n(k-l)] \quad \text{(B.15)}$$
$$= \sum_{k=N}^{N+L-1} \sum_{i=1}^{M} \sum_{l=0}^{2N-2} t_i(l) E[c(k)] E[n(k-l)] = 0$$

The mean value of the decision variable ξ is therefore found as

$$E[\xi] = E[\xi_1] = L\sum_{i=1}^{M} t_i(0) - \frac{1}{L} \sum_{k=N}^{N+L-1} \sum_{i=1}^{M} \sum_{l=1}^{2N-2} t_i(l). \quad \text{(B.16)}$$

(ii) The variance of the decision variable ξ for transform domain-based exciser case:

The variance of ξ in Eq. (5.42) for the transform domain-based exciser case is calculated as

$$var[\xi] = E[\xi^2] - E^2[\xi]$$

Assuming that all three processes $\{\xi_1, \xi_2, \xi_3\}$ are uncorrelated and using Eq. (5.43), then,

$$var[\xi] = E[(\xi_1 + \xi_2 + \xi_3)^2] - E^2[\xi]$$
$$= E[\xi_1^2] + E[\xi_2^2] + E[\xi_3^2] - E^2[\xi_1].$$

Resulting with,

$$var[\xi] = var[\xi_1] + var[\xi_2] + var[\xi_3]$$

The first term can be written as

$$\begin{aligned}
var[\xi_1] &= var[\sum_{k=N}^{N+L-1}\sum_{i=1}^{M}\sum_{l=0}^{2N-2} t_i(l)c(k)c(k-l)] \\
&= E[\sum_{k=N}^{N+L-1}\sum_{p=N}^{N+L-1}\sum_{i=1}^{M}\sum_{r=1}^{M}\sum_{l=0}^{2N-2}\sum_{s=0}^{2N-2} t_i(l)t_r(s)c(k)c(k-l)c(p)c(p-s)] \\
&\quad -E^2[\sum_{k=N}^{N+L-1}\sum_{i=1}^{M}\sum_{l=0}^{2N-2} t_i(l)c(k)c(k-l)] \\
&= \sum_{k=N}^{N+L-1}\sum_{p=N}^{N+L-1}\sum_{i=1}^{M}\sum_{r=1}^{M} t_i(0)t_r(0)E[c(k)c(k-0)c(p)c(p-0)] \\
&\quad + \sum_{k=N}^{N+L-1}\sum_{p=N}^{N+L-1}\sum_{i=1}^{M}\sum_{r=1}^{M}\sum_{l=1}^{2N-2}\sum_{s=1}^{2N-2} t_i(l)t_r(s)E[c(k)c(k-l)c(p)c(p-s)] \\
&\quad -[L\sum_{i=1}^{M} t_i(0) - \frac{1}{L}\sum_{k=N}^{N+L-1}\sum_{i=1}^{M}\sum_{l=1}^{2N-2} t_i(l)]^2
\end{aligned}$$

However, it is obvious that $E[c(k)c(k-0)c(p)c(p-0)] = E[c^2(k)c^2(p)] = 1$ and then

$$\begin{aligned}
var[\xi_1] &= L^2\sum_{i=1}^{M}\sum_{r=1}^{M} t_i(0)t_r(0) - [L\sum_{i=1}^{M} t_i(0) - \frac{1}{L}\sum_{k=N}^{N+L-1}\sum_{i=1}^{M}\sum_{l=1}^{2N-2} t_i(l)]^2 \\
&\quad + \underbrace{\sum_{k=N}^{N+L-1}\sum_{p=N}^{N+L-1}\sum_{i=1}^{M}\sum_{r=1}^{M}\sum_{l=1}^{2N-2}\sum_{s=1}^{2N-2} t_i(l)t_r(s)E[c(k)c(k-l)c(p)c(p-s)]}_{A}
\end{aligned} \tag{B.17}$$

Eq. (B.17) can be further simplified for the following cases:

(i) For the short-length sequences, considering that PN-code is deterministic to the desired user, the expectation operation in Eq. (B.17) can be dropped [25].

(ii) For the long-length sequences, the PN code has the white noise property [24][28]:

$$E[c(k)c(p)c(k-l)c(p-s)] = \begin{cases} 1 & \text{, if } l=s=0 \\ \delta_{l-s} & \text{, } l>0,\ s>0,\ k=p \\ 0 & \text{, otherwise} \end{cases} . \quad \text{(B.18)}$$

Therefore, the expected value in A of Eq. (B.17) can be rewritten by using the conditions of Eq. (B.18) as

$$E[c(k)c(k-l)c(p)c(p-s)] = \delta(k-p)E[c(k-l)c(p-s)] = \delta(k-p)\delta(s-l).$$

Finally, the variance of ξ_1 is expressed as

$$\begin{aligned} var[\xi_1] &= L^2\sum_{i=1}^{M}\sum_{r=1}^{M} t_i(0)t_r(0) - [L\sum_{i=1}^{M} t_i(0) - \frac{1}{L}\sum_{k=N}^{N+L-1}\sum_{i=1}^{M}\sum_{l=1}^{2N-2} t_i(l)]^2 \\ &\quad + L^2\sum_{i=1}^{M}\sum_{r=1}^{M}\sum_{l=1}^{2N-2} t_i(l)t_r(l) \\ &= L^2\sum_{i=1}^{M}\sum_{r=1}^{M}\sum_{l=0}^{2N-2} t_i(l)t_r(l) - [L\sum_{i=1}^{M} t_i(0) - \frac{1}{L}\sum_{k=N}^{N+L-1}\sum_{i=1}^{M}\sum_{l=1}^{2N-2} t_i(l)]^2. \end{aligned} \quad \text{(B.19)}$$

This term corresponds to distortion of the code due to the transform domain excision operation. Note that if there is no excision, Eq. B.19 becomes zero.

The variance of the second term is given by

$$\begin{aligned} var[\xi_2] &= var[\sum_{k=N}^{N+L-1}\sum_{i=1}^{M}\sum_{l=0}^{2N-2} t_i(l)c(k)j(k-l)] \\ &= E[\sum_{k=N}^{N+L-1}\sum_{p=N}^{N+L-1}\sum_{i=1}^{M}\sum_{r=1}^{M}\sum_{l=0}^{2N-2}\sum_{s=0}^{2N-2} t_i(l)c(k)j(k-l)t_r(s)c(p)j(p-s)] \\ &= \sum_{k=N}^{N+L-1}\sum_{p=N}^{N+L-1}\sum_{i=1}^{M}\sum_{r=1}^{M}\sum_{l=0}^{2N-2}\sum_{s=0}^{2N-2} t_i(l)t_r(s)E[c(k)c(p)j(k-l)j(p-s)]. \end{aligned} \quad \text{(B.20)}$$

Since $\{c(k)\}$ and $\{j(k)\}$ are uncorrelated,

$$E[c(k)c(p)j(k-l)j(p-s)] = E[c(k)c(p)]E[j(k-l)j(p-s)],$$

and

$$E[j(k-l)j(p-s)] = R_j(k-l-p+s).$$

Eq. (B.20) becomes,

$$\begin{aligned} var[\xi_2] &= \sum_{k=N}^{N+L-1} c^2(k) \sum_{i=1}^{M}\sum_{r=1}^{M}\sum_{l=0}^{2N-2}\sum_{s=0}^{2N-2} t_i(l)t_r(s)R_j(s-l) \\ &\quad -\frac{1}{L}\sum_{k=N}^{N+L-1}\sum_{\substack{p=N\\p\neq k}}^{N+L-1}\sum_{i=1}^{M}\sum_{r=1}^{M}\sum_{l=0}^{2N-2}\sum_{s=0}^{2N-2} t_i(l)t_r(s)R_j(k-l-p+s), \\ &= L\sum_{i=1}^{M}\sum_{r=1}^{M}\sum_{l=0}^{2N-2}\sum_{s=0}^{2N-2} t_i(l)t_r(s)R_j(s-l) \\ &\quad -\frac{1}{L}\sum_{k=N}^{N+L-1}\sum_{\substack{p=N\\p\neq k}}^{N+L-1}\sum_{i=1}^{M}\sum_{r=1}^{M}\sum_{l=0}^{2N-2}\sum_{s=0}^{2N-2} t_i(l)t_r(s)R_j(k-l-p+s). \end{aligned} \tag{B.21}$$

Similarly, the third term is derived as

$$\begin{aligned} var[\xi_3] &= var[\sum_{k=N}^{N+L-1}\sum_{i=1}^{M}\sum_{l=0}^{2N-2} t_i(l)c(k)n(k-l)] \\ &= E[\sum_{k=N}^{N+L-1}\sum_{p=N}^{N+L-1}\sum_{i=1}^{M}\sum_{r=1}^{M}\sum_{l=0}^{2N-2}\sum_{s=0}^{2N-2} t_i(l)c(k)n(k-l)t_r(s)c(p)n(p-s)] \\ &= \sum_{k=N}^{N+L-1}\sum_{p=N}^{N+L-1}\sum_{i=1}^{M}\sum_{r=1}^{M}\sum_{l=0}^{2N-2}\sum_{s=0}^{2N-2} t_i(l)t_r(s)E[c(k)c(p)n(k-l)n(p-s)]. \end{aligned} \tag{B.22}$$

Since $\{c(k)\}$ and $\{n(k)\}$ are uncorrelated,

$$E[c(k)c(p)n(k-l)n(p-s)] = E[c(k)c(p)]E[n(k-l)n(p-s)]$$

and

$$E[n(k-l)n(p-s)] = R_n(k-l-p+s) = \sigma_n^2\delta_{(k-l-p+s)}.$$

then

$$
\begin{aligned}
var[\xi_3] &= \sum_{k=N}^{N+L-1} c^2(k) \sum_{i=1}^{M}\sum_{r=1}^{M}\sum_{l=0}^{2N-2}\sum_{s=0}^{2N-2} t_i(l)t_r(s)R_n(s-l) \\
&\quad -\frac{1}{L}\sum_{k=N}^{N+L-1}\sum_{\substack{p=N \\ p\neq k}}^{N+L-1}\sum_{i=1}^{M}\sum_{r=1}^{M}\sum_{l=0}^{2N-2}\sum_{s=0}^{2N-2} t_i(l)t_r(s)R_n(k-l-p+s), \\
&= L\sum_{i=1}^{M}\sum_{r=1}^{M}\sum_{l=0}^{2N-2}\sum_{s=0}^{2N-2} t_i(l)t_r(s)\sigma_n^2\delta(s-l) \\
&\quad -\frac{1}{L}\sum_{k=N}^{N+L-1}\sum_{\substack{p=N \\ p\neq k}}^{N+L-1}\sum_{i=1}^{M}\sum_{r=1}^{M}\sum_{l=0}^{2N-2}\sum_{s=0}^{2N-2} t_i(l)t_r(s)\sigma_n^2\delta(k-l-p+s) \\
&= L\sigma_n^2\sum_{i=1}^{M}\sum_{r=1}^{M}\sum_{l=0}^{2N-2} t_i(l)t_r(l) \\
&\quad -\frac{1}{L}\sum_{k=N}^{N+L-1}\sum_{\substack{p=N \\ p\neq k}}^{N+L-1}\sum_{i=1}^{M}\sum_{r=1}^{M}\sum_{l=0}^{2N-2}\sum_{s=0}^{2N-2} t_i(l)t_r(s)\sigma_n^2\delta(k-l-p+s).
\end{aligned}
\tag{B.23}
$$

Therefore, the total variance is expressed as the sum of the three terms as

$$
\begin{aligned}
var[\xi] &= L^2\sum_{i=1}^{M}\sum_{r=1}^{M}\sum_{l=0}^{2N-2} t_i(l)t_r(l) - [L\sum_{i=1}^{M} t_i(0) - \frac{1}{L}\sum_{k=N}^{N+L-1}\sum_{i=1}^{M}\sum_{l=1}^{2N-2} t_i(l)]^2 \\
&\quad +L\sum_{i=1}^{M}\sum_{r=1}^{M}\sum_{l=0}^{2N-2}\sum_{s=0}^{2N-2} t_i(l)t_r(s)R_j(s-l) \\
&\quad -\frac{1}{L}\sum_{k=N}^{N+L-1}\sum_{\substack{p=N \\ p\neq k}}^{N+L-1}\sum_{i=1}^{M}\sum_{r=1}^{M}\sum_{l=0}^{2N-2}\sum_{s=0}^{2N-2} t_i(l)t_r(s)R_j(k-l-p+s) \\
&\quad +L\sigma_n^2\sum_{i=1}^{M}\sum_{r=1}^{M}\sum_{l=0}^{2N-2} t_i(l)t_r(l) \\
&\quad -\frac{1}{L}\sum_{k=N}^{N+L-1}\sum_{\substack{p=N \\ p\neq k}}^{N+L-1}\sum_{i=1}^{M}\sum_{r=1}^{M}\sum_{l=0}^{2N-2}\sum_{s=0}^{2N-2} t_i(l)t_r(s)\sigma_n^2\delta(k-l-p+s).
\end{aligned}
\tag{B.24}
$$

REFERENCES

1. A. N. Akansu and M. J. T. Smith, Eds., *Subband and Wavelet Transforms: Design and Applications*, Kluwer, New York, New York, 1995.

2. A. N. Akansu, "Wavelet Transforms and Relations to Filter Banks," in *IEEE ISCAS: A Tutorial*, pp. 167–177, May 1995.

3. A. N. Akansu and H. Caglar, "A Measure of Aliasing Energy in Multiresolution Signal Decomposition," in *IEEE International Conference on Acoustics, Speech, and Signal Processing*, vol. IV, pp. 621–624, 1992.

4. A. N. Akansu and R. A. Haddad, *Multiresolution Signal Decomposition, Transforms, Subbands, Wavelets*, Academic Press, San Diego, California, 1992.

5. A. N. Akansu and Y. Liu, "On Signal Decomposition Techniques," *Optical Engineering*, vol. 30, pp. 912–920, July 1991.

6. S. Akselrod, D. Gordon, F. A. Ubel, D. C. Shannon, A. C. Barger, and R. S. Cohen, "Power Spectrum Analysis of Heart Rate Fluctuation: A Quantative Probe of Beat-To-Beat Cardiovascular Control," *Science*, vol. 213, pp. 220–222, July 1981.

7. R. M. Berne and M. V. Levy, *Cardiovascular Physiology*, MO: Mosby, St. Louis, fifth ed., 1986.

8. H. Caglar, Y. Liu, and A. N. Akansu, "Statistically Optimized PR-QMF Design," in *SPIE Visual Communication and Image Processing*, pp. 86–94, November 1991.

9. R. R. Coifman and M. V. Wickerhauser, "Best-adapted Wave Packet Bases," *preprint, Yale University.*

10. A. Croisier, D. Esteban, and C. Galand, "Perfect Channel Splitting by Use of Interpolation/Decimation Tree Decomposition," in *International Conference. on Information Sciences and Systems*, Patras, 1976.

11. I. Daubechies, "Orthonormal Bases of Compactly Supported Wavelets," *Comm. in Pure and Applied Math.*, vol. 41, pp. 909–996, 1988.

12. S. Davidovici and E. G. Kanterakis, "Narrow-band Interference Rejection Using Real-time Fourier Transforms," *IEEE Trans. Com.*, vol. COM-37, pp. 713–722, July 1989.

13. R. W. DeBoer, J. M. Karemaker, and J. Strackee, "Comparing Spectra of a Series of Point Events Particularly for Heart Rate Variability Data," *IEEE Trans. Biomedical Eng.*, vol. BME-31, pp. 384–387, 1984.

14. R. DiPietro, "An FFT-based Technique for Suppressing Narrow-band Interference in PN Spread Spectrum Communications Systems," in *IEEE ICASSP*, pp. 1360–1363, 1989.

15. R. C. Dixon, *Spread Spectrum Systems*, John Wiley & Sons, New York, second ed., 1984.

16. J. L. Elghozi, D. Laude, and A. Girard, "Effects of Respiration on Blood Pressure and Heart Rate Variability in Humans," *Clinical and Experimental Pharmacology and Physiology*, vol. 18, pp. 735–742, 1991.

17. N. J. Fliege, *Multirate Digital Signal Processing*, John Wiley & Sons, UK, 1994.

18. J. Gevargiz, M. Rosenmann, P. Das, and L. B. Milstein, "A Comparison of Weighted and Non-Weighted Transform Domain Processing Systems for Narrowband Interference Excision," in *IEEE MILCOM*, pp. 32.2.1–32.3.4, 1984.

19. R. A. Haddad, "A Class of Orthogonal Nonrecursive Binomial Filters," *IEEE Transactions on Audio and Electroacoustics*, pp. 296–304, December 1971.

20. R. A. Haddad, A. N. Akansu, and A. Benyassine, "Time-Frequency Localizations in Transforms, Subbands and Wavelets: A Critical Review," *Optical Engineering*, vol. 32, no. 7, pp. 1411–1429, July 1993.

21. S. Haykin, *Communication Systems*, John Wiley & Sons, New York, New York, second ed., 1983.

22. C. Herley and M. Vetterli, "Orthogonal Time-varying filter Banks and Wavelet Packets," *IEEE Trans. on Signal Processing*, pp. 2650–2663, November 1994.

23. F. Hlawatsch and G. F. Boudreaux-Bartels, "Linear and Quadratic Time-Frequency Signal Representations," *IEEE Signal Processing Magazine*, vol. 9, no. 2, pp. 21–67, 1992.

24. F. M. Hsu and A. A. Giordano, "Digital Whitening Techniques for Improving Spread Spectrum Communications Performance in the Presence of Narrow-band Jamming and Interference," *IEEE Trans. Communications*, vol. COM-26, pp. 209–216, 1978.

25. R. Iltis and L. Milstein, "Performance Analysis of Narrow-Band Interference Rejection Techniques in DS Spread-Spectrum Systems," *IEEE Trans. Communications*, vol. COM-32, pp. 1169–1177, November 1984.

26. N. S. Jayant and P. Noll, *Digital Coding of Waveforms*, Prentice-Hall, Englewood Cliffs, 1984.

27. W. W. Jones and K. R. Jones, "Narrowband Interference Suppression Using Filter Bank Analysis/Synthesis Techniques," in *IEEE MILCOM*, pp. 38.1.1–38.1.5, 1992.

28. J. W. Ketchum and J. G. Proakis, "Adaptive Algorithms for Estimating and Suppressing Narrow-Band Interference in PN Spread-Spectrum Systems," *IEEE Trans. Communications*, vol. COM-30, pp. 913–924, May 1982.

29. E. Masry and L. B. Milstein, "Performance of DS Spread-Spectrum Receiver Employing Interference-Suppression Filters Under a Worst-Case Jamming Condition," *IEEE Trans. Com.*, vol. COM-34, pp. 13–21, January 1986.

30. M. Medley, G. J. Saulnier, and P. Das, "Applications of the Wavelet Transform in Spread Spectrum Communications Systems," in 3^{rd} *NJIT Symposium on Applications of Subbands and Wavelets*, March 1994.

31. M. Meyer, M. V. Tazebay, and A. N. Akansu, "A Sliding and Variable Window-Based Multitone Excision for Digital Audio Broadcasting," in *IEEE ISCAS*, vol. 2, pp. 1464–1467, April 1995.

32. L. B. Milstein, "Interference Rejection Techniques in Spread Spectrum Communications," *Proc. IEEE*, vol. 76, no. 6, pp. 657–671, June 1988.

33. L. B. Milstein and P. Das, "An Analysis of a Real-Time Transform Domain Filtering Digital Communication System: Part I: Narrow-Band Interference Rejection," *IEEE Trans. Communications*, vol. COM-28, pp. 816–824, June 1980.

34. K. Nayebi, T. P. Barnwell, and M. J. T. Smith, "Analysis-Synthesis Systems with Time-Varying Filter Bank Structures," in *IEEE International Conference on Acoustics, Speech, and Signal Processing*, vol. IV, San Fransisco, CA, pp. 617–620, 1992.

35. T. Q. Nguyen and P. P. Vaidyanathan, "Two-channel perfect reconstruction FIR QMF structures which yield linear phase analysis and synthesis filters," *IEEE Transactions on Signal Processing*, vol. 37, pp. 676–690, May 1989.

36. D. L. Nicholson, *Spread Spectrum Signal Design and AJ Systems*, Computer Science Press, Maryland, 1988.

37. A. V. Oppenheim and R. W. Schafer, *Discrete-Time Signal Processing*, Prentice-Hall, Inc., Englewood Cliffs, New Jersey, 1989.

38. M. Pagani and et. al., "Power Spectral Analysis of Heart Rate and Arterial Pressure Variabilities as a Marker of Sympatho-Vagal Interaction in Man and Conscious Dog," *Circulation Research*, vol. 59, no. 2, pp. 178 193, 1986.

39. R. Rifkin, "Comments on 'Narrow-band Interference Rejection Using Real-time Fourier Transforms'," *IEEE Trans. Com.*, vol. COM-39, September 1991.

40. D. V. Sarwate and M. B. Pursley, "Crosscorrelation Properties of Pseudorandom and Related Sequences," *Proceedings of the IEEE*, May 1980.

41. B. M. A. Sayers, "Analysis of Heat Rate Variability," *Ergonomics*, vol. 16, no. 1, pp. 17–32, 1973.

42. S. J. Shin, W. N. Tapp, S. Reisman, and B. H. Natelson, "Assessment of Autonomic Regulation of Heart Rate Variability by the Method of Complex Demodulation," *IEEE Transactions on Biomedical Engineering*, vol. 36, no. 2, pp. 274–282, February 1989.

43. M. J. T. Smith and T. P. Barnwell, "A Procedure for Designing Exact Reconstruction Filter Banks for Tree-Structured Sub-band Coders," in *IEEE International Conference on Acoustics, Speech, and Signal Processing*, pp. 27.1.1–27.1.4, March 1984.

44. M. J. T. Smith and T. P. Barnwell, "Exact Reconstruction Techniques for Tree-Structured Subband Coders," *IEEE Trans. on ASSP*, pp. 434–441, August 1986.

45. M. V. Tazebay and A. N. Akansu, "Progressive optimality in hierarchical trees," in *IEEE International Conference on Image Processing*, Austin,TX, pp. 825–829, November 1994.

46. M. V. Tazebay and A. N. Akansu, "Progressive Optimization of Time-Frequency Localization in Subband Trees," in *IEEE International Symposium on Time-Frequency and Time-Scale Analysis*, pp. 128–131, The IEEE Signal Processing Society and The IEEE Philadelphia Section, October 1994.

47. M. V. Tazebay and A. N. Akansu, "A Comparative Performance Study of Excisers in Spread Spectrum Communications," in *IEEE Global Telecommunications Conference*, Singapore, November 1995.

48. M. V. Tazebay and A. N. Akansu, "A Smart Time-Frequency Exciser Technique for DSSS Communications," in *IEEE International Conference on Acoustics , Speech, and Signal Processing*, vol. 2, pp. 1209–1212, May 1995.

49. M. V. Tazebay and A. N. Akansu, "Adaptive Subband Transforms in Time-Frequency Excisers for DSSS Communications Systems," *IEEE Transactions on Signal Processing*, vol. 43, pp. 1776–1782, November 1995.

50. M. V. Tazebay, A. N. Akansu, and M. J. Sherman, "A Novel Adaptive Time-Frequency Excision Technique for Direct Sequence Spread Spectrum Communications," in *IEEE International Symposium on Time-Frequency*

and Time-Scale Analysis, pp. 492–495, The IEEE Signal Processing Society and The IEEE Philadelphia Section, October 1994.

51. M. V. Tazebay, R. Saliba, and S. Reisman, "Adaptive Time-Frequency Analysis of Autonomic Nervous System," in *IEEE International Conference for Engineering in Medicine and Biology Society*, Montreal, Canada, September 1995.

52. P. P. Vaidyanathan, "Quadrature Mirror Filter Bank, M-band Extensions and Perfect Reconstruction Techniques," *IEEE ASSP Magazine*, pp. 4–20, July 1987.

53. P. P. Vaidyanathan, "Theory and Design of M-Channel Maximally Decimated Quadrature Mirror Filters with Arbitrary M, Having the Perfect Reconstruction Property," *IEEE Trans. on ASSP*, pp. 476–492, April 1987.

54. P. P. Vaidyanathan, "Multirate Digital Filters, Filter Banks, Polyphase Networks and Applications: A Tutorial," *Proc. of IEEE*, vol. 78, pp. 56–93, 1990.

55. P. P. Vaidyanathan, *Multirate Systems and Filter Banks*, Prentice-Hall, Inc., Englewood Cliffs, New Jersey, 1993.

56. M. Vetterli, "A Theory of Multirate Filter Banks," *IEEE Trans. ASSP*, vol. 35, pp. 356–372, 1987.

57. E. Viscito and J. Allebach, "The Design of Tree-structured M-channel Filter Banks using Perfect Reconstruction Filter Blocks," in *IEEE International Conference on Acoustics, Speech, and Signal Processing*, pp. 1475–1478, 1988.

58. R. E. Ziemer and R. L. Peterson, *Digital Communications and Spread Spectrum Systems*, Macmillan Publishing Company, New York, New York, 1985.